

UNIVERSITY OF CALIFORNIA
SANTA CRUZ

**SEARCH FOR WW AND WZ RESONANCES IN $\ell\nu qq$ FINAL
STATES IN pp COLLISIONS AT $\sqrt{s} = 13$ TEV WITH THE ATLAS
DETECTOR**

A dissertation submitted in partial satisfaction of the
requirements for the degree of

DOCTOR OF PHILOSOPHY

in

PHYSICS

by

Natasha Woods

December 2019

The Dissertation of Natasha Woods
is approved:

Abraham Seiden, Chair

Mike Hance

Bruce Schumm

Quentin Williams
Vice Provost and Dean of Graduate Studies

Copyright © by

Natasha Woods

2019

Table of Contents

List of Figures	vi
List of Tables	xvi
Abstract	xviii
Dedication	xix
Acknowledgments	xx
I Introduction	1
1 Introduction	2
II Theoretical Motivation	6
2 The Standard Model of Particle Physics	7
2.1 Introduction	7
2.2 Quantum Field Theory	7
2.3 $U(1)_{EM}$ Local Gauge Invariance	8
2.4 Yang-Mills Gauge Theories	11
2.5 Particles in the Standard Model	12
2.6 Higgs Mechanism	17
2.7 Electroweak Theory	18
2.8 Quantum ChromoDynamics	19
3 Standard Model Successes and Limitations	25
4 New Physics Models with Diboson Resonances	28
4.1 Randall Sundrum Bulk Model	28
4.2 Simple Standard Model Extensions	30

III Experimental Setup	32
5 LHC	33
5.1 LHC Layout and Design	35
6 The ATLAS Detector	40
6.1 Coordinate System	42
6.2 Inner Detector	43
6.2.1 Pixel Detector	46
6.2.2 Semiconductor Tracker	46
6.2.3 Transition Radiation Tracker	46
6.3 Calorimeters	48
6.4 Muon Spectrometer	52
6.5 Magnet System	56
6.6 Trigger System	57
IV Method	59
7 Dataset and Simulated Samples	60
7.1 Dataset	60
7.2 Simulated Samples	63
8 Objects	64
8.1 Electrons	64
8.2 Muons	65
8.3 Jets	66
8.3.1 Small-R jets	69
8.3.2 Large-R jets	69
8.3.3 Variable Radius jets	72
8.3.4 Jet Flavor Tagging	73
8.4 MET/Neutrinos	73
8.5 Overlap Removal	73
8.6 Reconstructed Resonance Mass (m_{WV})	74
9 Event Selection and Categorization	76
9.1 Pre-selection	76
9.2 Trigger	76
9.3 non-VBF/VBF RNN	78
9.4 Signal Region Definitions	85
9.5 Selection Acceptance and Efficiency	87
9.6 Background Estimate	89
9.6.1 Control Regions	89

9.6.2	Fake Lepton Backgrounds	97
10	Systematic Uncertainties	111
10.1	Experimental Systematics	111
10.2	Theory Systematics	113
11	Statistical Analysis	121
11.1	Likelihood Function Definition	121
11.2	Fit Configuration	122
11.3	Best Fit μ	124
11.4	Discovery Test	125
11.5	Exclusion Limits	126
12	Results	128
12.1	Expected and Measured Yields	128
12.2	Systematic Profiling and Correlations	142
12.3	Discovery Tests	144
12.4	Limits	150
V	Quark and Gluon Tagging	152
13	Prospects	153
14	n_{trk} Calibration	160
15	Application	166
VI	Conclusion	171
16	Conclusions	172
	Bibliography	173

List of Figures

2.1	The particles of the Standard Model.	14
2.2	Summary of how Standard Model particles interact with other Standard Model particles.	15
2.3	This figure shows the three dominant QCD interactions. From Ref. [18]	21
2.4	Strength of the U(1), SU(2), and SU(3) gauge couplings as a function of the energy scale of the interaction (Q). From Ref. [12] . .	22
2.5	A cartoon of string breaking: the QCD string spanned between quark Q and antiquark \bar{Q} breaks due to $q\bar{q}$ creation [4]	24
3.1	A comparison of cross section measurements at $\sqrt{s} = 7, 8, 13$ TeV from ATLAS compared to theoretical measurements. From Ref. [6]	27
4.1	Cartoon of RS Bulk Model	29
5.1	Scaling of cross sections with \sqrt{s} . Natasha: write more here . . .	34
5.2	LHC Layout. Natasha write more	36
5.3	LHC Accelerator. Natasha write more	38
6.1	Big picture layout of ATLAS detector. Natasha: write more . . .	41
6.2	Big picture layout of ATLAS detector. Natasha: write more . . .	41
6.3	A simplified schematic of how different particles interact and are detected within ATLAS.	42
6.4	Layout of ATLAS Inner Detector	44

6.5	Layout of ATLAS ID Barrel System.	45
6.6	Overview of ATLAS electromagnetic and hadronic calorimeters.	49
6.7	Schematic of ECAL.	50
6.8	Schematic of HCAL.	51
6.9	Schematic of Muon Spectrometer [cite G35]	54
6.10	Schematic of MDT chamber. [cite G35]	55
6.11	Schematic of RPC chamber, which is used for triggering in the central region of the detector [cite G35].	55
6.12	Schematic of TGC chamber, which is used for triggering in the muon end-cap region. [cite G35]	56
6.13	Layout of ATLAS magnet systems.	57
7.1	Integrated luminosity for data collected from ATLAS from 2011 - 2018	61
7.2	Mean number of interactions per crossing for data collected from ATLAS from 2011 - 2018	62
8.1	This figure shows the breakdown of the muon reconstruction efficiency scale factor measured in $Z \rightarrow \mu\mu$ as a function of p_T [5].	66
8.2	[8] This diagram shows the calibration stages for EM jets.	68
8.3	The upper cut on D_2 (a) and jet mass window cut i.e. the upper and lower boundary of the mass (b) of the W -tagger as a function of jet p_T . Corresponding values for Z -tagger are shown in (c) and (d). The optimal cut values for maximum significance are shown as solid markers and the fitted function as solid lines. Working points from $VV \rightarrow JJ$ [ATLAS-HDBS-2018-31-002] is also shown as dashed lines as a reference. Natasha reword?	71
8.4	Natasha write caption	72
9.1	RNN architecture. Natasha add caption	80

9.2	This figure shows the embedded logic in LSTM cells. This image was taken from [23], where a more in depth discussion about LSTMs may be found.	81
9.3	RNN Score distribution for ggF and VBF signals and backgrounds.	82
9.4	ROC curve using k-fold validation for RNN.	83
9.5	Comparison of GGF Z' limits for different RNN score selections. The bottom panel shows the ratio of the upper limits set for different RNN cuts to the cut-based analysis. In this panel smaller numbers, indicate that the expected upper limit is smaller than the cut-based analysis, which is desired.	84
9.6	Event Categorization. Natasha write more.	87
9.7	Selection acceptance times efficiency for the $W' \rightarrow WZ \rightarrow \ell\nu qq$ events from MC simulations as a function of the W' mass for (a) Drell-Yan and (b) VBF production, combining the merged HP and LP signal regions of the $WW \rightarrow \ell\nu J$ selection and the resolved regions of the $WW \rightarrow \ell\nu jj$ selection.	88
9.8	Selection acceptance times efficiency for the $G \rightarrow WW \rightarrow \ell\nu qq$ events from MC simulations as a function of the G mass for (a) Drell-Yan and (b) VBF production, combining the merged HP and LP signal regions of the $WW \rightarrow \ell\nu J$ selection and the resolved regions of the $WW \rightarrow \ell\nu jj$ selection.	88
9.9	Data MC comparison for the merged WW HP TCR. The bottom panel shows the ratio of the difference between data and simulation to simulation. The red bands include the all systematic and statistical uncertainties on the background.	91
9.10	Data MC comparison for the merged WW LP TCR. The bottom panel shows the ratio of the difference between data and simulation to simulation. The red bands include the all systematic and statistical uncertainties on the background.	92

9.11 Data MC comparison for the merged WZ HP TCR. The bottom panel shows the ratio of the difference between data and simulation to simulation. The red bands include the all systematic and statistical uncertainties on the background.	93
9.12 Data MC comparison for the merged WZ LP TCR. The bottom panel shows the ratio of the difference between data and simulation to simulation. The red bands include the all systematic and statistical uncertainties on the background.	94
9.13 Data MC comparison for the resolved WW TCR. The bottom panel shows the ratio of the difference between data and simulation to simulation. The red bands include the all systematic and statistical uncertainties on the background.	95
9.14 Data MC comparison for the resolved WZ TCR. The bottom panel shows the ratio of the difference between data and simulation to simulation. The red bands include the all systematic and statistical uncertainties on the background.	96
9.15 The E_T^{miss} distribution in MJCR for 2017 data in the electron channel(left), muon channel with W-boson pT < 150 GeV (center) and > 150 GeV (right). Multi-jet templates are calculated as remaining data components after excluding known MC	99
9.16 Postfit Data/MC comparison of distributions of E_T^{miss} , m_T^W , lepton and neutrino p_T , $m_{\ell\nu jj}$, lepton- ν angular distance in the WW electron channel. The MJ template is obtained from the pre-MJ-fit.	100
9.17 Postfit Data/MC comparison of distributions of E_T^{miss} , m_T^W , lepton and neutrino p_T , $m_{\ell\nu jj}$, lepton- ν angular distance in the WW muon channel. The MJ template is obtained from the pre-MJ-fit.	101
9.18 Postfit Data/MC comparison of distributions of E_T^{miss} , m_T^W , lepton and neutrino p_T , $m_{\ell\nu jj}$, lepton- ν angular distance in the WZ untag electron channel. The MJ template is obtained from the pre-MJ-fit.	102

9.19 Postfit Data/MC comparison of distributions of E_T^{miss} , m_T^W , lepton and neutrino p_T , $m_{\ell\nu jj}$, lepton- ν angular distance in the WZ untag muon channel. The MJ template is obtained from the pre-MJ-fit.	103
9.20 Postfit Data/MC comparison of distributions of E_T^{miss} , m_T^W , lepton and neutrino p_T , $m_{\ell\nu jj}$, lepton- ν angular distance in the WZ untag electron channel. The MJ template is obtained from the pre-MJ-fit.	104
9.21 Postfit Data/MC comparison of distributions of E_T^{miss} , m_T^W , lepton and neutrino p_T , $m_{\ell\nu jj}$, lepton- ν angular distance in the WZ untag muon channel. The MJ template is obtained from the pre-MJ-fit.	105
9.22 Postfit Data/MC comparison of distributions of E_T^{miss} , m_T^W , lepton and neutrino p_T , $m_{\ell\nu jj}$, lepton- ν angular distance in the VBF WW electron channel. The MJ template is obtained from the pre-MJ-fit.	106
9.23 Postfit Data/MC comparison of distributions of E_T^{miss} , m_T^W , lepton and neutrino p_T , $m_{\ell\nu jj}$, lepton- ν angular distance in the VBF WW muon channel. The MJ template is obtained from the pre-MJ-fit.	107
9.24 Postfit Data/MC comparison of distributions of E_T^{miss} , m_T^W , lepton and neutrino p_T , $m_{\ell\nu jj}$, lepton- ν angular distance in the VBF WZ electron channel. The MJ template is obtained from the pre-MJ-fit.	108
9.25 Postfit Data/MC comparison of distributions of E_T^{miss} , m_T^W , lepton and neutrino p_T , $m_{\ell\nu jj}$, lepton- ν angular distance in the VBF WZ muon channel. The MJ template is obtained from the pre-MJ-fit.	109
10.1 The $W/Z+jet$ systematics for the a) Merged ggF, b) Resolved ggF, c) Merged VBF, and d) Resolved VBF regions. The top subplot shows the nominal and variation distributions/bands, the middle shows the ratio of the two, and the final shows just the shape of the envelope (the final uncertainty).	115

10.2 The two-point generator comparison between Sherpa and MadGraph for the W/Z+jet samples in the a) Merged ggF, b) Resolved ggF, c) Merged VBF, and d) Resolved VBF regions. The normalization of the Madgraph sample is set to the Sherpa value to consider only shape effects. The bottom inset shows the ratio of the two.	116
10.3 Ratio between the variations of generator (red) and hadronization (blue) variations for the Merged regime for $t\bar{t}$ sample.	117
10.4 Ratio between the variations of generator (red) and hadronization (blue) variations for the Resolved regime for $t\bar{t}$ sample.	117
10.5 Ratio between the variations of ISR up (red) and down (blue) variations for the Merged regime for $t\bar{t}$ sample.	118
10.6 Ratio between the variations of ISR up (red) and down (blue) variations for the Resolved regime for $t\bar{t}$ sample.	119
10.7 Ratio between the variations of FSR up (red) and down (blue) variations for the Merged regime for $t\bar{t}$ sample.	120
10.8 Ratio between the variations of FSR up (red) and down (blue) variations for the Resolved regime for $t\bar{t}$ sample.	120
11.1 The HVT signal mass resolution as a function of mass fit with a straight line in the Resolved ggF region (left) and VBF (right) region.	124
11.2 The HVT signal mass resolution as a function of mass fit with a straight line in the Merged ggF region (left) and VBF (right) region.	124
12.1 This figure shows the distribution of $m_{\ell\nu qq}$ in the DY WW control regions.	136
12.2 This figure shows the distribution of $m_{\ell\nu qq}$ in the DY WZ control regions.	137
12.3 This figure shows the distribution of $m_{\ell\nu qq}$ in the VBF WW control regions.	138

12.4 This figure shows the distribution of $m_{\ell\nu qq}$ in the VBF WZ control regions.	139
12.5 This figure shows the distribution of $m_{\ell\nu qq}$ in the GGF WW signal regions.	140
12.6 This figure shows the distribution of $m_{\ell\nu qq}$ in the GGF WZ Untag signal regions.	140
12.7 This figure shows the distribution of $m_{\ell\nu qq}$ in the GGF WZ Tag signal regions.	141
12.8 This figure shows the distribution of $m_{\ell\nu qq}$ in the VBF WZ Tag signal regions.	141
12.9 This figure shows the distribution of $m_{\ell\nu qq}$ in the VBF WZ Tag signal regions.	142
12.10 Ranked systematics and their fitted values for WW DY (right) and VBF (left) selections.	143
12.11 Ranked systematics and their fitted values for WZ DY (right) and VBF (left) selections.	143
12.12 Correlations between systematics for WW DY (right) and VBF (left) selections.	144
12.13 These plots show the measured p_0 value as a function of resonance mass for HVT Z' DY production.	145
12.14 These plots show the measured p_0 value as a function of resonance mass for HVT Z' VBF production.	146
12.15 These plots show the measured p_0 value as a function of resonance mass for HVT W' DY production.	147
12.16 These plots show the measured p_0 value as a function of resonance mass for HVT W' VBF production.	148
12.17 These plots show the measured p_0 value as a function of resonance mass for the RS Graviton DY production.	149
12.18 This figure shows theory, expected and observed limits for HVT W' DY (left) and VBF (right) production.	150

12.19 This figure shows theory, expected and observed limits for HVT Z' DY (left) and VBF (right) production.	150
12.20 This figure shows theory, expected and observed limits for RS Gravitons via DY production.	151
13.1 PDGID of the truth-level parton matched to the small-R jets passing the Resolved GGF WW Signal Region selections for the (a) Leading (b) Sub-Leading jets . These distributions are shown for 300, 500, and 700GeV Z' signals and the background.	155
13.2 The number of tracks in small-R jets in events passing the Resolved GGF WW Signal Region selections for the (a) Leading (b) Sub-Leading jets. These distributions are shown for 300, 500, and 700GeV Z' signals and the background.	155
13.3 The number of tracks in background small-R jets in events passing the Resolved GGF WW Signal region selection vs. $\ln(p_T)$ for (a)Leading (b) Sub-Leading jets. The best fit line for the distribution is also shown, as well as the percentage of jets that pass a cut of number of tracks $< 4 \times \ln(p_T) - 5$. Note the number of total entries in these plots has been normalized to one.	156
13.4 The number of tracks in small-R jets in 300GeV Z' events passing the Resolved GGF WW Signal region selection vs. $\ln(p_T)$ for (a)Leading (b) Sub-Leading jets. The best fit line for the distribution is also shown, as well as the percentage of jets that pass a cut of number of tracks $< 4 \times \ln(p_T) - 5$.Note the number of total entries in these plots has been normalized to one.	156
13.5 The number of tracks in small-R jets in 500GeV Z' events passing the Resolved GGF WW Signal region selection vs. $\ln(p_T)$ for (a)Leading (b) Sub-Leading jets. The best fit line for the distribution is also shown, as well as the percentage of jets that pass a cut of number of tracks $< 4 \times \ln(p_T) - 5$.Note the number of total entries in these plots has been normalized to one.	157

13.6 The number of tracks in small-R jets in 700GeV Z' events passing the Resolved GGF WW Signal region selection vs. $\ln(p_T)$ for (a)Leading (b) Sub-Leading jets. The best fit line for the distribution is also shown, as well as the percentage of jets that pass a cut of number of tracks $< 4 \times \ln(p_T) - 5$.Note the number of total entries in these plots has been normalized to one.	157
13.7 The number of tracks in leading small-R jets in background events passing the Resolved GGF WW Signal region selection vs. $\ln(p_T)$ for (a)Gluons (b) Quarks jets. The best fit line for the distribution is also shown, as well as the percentage of jets that pass a cut of number of tracks $< 4 \times \ln(p_T) - 5$.Note the number of total entries in these plots has been normalized to one.	158
13.8 ROC Curve for Quark and Gluon Tagging with a cut on the number of tracks that depends on the $\ln(p_T)$	158
13.9 The top panel shows the distribution of m_{lvqq} with and without quark gluon tagging. The middle panel shows the ratio of the signals and backgrounds with and without quark gluon tagging. The bottom panel shows the change in S/\sqrt{B} with quark gluon tagging.	159
15.1 The top panel shows the distribution of m_{lvqq} with and without requiring jets to be true quarks. The middle panel shows the ratio of the signals and backgrounds with and without requiring jets to be true quarks. The bottom panel shows the change in S/\sqrt{B} when requiring jets to be true quarks.	167
15.2 Unfolded and extracted n_C qg dstbs.	168
15.3 PDGID of the truth-level parton matched to the small-R jets passing the Resolved GGF WW Signal Region selections for the (a) Leading (b) Sub-Leading jets . These distributions are shown for 300, 500, and 700GeV Z' signals and the background.	169

List of Tables

2.1	Representations of the SM fermions under $SU(3)_C \times SU(2)_L \times U(1)_Y$ gauge symmetry group. Rows are correspond to different weak isospin states and columns to different QCD color states.	13
9.1	The list of triggers used in the analysis.	77
9.2	Summary of selection criteria used to define the signal region (SR), W +jets control region (W CR) and $t\bar{t}$ control region ($t\bar{t}$ CR) for merged 1-lepton channel.	86
9.3	The list of selection cuts in the resolved analysis for the WW and WZ signal regions (SR), W +jets control region (WR) and $t\bar{t}$ control region (TR).	87
9.4	Definitions of “inverted” leptons used in multijet control region . .	98
9.5	Fit validation result in WCRs for 2015+16 data. The fit is done in various WCRs, in order to obtain the corresponding scale factors for MJ templates: ggF resolved WCR for the $WW \rightarrow lvqq$ selection, ggF resolved untagged WCR for the $WZ \rightarrow lvqq$ selection, ggF resolved tagged WCR for the $WZ \rightarrow lvqq$ selection, VBF resolved WCR for the $WW \rightarrow lvqq$ selection, and VBF resolved WCR for the $WZ \rightarrow lvqq$ selection. Post-fit event yields for electroweak processes and MJ contributions are shown. The SF column shows the corresponding normalization scale factors for electroweak processes from the fit. R.U. stands for relative uncertainty.	110

12.1	Expected and Measured for DY WW $W+\text{jets}$, $t\bar{t}$ control regions and signal regions.	129
12.2	Expected and Measured for DY WZ $W+\text{jets}$, $t\bar{t}$ tag and untag control regions.	130
12.3	Expected and Measured for DY WZ $W+\text{jets}$, $t\bar{t}$ tag and untag signal regions.	131
12.4	Expected and Measured for VBF WW $W+\text{jets}$, $t\bar{t}$ control regions and signal regions.	132
12.5	Expected and Measured for VBF WZ $W+\text{jets}$, $t\bar{t}$ control regions and signal regions.	133
12.6	Fitted background normalizations for $t\bar{t}$ and $W+\text{jets}$ backgrounds for the DY WW analysis region.	134
12.7	Fitted background normalizations for $t\bar{t}$ and $W+\text{jets}$ backgrounds for the DY WZ analysis region.	134
12.8	Fitted background normalizations for $t\bar{t}$ and $W+\text{jets}$ backgrounds for the VBF WW analysis region.	134
12.9	Fitted background normalizations for $t\bar{t}$ and $W+\text{jets}$ backgrounds for the VBF WZ analysis region.	135

Abstract

Search for WW and WZ Resonances in $\ell\nu qq$ final states in pp collisions at

$\sqrt{s} = 13$ TeV with the ATLAS detector

by

Natasha Woods

This thesis presents a search for WW and WZ resonances using data from pp collisions at $\sqrt{s} = 13$ TeV using the ATLAS detector, corresponding to an integrated luminosity of 139 fb^{-1} . Diboson resonances are predicted in a number of Standard Model (SM) extensions, such as Extended Gauge Models, and Extra dimensional models. This search looks for resonances where one W boson decays leptonically and the other W or Z boson decays hadronically. This search is sensitive to diboson resonance production via vector-boson fusion as well as quark-antiquark annihilation and gluon-gluon fusion mechanisms. No significant excess of events is observed with respect to the Standard Model backgrounds, and constraints on the masses of new W' , Z' , and bulk-RS Gravitons are extended to up to 3.3 TeV, depending on the model. As the dominant backgrounds in this search contain gluons, classifying jets as quark-initiated or gluon-initiated would make this analysis more sensitive to new physics. Towards this end, this thesis provides a calibrated quark-gluon tagger based on the multiplicity of charged particles within a jet.

Loving Dedication

å

xix

Acknowledgments

Proper acknowledgments of everyone else who helped you graduate. Write later.

Part I

Introduction

³ Chapter 1

⁴ Introduction

⁵ In general, humanity has continually strived to understand the structure and
⁶ dynamics of reality for widely varying reasons. Each academic field uses a spe-
⁷ cific set of concepts and models to describe nature. Physics is one such field,
⁸ that uses mathematical objects to systematically develop testable models about
⁹ the universe. Currently, the most fundamental types particles are fermions and
¹⁰ bosons. Fermions are the particles that make up the "ordinary" matter of the
¹¹ universe, while bosons are the quanta of the fundamental forces. The Standard
¹² Model (SM) of particle physics describes the quantum behavior of three of the
¹³ four fundamental forces: electromagnetic, strong, and weak forces.

¹⁴ The Standard Model has consistently described much of reality to an extreme
¹⁵ degree of accuracy. It has predicted cross sections for strong and electroweak
¹⁶ processes that span over ten orders of magnitude [see Fig. 3.1] and contains no
¹⁷ known logical inconsistencies. Despite the reality of the Standard Model, it still
¹⁸ fails to describe aspects of reality and suffers from aesthetic issues. The SM fails
¹⁹ to account for dark matter, dark energy, neutrino masses, the hierarchy of the
²⁰ fundamental force strengths, and other issues that may have not been noticed
²¹ yet! This incompleteness may indicate that a more fundamental theory exists. It

22 is hoped that such a theory would address the aforementioned phenomena and
23 the ad-hoc structure and parameter values of the SM. In particular the relative
24 scales of the fundamental forces impose oddly fine-tuned SM parameters, unless
25 there is additional structure at higher energies (e.g. between the electroweak and
26 Planck scales). This and other theoretical arguments motivate the search for new
27 physics at the TeV scale. The set of theories that hope to explain more of reality
28 are known as Beyond the Standard Model theories (BSM). Many of these theories,
29 if true, would revolutionize concepts of symmetry and space-time, which would
30 be intrinsically meaningful.

31 To probe the physics at this high energy frontier, physicists often collide ener-
32 getic particles that combine to produce massive particles, such as the Higgs boson
33 and top quark. The more energetic the colliding particles are the more massive
34 produced particles can be. Currently, the world's highest energy particle collider
35 is the Large Hadron Collider (LHC) at the European Organization for Nuclear
36 Research (CERN).

37 This thesis presents a search for WW and WZ resonances using data from pp
38 collisions at $\sqrt{s} = 13$ TeV using the ATLAS detector at CERN, corresponding
39 to an integrated luminosity of 139 fb^{-1} . Diboson resonances are predicted in a
40 number of BSM theories, such as Extended Gauge Models and Extra dimensional
41 models. This search looks for resonances where one W boson decays leptonically
42 and the other W or Z boson decays hadronically. This search is sensitive to
43 diboson resonance production via vector-boson fusion as well as quark-antiquark
44 annihilation and gluon-gluon fusion mechanisms (which will be collectively called
45 non-VBF modes).

46 To search for these new resonances, Monte-Carlo simulations are used to model
47 SM backgrounds and BSM signals. In these simulations, a series of optimized cuts

48 are used to create signal regions (SR) to identify the leptonic and hadronic decay
49 products of the resonance, maximize signal acceptance, and minimize background
50 contamination. In these regions, the resonance mass is calculated as the combined
51 system mass of the leptonic and hadronic system. The expected resonance mass
52 distribution from the simulated backgrounds and anticipated signal are compared
53 to data to search for the existence of these BSM signals (also known as a "bump
54 hunt"). Control regions enriched in the dominant backgrounds, $t\bar{t}$ and $W+\text{jets}$
55 (TCR and WCR, respectively) are constructed to be orthogonal to SRs and used
56 to determine the normalization of the $t\bar{t}$ and $W+\text{jets}$ backgrounds in SRs.

57 The VBF W' and Z' and ggF W' and Z' resonances studied have unique
58 SR and CR selections to maximize analysis sensitivity. RS Graviton signals are
59 probed using the same selections as the ggF Z' signal. Additionally, more mas-
60 sive resonances are more likely to have boosted W/Z bosons. As the boost of
61 the hadronically decaying boson increases the separation of its hadronic decay
62 products decreases. When the hadronically decaying boson has sufficient boost,
63 the two quarks will overlap and not be identified separately. For this reason, a
64 set of "resolved" selections are used when the hadronic decay products are recon-
65 structed separately, and "merged" selections when the decay products overlap and
66 identified as a single object in the event. A W/Z tagger identifies merged jets as
67 originating from a W/Z bosons based on jet substructure and mass cuts. However,
68 the more boosted the jet is the less likely it is to pass the jet substructure cut, due
69 to track merging. Consequently, the merged selection uses a high purity region
70 (HP), which requires that the jet pass both cuts, and low purity (LP) region where
71 the jet can fail the jet substructure cut.

72 The aforementioned SR definitions veto events with b -jets to minimize $t\bar{t}$ con-
73 tamination. However, b -jets are anticipated from W' resonances from the hadron-

74 ically decaying Z boson. To increase the signal acceptance of these resonances,
75 a $Z \rightarrow bb$ tagger is used to construct additional SR and CRs called the "tagged"
76 regions (and "un>tagged" if the event fails the $Z \rightarrow bb$ tagger).

77 For each signal model, the simulated and measured resonance mass distribu-
78 tions in the relevant SR and CRs are combined to construct a likelihood. This
79 likelihood is parameterized by the signal strength parameter, μ and systematic
80 uncertainties of the resonance mass distribution. This likelihood is used to quan-
81 tify the likelihood of a certain signal model given the anticipated backgrounds and
82 measured data.

83 No significant excess of events is observed with respect to the Standard Model
84 backgrounds, and constraints on the masses of new W' , Z' , and bulk-RS Gravi-
85 tons are extended to up to 3.3 TeV, depending on the model. As the dominant
86 backgrounds in this search contain gluons, classifying jets as quark-initiated or
87 gluon-initiated would improve the sensitivity of this analysis to new physics. To-
88 wards this end, this thesis provides a calibrated quark-gluon tagger based on the
89 multiplicity of charged particles within a jet.

90 Part II reviews the SM, its successes and shortcomings, and the aforemen-
91 tioned BSM theories that address the incompleteness of the SM. The structure
92 and performance of the ATLAS detector used is given in Part III. Part IV summa-
93 rizes the search for the diboson resonances using ATLAS data from pp collisions
94 at $\sqrt{s} = 13$ TeV. Finally, Part V examines the prospects for a quark gluon tagger
95 based on the track multiplicity of jets and details the calibration of this tagger.

Part II

96

Theoretical Motivation

97

₉₈ **Chapter 2**

₉₉ **The Standard Model of Particle**

₁₀₀ **Physics**

₁₀₁ **2.1 Introduction**

₁₀₂ By determining the dynamics of the most elementary degrees of freedom, par-
₁₀₃ ticle physics hopes to uncover the fundamental laws of the universe. The definition
₁₀₄ of elementary has evolved through time and currently refers to matter and force
₁₀₅ mediating particles: fermions and bosons, respectively. The Standard Model of
₁₀₆ Particle Physics (SM) describes the quantum behavior of three of the four funda-
₁₀₇ mental forces: weak, strong, and electromagnetic, via boson and fermion interac-
₁₀₈ tions. Gravity is not included in the SM and still under investigation.

₁₀₉ **2.2 Quantum Field Theory**

₁₁₀ In the SM, forces (and particles) are represented as fields. In this context,
₁₁₁ fields are mathematical objects that define a tensor (e.g. scalar, vector, etc) at
₁₁₂ every point on a manifold, here the manifold is space-time. These fields obey laws

₁₁₃ dictated by Quantum Field Theory (QFT). Particles arise naturally in QFT as
₁₁₄ quantized field excitations localized in spacetime.

₁₁₅ According to Noether's theorem, symmetries of a field give rise to conserved
₁₁₆ quantities (e.g. time-translation invariance leads to energy conservation). Often
₁₁₇ in the history of physics, a conserved quantity of a field is found and then the
₁₁₈ underlying symmetry of the field is inferred. Gauge symmetries are symmetries
₁₁₉ among the internal degrees of freedom of the field (components of the tensor),
₁₂₀ which give rise to quantities associated with fields. By specifying the symmetries
₁₂₁ of a system the dynamics and conserved quantities of the system may be succinctly
₁₂₂ defined.

₁₂₃ 2.3 $U(1)_{EM}$ Local Gauge Invariance

₁₂₄ The Lagrangian of Quantum Electrodynamics (QED) describes the electro-
₁₂₅ magnetic force. QED may be derived by requiring local $U(1)_{EM}$ gauge invariance
₁₂₆ of the free dirac fermion Lagrangian, ψ :

$$\mathcal{L} = i\bar{\psi}\gamma^\mu\partial_\mu\psi - m\bar{\psi}\psi \quad (2.1)$$

₁₂₇ This symmetry may be represented as a complex number with unit modulus,
₁₂₈ $e^{i\theta}$. $U(1)$ gauge invariance requires this gauge transformation of ψ will leave the
₁₂₉ Lagrangian unchanged.

$$\psi(x) \rightarrow \psi'(x) = e^{i\theta(x)}\psi(x) \quad (2.2)$$

₁₃₀ NB: This transformation is a local gauge transformation as θ depends on the
₁₃₁ spacetime coordinate.

₁₃₂ By requiring this symmetry of the free Dirac fermion Lagrangian:

$$\mathcal{L} = i\bar{\psi}\gamma^\mu\partial_\mu\psi - m\bar{\psi}\psi \quad (2.3)$$

¹³³ The mass term is unaffected, but the kinetic term is modified due to $\theta(x)$.

$$\mathcal{L} \rightarrow \mathcal{L}' = i\bar{\psi}e^{-i\theta(x)}\gamma^\mu\partial_\mu\psi e^{i\theta(x)} - m\bar{\psi}e^{-i\theta(x)}\psi e^{i\theta(x)} \quad (2.4)$$

¹³⁴

$$= i\bar{\psi}\gamma^\mu(\partial_\mu\psi + i\psi\partial_\mu\theta) - m\bar{\psi}\psi \quad (2.5)$$

¹³⁵ The $\partial_\mu\theta$ terms breaks the gauge invariance of the Lagrangian. By introducing a
¹³⁶ new field, A_μ we can recover the gauge invariance of the derivative. Now redefining
¹³⁷ the derivative as the covariant derivative:

$$D_\mu\psi \equiv (\partial_\mu - iqA_\mu)\psi \quad (2.6)$$

¹³⁸ And letting A_μ transform under $U(1)$ as:

$$A_\mu \rightarrow A_\mu + \delta A_\mu \quad (2.7)$$

¹³⁹ The transformed covariant derivative becomes:

$$D_\mu\psi \rightarrow D_\mu\psi' = (\partial_\mu - iqA_\mu)\psi' \quad (2.8)$$

¹⁴⁰

$$= (\partial_\mu - iq(A_\mu + \delta A_\mu))\psi e^{i\theta} \quad (2.9)$$

¹⁴¹

$$= e^{i\theta}D_\mu + ie^{i\theta}\psi(\partial_\mu\theta - q\delta A_\mu) \quad (2.10)$$

¹⁴² The covariant derivative can be made gauage invariant by setting the last term
¹⁴³ to zero.

$$\delta A_\mu = \frac{1}{q} \partial_\mu \theta \quad (2.11)$$

¹⁴⁴ So now A_μ transforms as:

$$A_\mu \rightarrow A_\mu + \frac{1}{q} \partial_\mu \theta \quad (2.12)$$

¹⁴⁵ Finally, replacing the derivative with the covariant derivative the Dirac La-
¹⁴⁶ grangian we have:

$$\mathcal{L} = i\bar{\psi}\gamma^\mu D_\mu \psi - m\bar{\psi}\psi - \frac{1}{4}F_{\mu\nu}F^{\mu\nu} \quad (2.13)$$

¹⁴⁷

$$= \mathcal{L}_{QED} \quad (2.14)$$

¹⁴⁸ Here $F_{\mu\nu} \equiv \partial_\mu A_\nu - \partial_\nu A_\mu$. This last term in the Lagrangian is the kinetic
¹⁴⁹ energy of the gauge boson field.

¹⁵⁰ So we have derived the QED Lagrangian. By requiring the free Dirac La-
¹⁵¹ grangian to be invariant under local U(1) transformations we have generated a
¹⁵² new gauge boson field, A_μ , which describes the photon. As expected the photon
¹⁵³ interacts with fermions.

¹⁵⁴ Stepping back, a global U(1) gauge symmetry of the free Dirac Lagrangian
¹⁵⁵ implies we cannot measure the absolute phase of a charged particle. A local U(1)
¹⁵⁶ gauge symmetry changes the phase of fields differently across space time. For this
¹⁵⁷ type of transformation to leave the Lagrangian invariant, we had to introduce an
¹⁵⁸ additional field, A_μ , which "communicates" these phase changes across space-time.
¹⁵⁹ In less formal language this effectively means: if the field at one location changes,
¹⁶⁰ this change is conferred to other particles via A_μ .

¹⁶¹ 2.4 Yang-Mills Gauge Theories

¹⁶² Requiring $U(1)_{EM}$ gauge invariance of the free Dirac Lagrangian gave us QED.

¹⁶³ Requiring different gauge symmetries we can derive the structure of other inter-

¹⁶⁴ actions. Any gauge symmetry may be written as:

$$\psi_i \rightarrow \exp(i\theta^a T_{ij}^a) \psi_j \quad (2.15)$$

¹⁶⁵ Here θ is a dimensionless real parameter and T is the generator of the gauge

¹⁶⁶ symmetry group. With this the covariant derivative can be written as:

$$D_\mu \psi_i \equiv \partial_\mu \psi_i + ig A_\mu^a T_{ij}^a \psi_j \quad (2.16)$$

¹⁶⁷ Then the gauge field must transform as:

$$A_\mu^a \rightarrow A_\mu^a - \frac{1}{g} \partial_\mu \theta^a - f^{abc} \theta^b A_\mu^c \quad (2.17)$$

¹⁶⁸ Here f is the structure constant of the gauge group. The field strength tensor

¹⁶⁹ is given by:

$$F_{\mu\nu}^a \equiv \partial_\mu A_\nu^a - \partial_\nu A_\mu^a - g f^{abc} A_\mu^b A_\nu^c \quad (2.18)$$

¹⁷⁰

$$F_{\mu\nu}^a \rightarrow F_{\mu\nu}^a - f^{abc} \theta^b F_{\mu\nu}^c \quad (2.19)$$

¹⁷¹ This gives the Yang-Mills Lagrangian:

$$\mathcal{L}_{YM} = -\frac{1}{4} F_{\mu\nu}^{a\mu\nu} F_{\mu\nu}^a + i \bar{\psi}_i \gamma^\mu D_\mu \psi_i + m \bar{\psi}_i \psi_i \quad (2.20)$$

¹⁷² 2.5 Particles in the Standard Model

¹⁷³ The SM consists of fermions (half-integer spin matter constituents) and bosons
¹⁷⁴ (integer spin force mediators). Fermions are spinor representations of the Poincare
¹⁷⁵ group and can be further separated into leptons and quarks. Bosons are the result
¹⁷⁶ of requiring a particular symmetry among the spinor fields:

$$SU(3)_C \times SU(2)_L \times U(1)_Y \quad (2.21)$$

¹⁷⁷ $SU(3)_C$ is the symmetry group of the strong force and generates eight gluon
¹⁷⁸ fields, G_μ . $SU(2)_L$ is the symmetry group of the Electroweak force and generates
¹⁷⁹ three electroweak boson fields. The mixing of this $SU(2)_L$ and $U(1)_Y$ gives rise
¹⁸⁰ to the photon field, where Y is the weak-hypercharge:

$$Y = 2(Q - T_3) \quad (2.22)$$

¹⁸¹ Q is the electromagnetic charge, and T_3 is the z-component of the weak isospin.
¹⁸² Weak isospin is the charge associated with the $SU(2)_L$ symmetry. The correspond-
¹⁸³ ing covariant derivative is then:

$$D_\mu \phi \equiv (\partial_\mu + ig_1 B_\mu Y_{L/R} + [ig_2 W_\mu^\alpha T^\alpha]_L + [ig_3 G_\mu^\alpha \tau^\alpha]_C) \psi \quad (2.23)$$

¹⁸⁴ It is important to note that the gauge symmetry of the SM yields a particular
¹⁸⁵ structure of the fermion representations. So for a given fermion to interact with
¹⁸⁶ a given gauge field it must have a non-zero corresponding Noether charge for
¹⁸⁷ that gauge symmetry. If the corresponding Noether charge is zero, that fermion
¹⁸⁸ transforms as a singlet and does not participate in that gauge interaction.

¹⁸⁹ Fermions are divided into quarks and leptons based on their transformations
¹⁹⁰ under $SU(3)_C$. Quarks transform as color triplets. Leptons transform as color

singlets and consequently do not interact with gluons. Fermions may be further
 classified by their $SU(2)_L$ interactions. Only the left-chiral part of fermions (denoted by L here) transform as $SU(2)_L$ doublets, the right-chiral part forms singlets under this gauge. Lastly, all these groups of particles come in three generations, each a heavier copy of the previous, but with differing flavor quantum numbers.
 This is summarized in Table 2.1 and shown in Figures 2.1 and 2.2.

SM Fermion Gauge Group	First Generation	Second Generation	Third Generation	$(SU(3)_C, SU(2)_L, U(1)_Y)$ Representations
Left-handed quarks	$\begin{pmatrix} u_L^r & u_L^g & u_L^b \\ d_L^r & d_L^g & d_L^b \end{pmatrix}$	$\begin{pmatrix} c_L^r & c_L^g & c_L^b \\ s_L^r & s_L^g & s_L^b \end{pmatrix}$	$\begin{pmatrix} t_L^r & t_L^g & t_L^b \\ b_L^r & b_L^g & b_L^b \end{pmatrix}$	$(3, 2, \frac{1}{6})$
Right-handed quarks	(u_R^r, u_R^g, u_R^b) (d_R^r, d_R^g, d_R^b)	(c_R^r, c_R^g, c_R^b) (s_R^r, s_R^g, s_R^b)	(t_R^r, t_R^g, t_R^b) (b_R^r, b_R^g, b_R^b)	$(3, 1, \frac{2}{3})$ $(3, 1, -\frac{1}{3})$
Left-handed leptons	$\begin{pmatrix} \nu_e^L \\ e_L \end{pmatrix}$	$\begin{pmatrix} \mu_e^L \\ \mu_L \end{pmatrix}$	$\begin{pmatrix} \tau_e^L \\ \tau_L \end{pmatrix}$	$(1, 2, -\frac{1}{2})$
Right-handed leptons	e_R	μ_R	τ_R	$(1, 1, -1)$

Table 2.1: Representations of the SM fermions under $SU(3)_C \times SU(2)_L \times U(1)_Y$ gauge symmetry group. Rows are correspond to different weak isospin states and columns to different QCD color states.

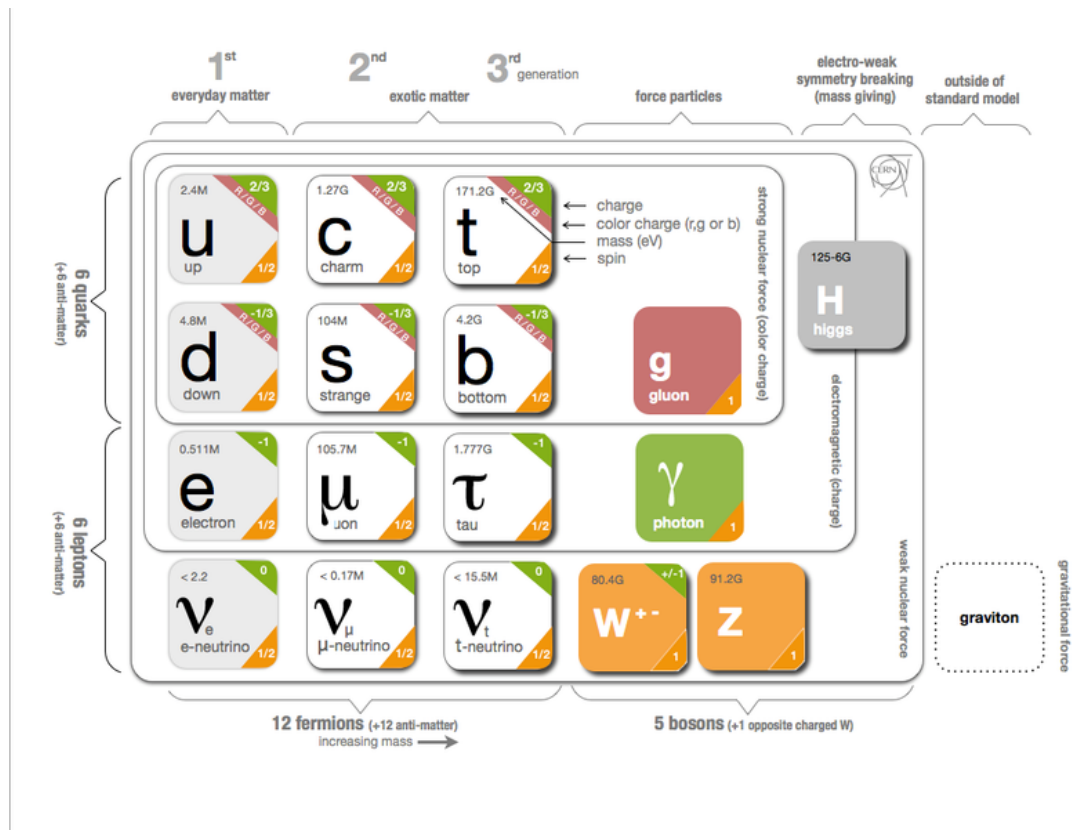


Figure 2.1: The particles of the Standard Model.



Figure 2.2: Summary of how Standard Model particles interact with other Standard Model particles.

197 Now we can understand the SM Lagrangian density as a Yang-Mills theory
 198 with the gauge group: $SU(3)_C \times SU(2)_L \times U(1)_Y$ with an additional $SU(2)$ complex
 199 scalar Higgs field doublet that will be discussed later.

$$\begin{aligned} \mathcal{L}_{SM} = & \underbrace{-\frac{1}{4}B_{\mu\nu}B^{\mu\nu} - \frac{1}{4}W_{\mu\nu}^a W^{a\mu\nu} - \frac{1}{4}G_{\mu\nu}^\alpha G^{\alpha\mu\nu}}_{\text{Kinetic Energies and Self-Interactions of Gauge Bosons}} \\ & + \underbrace{\bar{L}_i \gamma^\mu (i\partial_\mu - \frac{1}{2}g_1 Y_{iL} B_\mu - \frac{1}{2}g_2 \sigma^a W_\mu^a) L_i}_{\text{Kinetic Energies and EW Interactions of Left-handed Fermions}} \\ & + \underbrace{\bar{R}_i \gamma^\mu (i\partial_\mu - \frac{1}{2}g_1 Y_{iR} B_\mu) R_i}_{\text{Kinetic Energies and EW Interactions of Right-Handed Fermions}} \\ & + \underbrace{\frac{ig_3}{2} \bar{Q}_j \gamma^\mu \lambda^\alpha G_\mu^\alpha Q_j}_{\text{Strong Interactions between Quarks and Gluons}} \\ & + \underbrace{\frac{1}{2} |(i\partial_\mu - \frac{1}{2}g_1 B_\mu - \frac{1}{2}g_2 \sigma^a W_\mu^a)\Phi|^2 - V(\Phi)}_{\text{Electroweak Boson Masses and Higgs Couplings}} \\ & - \underbrace{(y_{kl}^d \bar{L}_k \Phi R_l + y_{kl}^u \bar{R}_k \tilde{\Phi} L_l + h.c.)}_{\text{Fermion Mass terms and Higgs Couplings}} \end{aligned}$$

200 Here several abstract spaces are being spanned:

- 201 – a spans the three $SU(2)_L$ gauge fields with generators expanded in Pauli
 202 matrices, $T^\alpha = \frac{1}{2}\sigma^\alpha$
- 203 – α spans the eight $SU(3)_C$ gauge fields, with generators expanded in Gell-
 204 Mann matrices, $\tau^\alpha = \frac{1}{2}\lambda^\alpha$
- 205 – L/R represent left and right projections of Dirac fermion fields. The Strong
 206 interaction is not chiral, so $Q = L+R$

- 207 – μ and ν are four-vector indices
- 208 – i, j, k are summed over the three generations of SM particles.

209 2.6 Higgs Mechanism

210 The SM Lagrangian without the addition of a Higgs field does not allow for
211 gauge boson and fermion mass terms: $\frac{1}{2}m_A^2 A_\mu A_\mu$ and $m(\bar{\psi}\psi)$, as these terms are
212 not gauge invariant. By introducing the Higgs field, mass terms for these particles
213 may be included in a gauge invariant way. This field is a complex doublet with a
214 potential $V(\Phi)$:

$$\Psi = \begin{pmatrix} \Phi^\dagger \\ \Phi^0 \end{pmatrix} \quad (2.24)$$

215

$$V(\Phi) = \mu^2 \Phi^\dagger \Phi + \lambda |\Phi^\dagger \Phi|^2 \quad (2.25)$$

216 The minima of this field occurs for $|\Phi| = \sqrt{\frac{\mu^2}{2\lambda}} \equiv \frac{v}{2}$. This yields degenerate
217 minima, this symmetry is broken by choosing a specific minima (a.k.a. sponta-
218 neous symmetry breaking). By convention $\Phi_{min} = \frac{1}{\sqrt{2}} \begin{pmatrix} 0 \\ v \end{pmatrix}$ is chosen. This means
219 the ground state of the Higgs field (Higgs vacuum) is non-zero, $\sqrt{\frac{-\mu^2}{\lambda}}$. The Higgs
220 Field may now be expanded around this new ground state:

$$\Phi(x) = \frac{1}{\sqrt{2}} \begin{pmatrix} 0 \\ v + h(x) \end{pmatrix} \quad (2.26)$$

221 This non-zero Higgs vacuum now generates mass terms for the gauge bosons
222 from the following term in the Lagrangian:

$$|(-\frac{1}{2}g_1B_\mu - \frac{1}{2}g_2\sigma^aW_\mu^a)\Phi|^2 = \frac{1}{2}m_W^2W_\mu^+W^{-\mu} + \frac{1}{2}m_Z^2Z_\mu Z^\mu \quad (2.27)$$

223 where:

$$W_\mu^\pm \equiv \frac{1}{\sqrt{2}}(W_\mu^1 \mp iW_\mu^2) \quad (2.28)$$

$$\begin{aligned} \text{224} \quad Z_\mu &\equiv \frac{1}{\sqrt{g_1^2 + g_2^2}}(g_2W_\mu^2 - g_1B_\mu) \end{aligned} \quad (2.29)$$

$$\begin{aligned} \text{225} \quad m_W &= \frac{vg_2}{\sqrt{2}} \end{aligned} \quad (2.30)$$

$$\begin{aligned} \text{226} \quad m_Z &= \frac{v}{\sqrt{2}}\sqrt{g_1^2 + g_2^2} \end{aligned} \quad (2.31)$$

227 The Higgs field also generates a mass term for the Higgs boson and self-
228 interactions for the Higgs boson.

229 2.7 Electroweak Theory

230 $SU(2)_L$ generates W^\pm, W^0 gauge bosons, which would be massless if $SU(2)_L$
231 was a perfect symmetry. These bosons are massive as this symmetry is broken.

232 The mass eigenstates, Z and γ given by:

$$\begin{pmatrix} Z_\mu \\ A_\mu \end{pmatrix} = \begin{pmatrix} \cos\theta_W & -\sin\theta_W \\ \sin\theta_W & \cos\theta_W \end{pmatrix} \begin{pmatrix} W_\mu^3 \\ B_\mu \end{pmatrix} \quad (2.32)$$

233 Here θ_W is the Weinberg angle given by:

$$\cos\theta_W = \frac{g_2}{\sqrt{g_1^2 + g_2^2}} = \frac{m_W}{m_Z} \quad (2.33)$$

²³⁴ 2.8 Quantum ChromoDynamics

²³⁵ As mentioned earlier the Strong Force, which binds the proton together, is
²³⁶ mediated by gluons. Quantum Chromodynamics is the QFT which describes the
²³⁷ interactions of quarks and gluons via $SU(3)_C$ symmetry. QCD contains features
²³⁸ not present in Electroweak Interactions due to $SU(3)_C$ generators not commuting
²³⁹ (a.k.a. $SU(3)_C$ is a non-abelian group) and the number of quark flavors (n_f).
²⁴⁰ For example, in QCD there is color confinement and asymptotic freedom due to
²⁴¹ the structure constants being non-zero. Requiring $SU(3)_C$ local gauge invariance
²⁴² implies:

$$\psi(x) \rightarrow \psi(x)' = \exp[i g_S \alpha(x) \cdot \hat{T}] \psi(x) \quad (2.34)$$

²⁴³ where $\alpha(x)$ is the local phase function, g_S is the strong coupling constant, and
²⁴⁴ \hat{T} are the eight generators of $SU(3)$ (note $\hat{T}^a = \frac{1}{2}\lambda^a a$, where λ^a are the Gell-Mann
²⁴⁵ matrices). As the Gell-Mann matrices are 3x3, this means ψ has three degrees of
²⁴⁶ freedom under these $SU(3)$ rotations. So we represent ψ under $SU(3)$ rotations
²⁴⁷ as:

$$\psi = \begin{pmatrix} \psi_{red} \\ \psi_{green} \\ \psi_{blue} \end{pmatrix} \quad (2.35)$$

²⁴⁸ Consequently, particle fields transforming under $SU(3)$ rotations have three
²⁴⁹ components which physicists describe as color components (red, green, and blue).
²⁵⁰ A particle's corresponding antiparticle has the corresponding anticolor. This color
²⁵¹ is the "charge" of QCD and is conserved under $SU(3)$ rotations. Combining colors,
²⁵² color neutral states (e.g. red and antired, or red, green and blue) may be created.
²⁵³ For the Free Dirac Lagrangian to remain invariant under $SU(3)$ transformations,

254 we must again postulate a boson field that modifies the derivative. The gluon
255 field tensor is given by ($\alpha = 1, \dots, 8$):

$$G_{\mu\nu}^k = \partial^\mu G_\alpha^\nu - \partial^\nu G_\alpha^\mu - g_S f^{\alpha\beta\gamma} G_\beta^\mu G_\gamma^\nu \quad (2.36)$$

256 Here $f^{\alpha\beta\gamma}$ are the structure constants of $SU(3)$. Combining all this gives the
257 QCD Lagrangian:

$$\mathcal{L}_{QCD} = \bar{\psi}_q i\gamma^\mu (D_\mu)_{ij} \psi^{qj} - m \bar{\psi}_q \psi_q - \frac{1}{4} G_{\mu\nu}^\alpha G^{\alpha\mu\nu} \quad (2.37)$$

258 Here i are the color indices, and q are the quark flavors. It is important to
259 note that quarks transform under the fundamental representation of $SU(3)$, while
260 gluons transform under the adjoint representation. This means quarks carry a
261 single color charge (red, green, blue, antired, antigreen, antiblue) and gluons carry
262 a color and anticolor charge.

263 Figure 2.3 shows the three dominant QCD interactions. Since gluons carry
264 color charge, they interact with one another. This does not occur in QED, as
265 photons do not have electric charge and therefore do not interact with each other.
266 In QED, a bare electron's effective charge is largest closest to the electron and
267 decreases as a function of distance. This is because the QED vacuum fills with
268 particle antiparticle pairs spontaneously, which screen the charge of the bare elec-
269 tron. The larger the distance from the electron, the smaller the effective charge
270 and therefore the weaker the force.

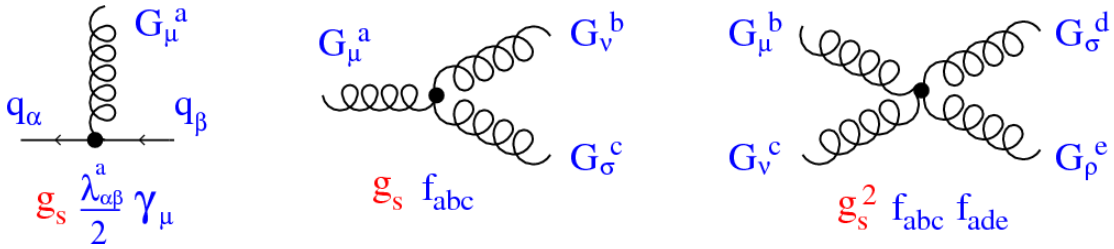


Figure 2.3: This figure shows the three dominant QCD interactions. From Ref. [18]

271 As the distance from a quark increases it's effective color charge increases due
 272 to the vacuum polarization in QCD. Color charge grows as the distance from
 273 the source increases (a.k.a. color is anti-screened in QCD). In this way, strong
 274 interactions become stronger at large distances (low momenta interactions). At
 275 small distances (large momenta interactions) strong interactions are significantly
 276 weaker and considered nearly free. This effect of referred to as asymptotic freedom.
 277 At large distances, a quark's effective charge is large and the strong force is more
 278 significant. This force becomes so strong that quarks form colorless bound states
 279 instead of remaining free particles. This effect is known as color confinement.
 280 This running of all SM fields is shown in Figure 2.4.



Figure 2.4: Strength of the U(1), SU(2), and SU(3) gauge couplings as a function of the energy scale of the interaction (Q). From Ref. [12]

Commonly the change in a particle's effective charge under a given force is quantified with $\beta(r) \equiv -\frac{de(r)}{d\ln r}$, where $e(r)$ is the effective charge of a given particle under a force. In QED this function is positive but in QCD this function is negative leading to confinement and asymptotic freedom. Moreover, one can calculate how the coupling (α) of a force varies with energies. (More deeply this amounts to incorporating renormalization and vacuum polarization in the boson propagators).

For QCD this is:

$$\alpha_s(Q^2) = \frac{\alpha_s(\mu^2)}{1 + \frac{\alpha_s(\mu^2)}{12\pi}(33 - 2n_f)\ln(Q^2/\mu^2)} \quad (2.38)$$

where Q is the momentum of the force is probed at, μ^2 is the renormaliza-

289 tion scale, n_f is the number of quark flavors. There are six quark flavors in SM
290 QCD, making $33 - 2n_f > 0$. This factor being positive and the $\ln(Q^2/\mu^2)$ being
291 in the denominator means that as Q^2 increases α_s decreases. So for large Q^2 , α_s
292 is small and SM QCD is asymptotically free, while for small Q^2 , α_s is large and
293 SM QCD is confined, as mentioned earlier.

294 As stated previously, quarks and gluons have not been observed in isolation.
295 Instead they form bound colorless states. Hadronization is the process by which
296 quarks and gluons form hadrons. The process of hadronization is still an active
297 area of research. One qualitative description is show in Figure 2.5. In this figure,
298 as two quarks separate the color field between them is restricted to a tube with
299 energy density of $1\text{GeV}/\text{fm}$. As they separate further, the energy in the color field
300 increases, until there is enough energy to produce $q\bar{q}$ pairs, which breaks the color
301 field. This process repeats until quarks and antiquarks have low enough energy
302 to form colorless hadrons. The resulting spray of hadrons is called a jet.

303 Since quarks and gluons carry different color charges, their respective jets have
304 different properties. As quarks carry only a single color charge (vs. gluons which
305 have color and anticolor charge), so their jets have less constituent particles. More
306 precisely, the Altarelli-Parisi splitting functions [3] contain a factor C_A for gluon
307 radiation off a gluon and C_F for gluon radiation off a quark ($C_A/C_F = 9/4$). These
308 color factors are the prefactor in the Feynman diagrams for these processes [1],
309 which leads to gluon jets having more constituents and therefore more tracks than
310 quark jets. Gluon jets also tend to have a larger radius with lower momentum
311 constituents than quarks. There are many novel techniques to distinguish quarks
312 from gluons. For this study the number of charged particles will be focused on.

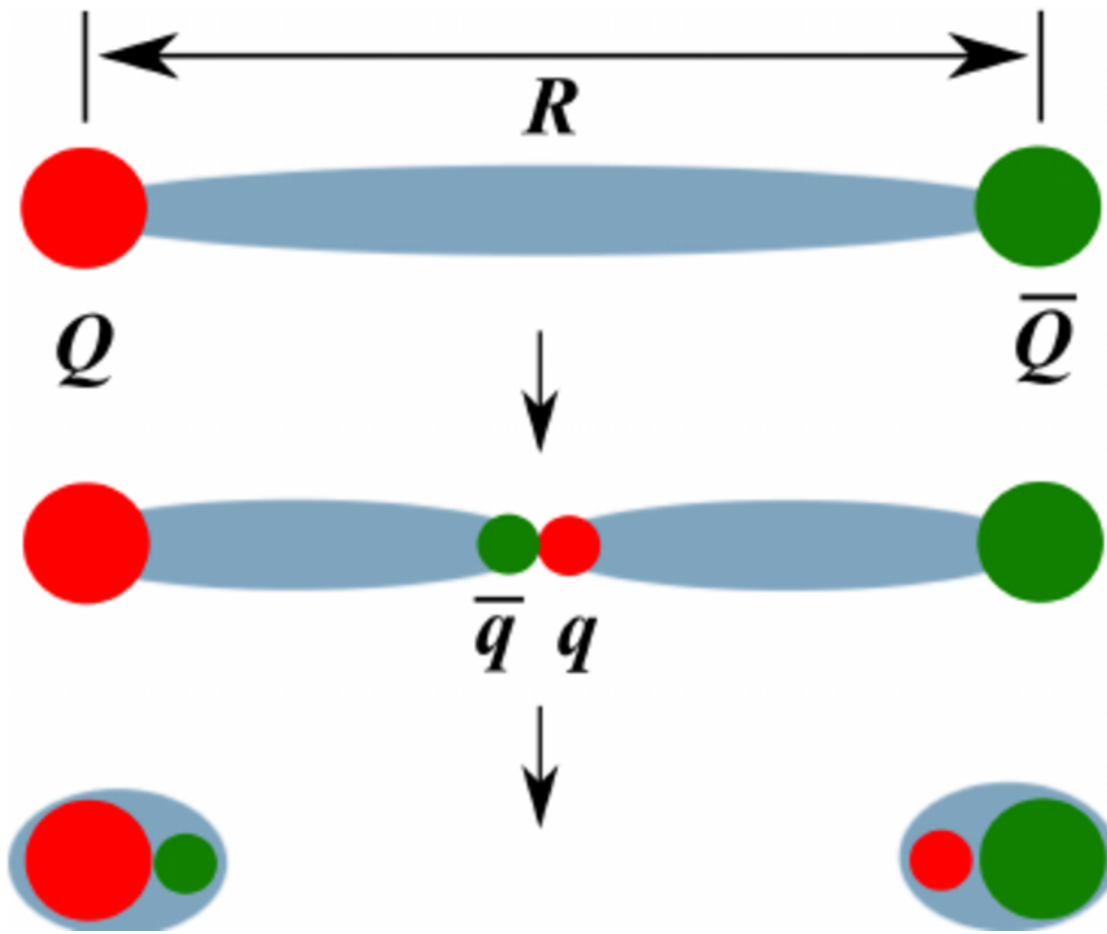


Figure 2.5: A cartoon of string breaking: the QCD string spanned between quark Q and antiquark \bar{Q} breaks due to $q\bar{q}$ creation [4]

³¹³ **Chapter 3**

³¹⁴ **Standard Model Successes and**

³¹⁵ **Limitations**

³¹⁶ The Standard Model has accurately described most of the underlying principles
³¹⁷ of nature. It has predicted cross sections for strong and electroweak processes that
³¹⁸ span over ten orders of magnitude correctly [see Fig. 3.1] and contains no known
³¹⁹ logical inconsistencies. Despite the strength and reality of the Standard Model, it
³²⁰ still fails to describe some important aspects of reality and suffers from aesthetic
³²¹ issues. To date, dark matter and energy comprise 95% of the universe, but are
³²² not accounted for in the SM. Additionally, neutrinos are known to have mass but
³²³ are massless in the SM. There are mechanisms for introducing massive neutrinos
³²⁴ in the SM, but these mechanisms create hierarchy problems.

³²⁵ Possibly the most significant aesthetic issue is the hierarchy between the elec-
³²⁶ troweak and Planck scales. The electroweak scale is the scale of electroweak
³²⁷ symmetry breaking. The Planck scale is the scale where the gravitational force
³²⁸ is comparable in strength to the other forces. The Planck scale is where the SM
³²⁹ breaks down, as there is not an experimentally verified theory of quantum gravity,
³³⁰ and at this scale gravity cannot be ignored (like it can at the electro-weak scale).

331 These scales differ by ~ 30 orders of magnitude. Understanding the difference
332 in these energy scales may help explain the weakness of gravity at electroweak
333 scales, and possibly a QFT for gravity. (NB: This hierarchy can also be framed in
334 terms of the corrections to the Higgs mass, which depend on the UV cutoff scale -
335 where the SM is suppose to break, which is taken at the Planck scale. This leads
336 the quantum corrections to the Higgs mass that would force the Higgs mass to
337 $\sim 10^{18}$ TeV.)

338 These stark contrasts in scales may indicate that a more fundamental theory
339 exists. It is hoped that such a theory would explain and motivate some of the
340 ad-hoc features of the SM. In particular, the values of the 19 SM parameters (6
341 quark masses, 3 charged lepton masses, 3 gauge couplings, Higgs parameters (μ^2 ,
342 λ)), the structure of the fermion representations, etc.

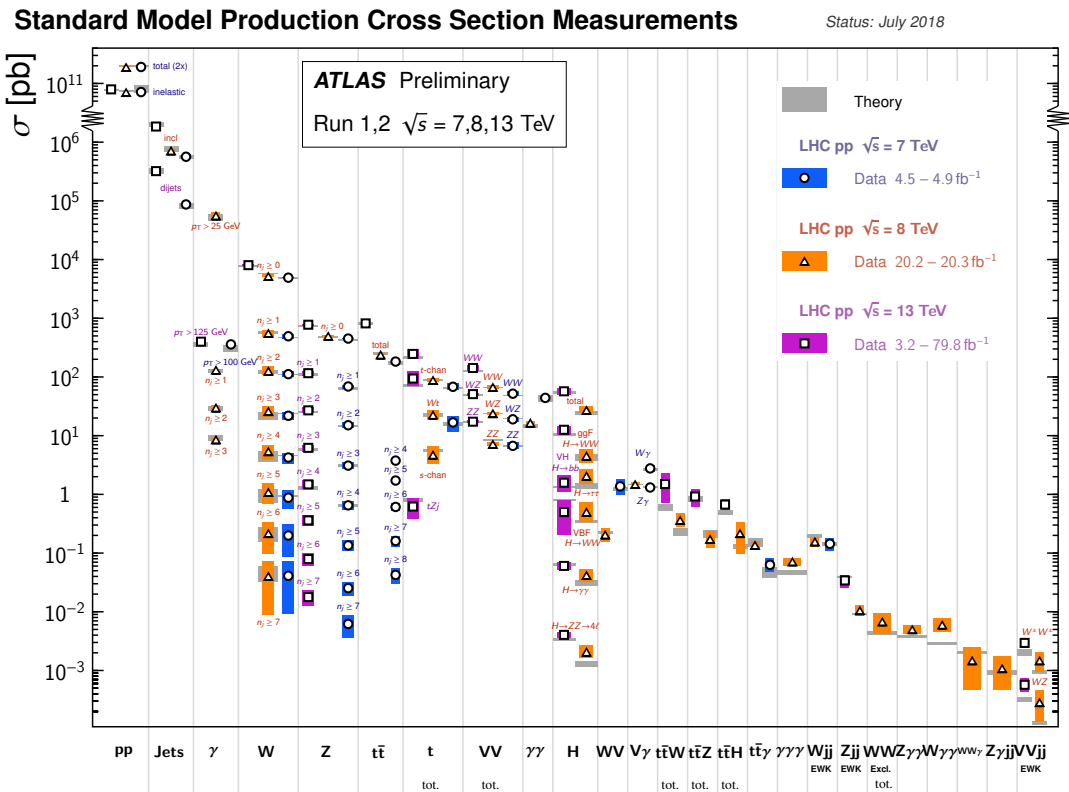


Figure 3.1: A comparison of cross section measurements at $\sqrt{s} = 7,8,13$ TeV from ATLAS compared to theoretical measurements. From Ref. [6]

³⁴³ **Chapter 4**

³⁴⁴ **New Physics Models with**

³⁴⁵ **Diboson Resonances**

³⁴⁶ **4.1 Randall Sundrum Bulk Model**

³⁴⁷ The electroweak-planck hierarchy may be explained by the existence of extra
³⁴⁸ dimensions, like the 5D Randall Sundrum Bulk Model ([19], [2]). In this model,
³⁴⁹ there is one extra warped spatial dimension, y , with a metric:

$$ds^2 = e^{-2k|y|} \eta_{\mu\nu} dx^\mu dx^\nu + dy^2 \quad (4.1)$$

³⁵⁰ where $e^{-k|y|}$ is the warp factor of the extra dimension, which is compactified on
³⁵¹ a S^1/Z_2 orbifold (a.k.a. a circle where $y \rightarrow -y$). This can be visualized as every
³⁵² point in space time having a line extending from it a distance L , representing
³⁵³ this fifth dimension. At the end of this line is the Planck brane. This fourth
³⁵⁴ spatial dimension separates two 4-D branes: Planck brane and TeV brane. We
³⁵⁵ live on the TeV brane, as shown in Figure 4.1. The Higgs field (and to a lesser
³⁵⁶ degree the top quark and graviton fields) is localized near the TeV Brane, while

357 the light fermion fields are localized more near the Planck brane. Fundamental
 358 parameters are set on the Planck brane. The warp factor may be scaled away from
 359 all dimensionless SM terms by field redefinitions. However, the only dimensionful
 360 parameter, $m_H^2 = v^2$ is rescaled by $\tilde{v} \sim e^{-kL} M_{Pl} \sim 1\text{TeV}$ for $kL \sim 35$, explaining
 361 why gravity is so weak on the TeV brane. Also, by localizing the light fermion
 362 fields near the Planck brane and top and graviton fields near the TeV brane, the
 363 light quarks will have smaller masses.

364 The two free parameters of this theory are M_{Pl} and k . Based on this RS Bulk
 365 model, all SM particles should have Kaluza-Klein (KK) excitations. In particular,
 366 the graviton would have KK excitations that prefer to decay to WW or ZZ, which
 367 is why this analysis searches for RS Gravitons.

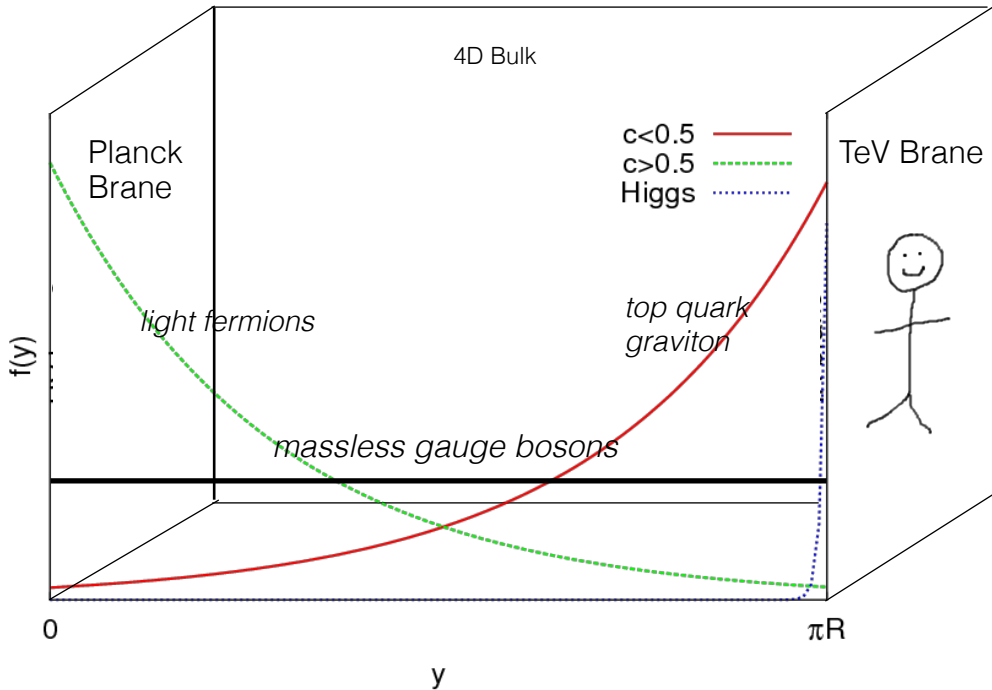


Figure 4.1: Cartoon of RS Bulk Model

368 4.2 Simple Standard Model Extensions

369 The RS Bulk model is motivated by resolving SM hierarchies, but it does not
370 address all of the other SM issues. There are many other interesting and well
371 motivated new physics frameworks that address these issues, but there is a lack
372 of completely predictive models, due to model flexibility (free parameters). It is
373 difficult for experimentalists to know which theories to search for in data. There-
374 fore, developing a model-independent resonance search that can be reinterperted
375 in the context of a given BSM theory is ideal.

376 This search is sensitive to the resonance mass and its interactions, but not
377 all of a given BSM model's parameters. Therefore, the BSM Lagrangian may be
378 reduced to only retain this information (mass parameters and couplings) following
379 the procedure in [17]. In this simplified approach, the new resonance searched for
380 is represented as an additional heavy vector triplet (HVT), which is a real vector
381 field in the adjoint representation of $SU(2)_L$ with vanishing hypercharge. This
382 results in one neutral and two charged bosons, defined as:

$$V^\pm = \frac{V_\mu^1 \mp i V_\mu^2}{\sqrt{2}} \quad (4.2)$$

$$V_\mu^0 = V_\mu^3 \quad (4.3)$$

384 The SM Lagrangian is then augmented with the additional terms:

$$\mathcal{L} \supset -\frac{1}{4} D_{[\mu} V_{\nu]}^a D^{[\mu} V^{\nu]}_a + \frac{m_V^2}{2} V_\mu^a V^{a\mu} + ig_V c_H V_\mu^a H^\dagger \tau^a \overset{\leftrightarrow}{D}{}^\mu H + \frac{g^2}{g_V} c_F V_\mu^a J_F^{\mu a} \quad (4.4)$$

385 In order the terms represent: the kinetic, V mass, Higgs- V interaction, and
386 V -left-handed fermion interaction terms. The g_V coupling factor determines the
387 coupling of the new resonance to left-handed fermions and the Higgs boson.

388 As benchmark models, this search considers resonances from extended gauge
389 symmetry (EGM) and composite Higgs models as discussed in [17] . The EGM
390 model predicts weakly coupled resonances, where $g_V = 1$, referred to later as
391 Model A. The composite Higgs Model is a strongly coupled model, where $g_V = 3$,
392 and later referred to as Model B. As shown in Eq. 4.4, the coupling of these
393 resonances to fermions scales as $g_f = g^2 c_F / g_V$, where g is the SM $SU(2)_L$ gauge
394 coupling and c_F is a free parameter. This then means that for Model B the
395 coupling to fermions is suppressed relative to Model A, leading to a smaller DY
396 production rate and branching ratio (BR) to fermionic final states. The coupling
397 of V to SM bosons scales as $g_H = g_V c_H$, where c_H is a free parameter on the
398 order of one for Model A and B. Consequently Model A resonances have a smaller
399 the BR to gauge bosons than Model B. For the pp collision data used, Model A
400 predicts larger production cross sections decaying to leptons and fermions than
401 Model B which decays primarily to gauge bosons.

402 Model A and B vectors are produced via quark-anti-quark annihilation and
403 the more rare vector-boson-fusion is considered by setting $g_H = 1$ and $g_F = 0$.
404 Both production modes are probed in this resonance search.

405 In summary, V couples most strongly to left-handed fermions and VV depen-
406 dent on g_V .

407

Part III

408

Experimental Setup

409 **Chapter 5**

410 **LHC**

411 The Large Hadron Collider (LHC) is the highest-energy particle collider in the
412 world. It was designed to expand the frontier of high energy particle collisions in
413 energy and luminosity. This enables LHC experiments to test the Standard Model
414 and search for new physics at higher energies than tested with previous colliders.
415 Collisions at higher energies not only produce more massive particles but also
416 more weakly interacting particles. Fig. 5.1 shows production cross sections for
417 various processes at hadron colliders. The rate for electroweak physics processes
418 including W and Z scale with the center-of-momentum energy, \sqrt{s} .

419 The LHC consists of a 26.7 km (17 miles) ring, approximately 100 m un-
420 derground, outside Geneva, Switzerland. Counter-circulating proton (and occa-
421 sionally heavy ions) beams collide inside four experiments along the beam line:
422 ATLAS, CMS, LHCb, ALICE. ATLAS and CMS are general purpose detectors de-
423 signed to explore the high energy frontier. LHCb is designed to study the physics
424 of b -quarks. ALICE specializes in studying heavy ion collisions.

proton - (anti)proton cross sections

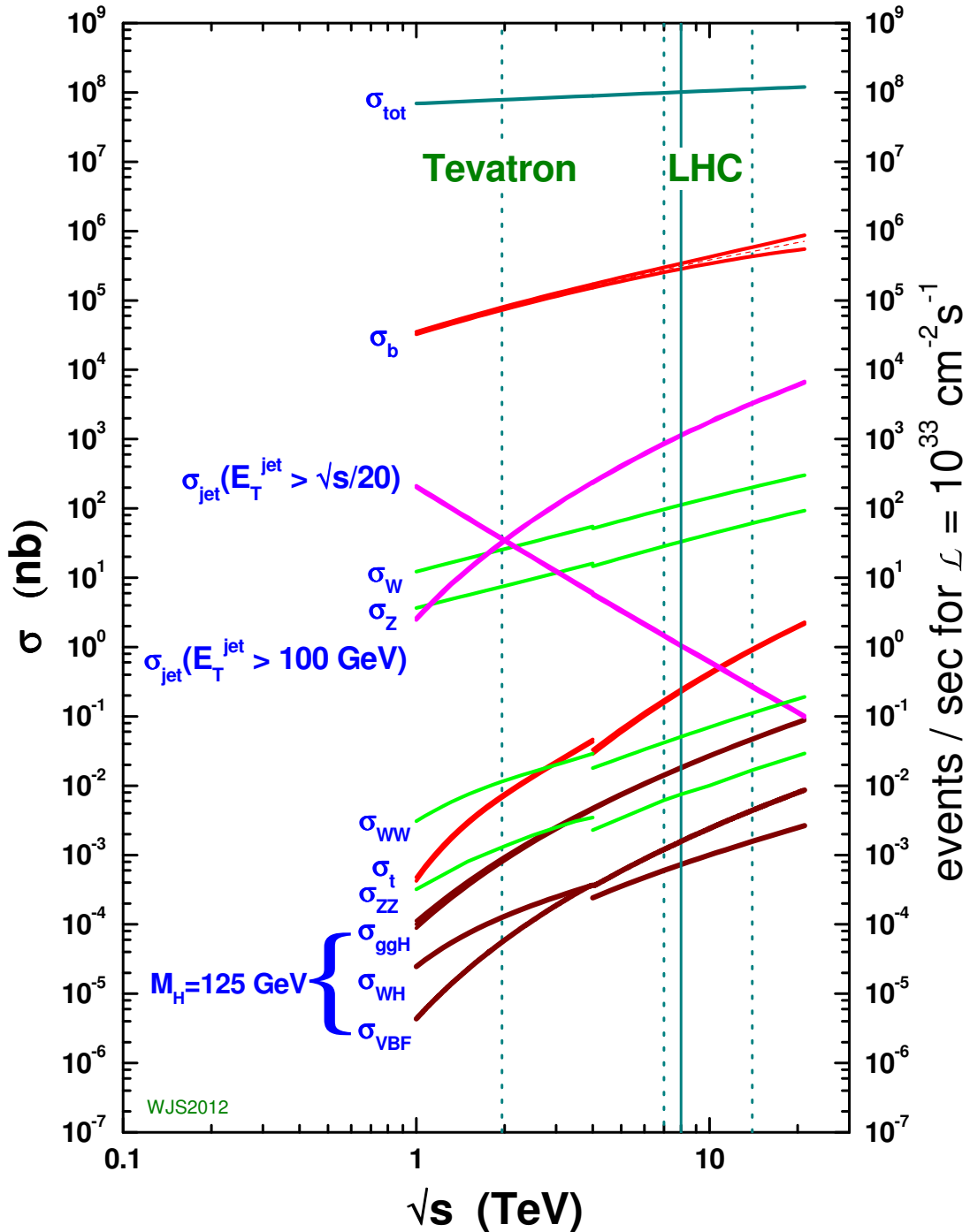


Figure 5.1: Scaling of cross sections with \sqrt{s} . Natasha: write more here

425 The first proton beams circulated in September, 2008. Nine days later an elec-
426 trical fault lead to mechanical damage and liquid helium leaks in the collider. This
427 incident delayed further operation until November 2009, when the LHC became
428 the world's highest energy particle collider, at 1.18TeV per beam. This first oper-
429 ational run continued until 2013, reaching 7 and 8 TeV collision energies. During
430 this run a particle with properties consistent with the Standard Model Higgs bo-
431 son was discovered. The next run began after a two year shutdown after upgrades
432 to the LHC and experiments. This run lasted from 2013 to 2018 reaching 13 TeV
433 collision energies. This analysis uses data from the second operational run.

434 5.1 LHC Layout and Design

435 The layout of the LHC is shown in Figure 5.2. The red and blue lines in the
436 figure represent the counter-circulating proton beams. The LHC is divided into
437 eight octants. Octant 4 contains the RF cavities that accelerate the protons and
438 octant 6 contains the beam dump system. Octants 3 and 7 house the collimation
439 systems for beam cleaning. The beams collide inside the four aforementioned
440 experiments. Each octant contains a curved and straight section. The LHC
441 magnets are built with NbTi superconductors cooled with super-fluid Helium to
442 2K, creating a 8.3T magnetic field to bend the proton beams.

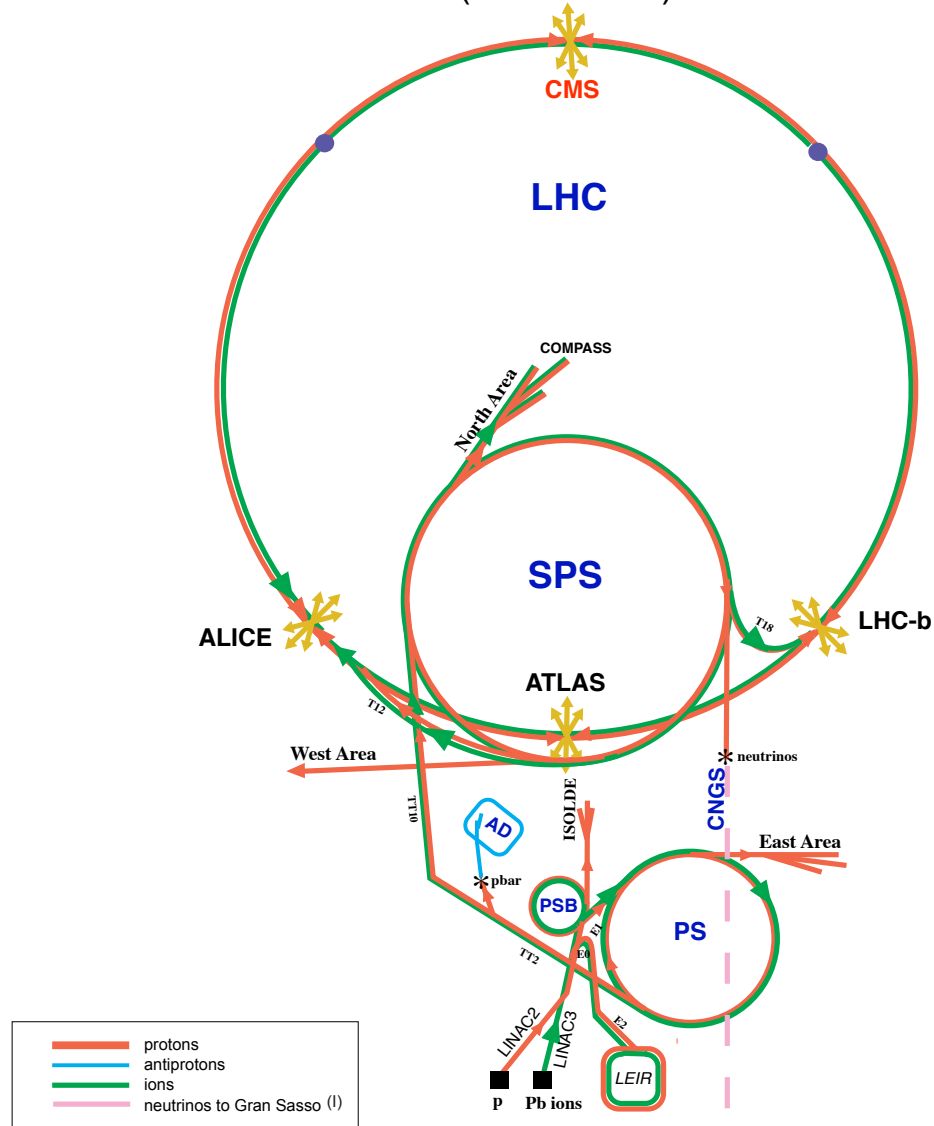


Figure 5.2: LHC Layout. Natasha write more

443 Four sequential particle accelerators are used to accelerate protons from rest
 444 as shown in Figure 5.3. First, Hydrogen gas is ionized to produce protons which
 445 are then accelerated to 50 MeV using Linac 2, a linear accelerator. The result-
 446 ing proton beam is then passed to three circular particle accelerators: Proton
 447 Synchrotron Booster, Proton Synchrotron, and Super Proton Synchrotron (SPS),

448 accelerating protons to 1.4, 25, and 450 GeV, respectively. Once the protons exit
449 the SPS, they are injected into the LHC at octant 2 and 8. Each proton bunch
450 contains $\sim 10^{11}$ protons. The spacing between bunches is 25 ns, which means
451 each beam contains 3564 bunches. However, some bunches are left empty due
452 to injection and safety requirements, yielding 2808 bunches per beam. Once the
453 proton beams are injected they are accelerated to 13 TeV.

CERN Accelerators (not to scale)



LHC: Large Hadron Collider

SPS: Super Proton Synchrotron

AD: Antiproton Decelerator

ISOLDE: Isotope Separator OnLine DEvice

PSB: Proton Synchrotron Booster

PS: Proton Synchrotron

LINAC: LINear ACcelerator

LEIR: Low Energy Ion Ring

CNGS: Cern Neutrinos to Gran Sasso

Rudolf LEY, PS Division, CERN, 02.09.96
Revised and adapted by Antonella Del Rosso, ETT Div.,
in collaboration with B. Desforges, SL Div., and
D. Manglunki, PS Div. CERN, 23.05.01

Figure 5.3: LHC Accelerator. Natasha write more

454 As many new physics models predict cross-sections below the weak scale it was
455 important to design the LHC to be capable of collecting enough data, by running
456 in high luminosity conditions. The machine luminosity depends only on beam
457 parameters:

$$L = \frac{N_p^2 f}{4\epsilon\beta^*} F \quad (5.1)$$

458 where N_p is the number of protons per bunch, f is the bunch crossing frequency,
459 ϵ is the transverse beam emittance, β^* is the amplitude function at the collision
460 point, and F is the geometric luminosity reduction factor due to the beams crossing
461 at an angle (rather than head-on).

462 **Chapter 6**

463 **The ATLAS Detector**

464 The ATLAS detector measures the position, momentum and energy of parti-
465 cles produced in the proton collisions by using magnetic fields, silicon detectors,
466 sampling calorimeters, and gaseous wire detectors. It is located approximately
467 100 m underground at Point-1 around the LHC beam line and weighs 7000 metric
468 tons. The detector is 46 m long, 25 m high, 25 m wide as shown in Figure 6.2.
469 The detector can be divided into three subsystems: the Inner Detector (ID), the
470 Calorimeters, and the Muon Spectrometer (MS). Figure 6.3 shows an overview of
471 how different particles interact in the detector.

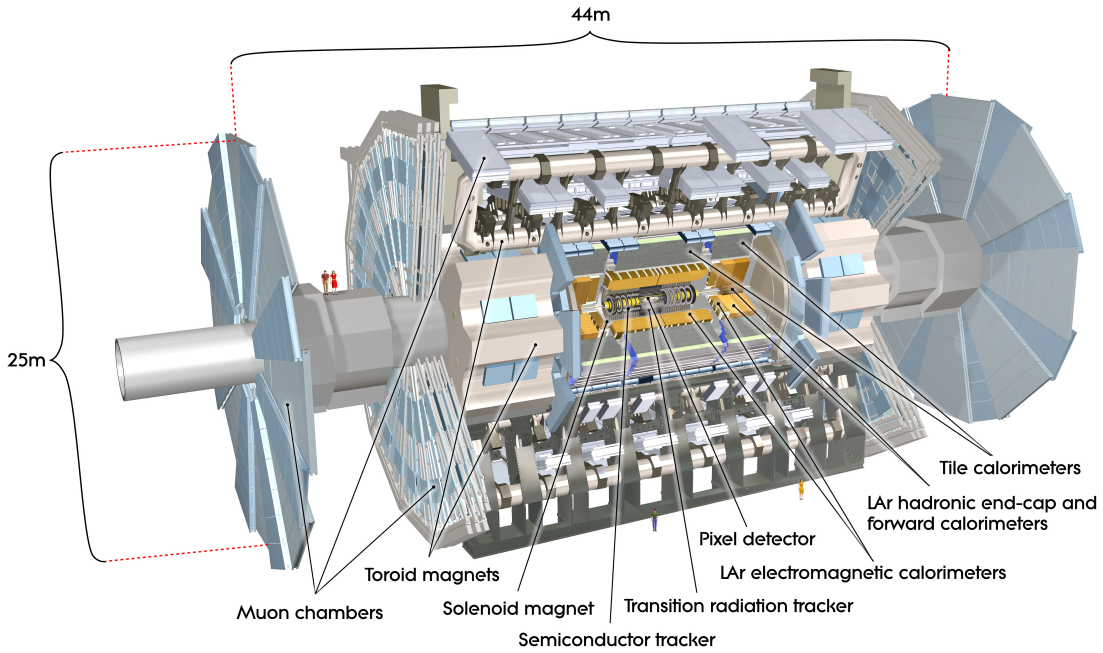


Figure 6.1: Big picture layout of ATLAS detector. Natasha: write more

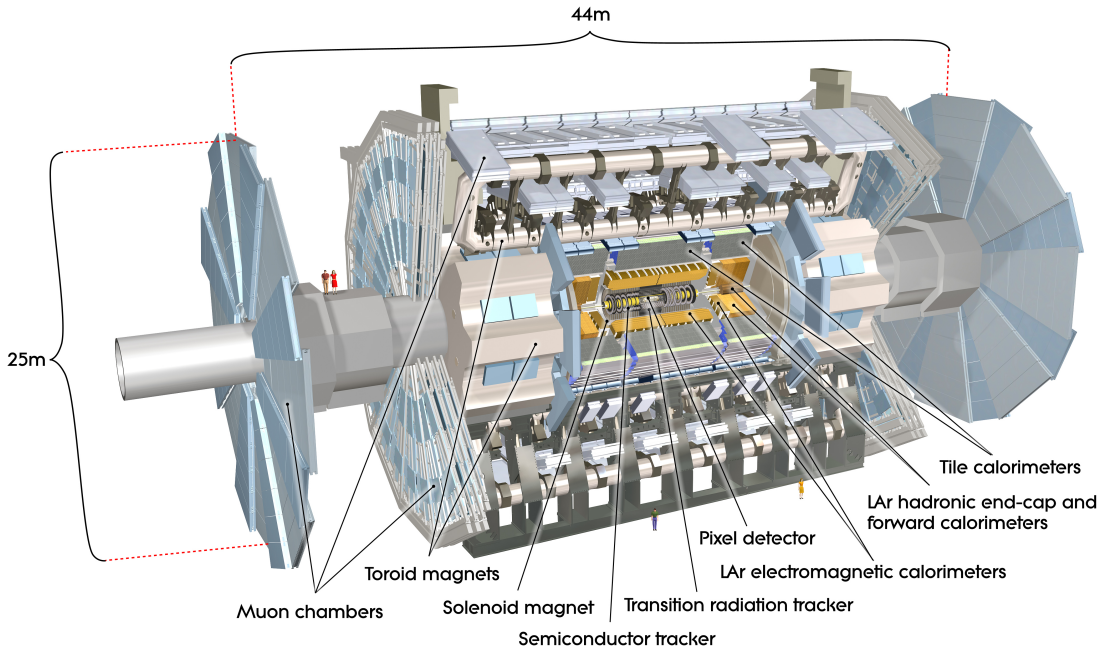


Figure 6.2: Big picture layout of ATLAS detector. Natasha: write more

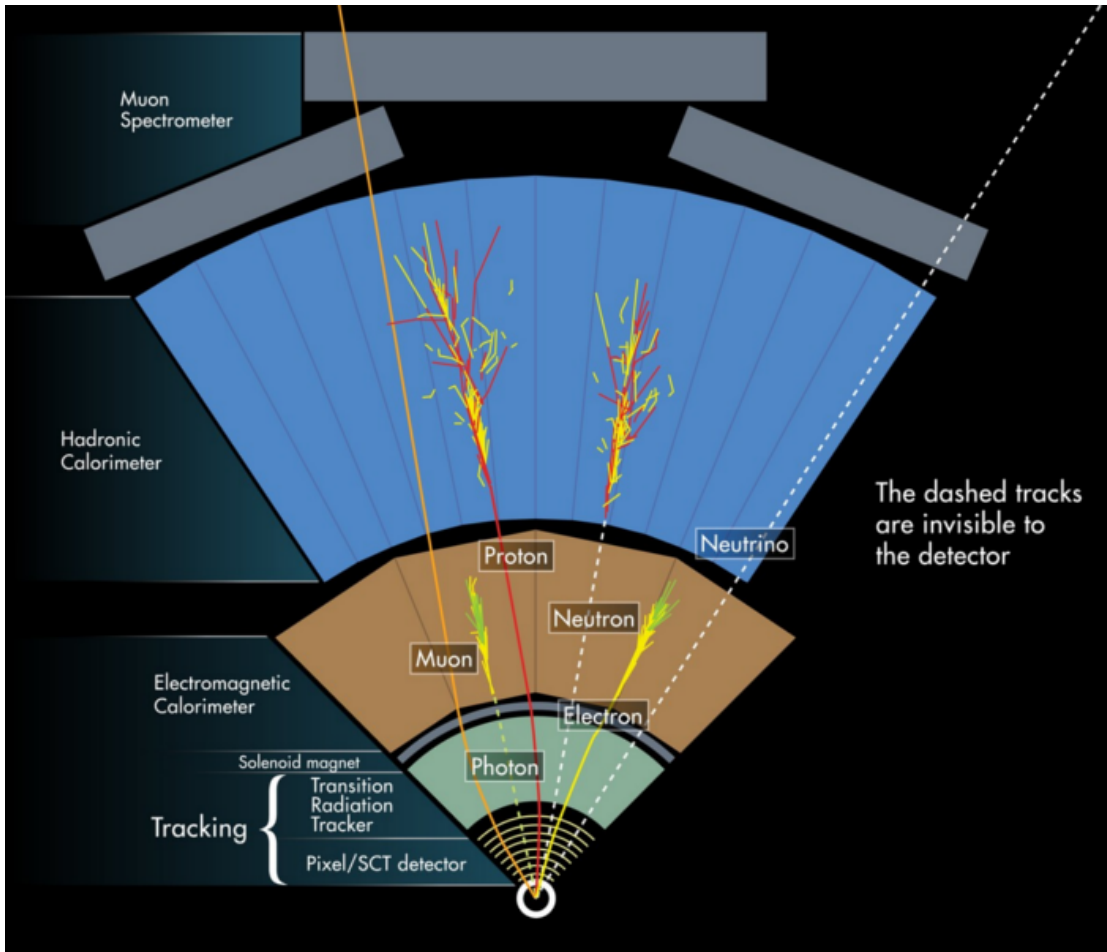


Figure 6.3: A simplified schematic of how different particles interact and are detected within ATLAS.

472 6.1 Coordinate System

473 The trajectory of particles within ATLAS is measured relative to the nominal
 474 interaction point. The z -axis points along the beam line, such that when the
 475 LHC is viewed from above, the counter-clockwise circulating beam points along
 476 the positive- z direction. The $x - y$ plane is transverse to the beam line, with the
 477 positive x -axis pointing towards the center of the LHC ring. The positive y -axis
 478 points vertically upward. The azimuthal angle, ϕ , is the angular distance about

479 the z -axis, with $\phi = 0$ along the x -axis. The polar angle from the z -axis is denoted
480 as θ . However, this quantity is not Lorentz invariant, like rapidity, $y = \frac{1}{2} \ln \frac{E+p_z}{E-p_z}$,
481 where E is the energy of the particle considered, and p_z , is it's momentum along
482 the z -axis. Pseudo-rapidity is preferred as $\Delta\eta$ is invariant under boosts along z
483 and particle production is approximately invariant under η . For massless particles,
484 rapidity and a related quantity, pseudorapidity, are the identical. The pseudora-
485 pidity is defined as: $\eta = -\ln \tan(\frac{\theta}{2})$. This quantity is preferred as it is purely a
486 geometric quantity, independent of particle energy. Angular separation between
487 particles in ATLAS are given by $\Delta R = \sqrt{\Delta\eta^2 + \Delta\phi^2}$. The distance from the
488 beamline is given by $r = \sqrt{x^2 + y^2}$

489 6.2 Inner Detector

490 The Inner Detector (ID) was designed to identify and reconstruct vertices,
491 distinguish pions from electrons, and measure the momentum of charged particles.
492 The ID uses three different technologies for particle reconstruction: the Pixel
493 Detector, Semiconductor Tracker (SCT), and the Transition Radiation Tracker
494 (TRT), shown in Figure 6.4 and 6.5. The entire ID is immersed in a 2T solenoidal
495 magnetic field parallel to the $+z$ -axis, causing charged particles to bend in the
496 transverse-plane, allowing particle momentum measurements.

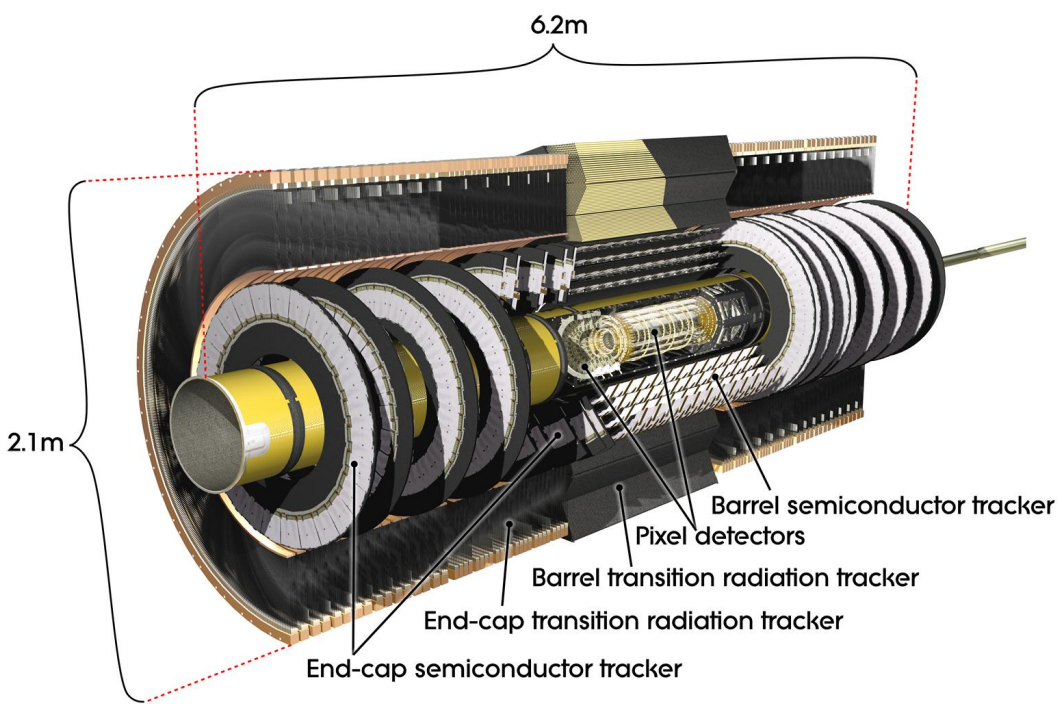


Figure 6.4: Layout of ATLAS Inner Detector

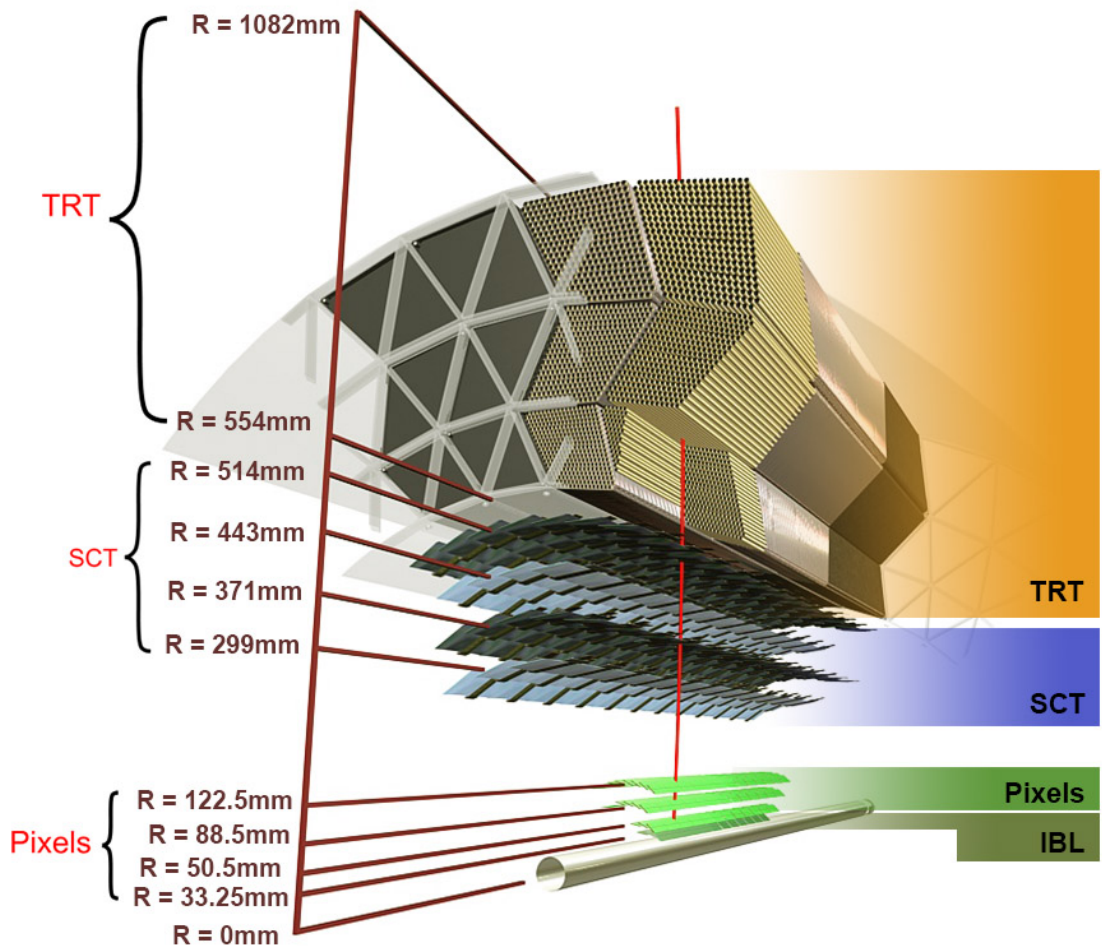


Figure 6.5: Layout of ATLAS ID Barrel System.

497 **6.2.1 Pixel Detector**

498 The pixel detector consists of four barrel layers between $r = 32.7$ and 122.5
499 mm, extending to $|z| = 400.5$ mm. The remaining detectors are arranged in bar-
500 rels and forward and backward rings. The innermost pixel barrel, the Insertable
501 b-Layer (IBL), only extends to $|z| = 332$ mm. The pixel detectors closer to the
502 beam line (larger η values) consists of six parallel cylindrical rings of pixel de-
503 tectors transverse to the beam line. The entire pixel detector consists of 1744
504 identical pixel sensors each with 46080 readout channels, totaling about 80 mil-
505 lion individual pixels. Most of the pixel sensors are $50 \times 400 \mu\text{m}^2$. Each pixel has
506 a position resolution of $14 \mu\text{m}$ in ϕ and $115 \mu\text{m}$ in the z direction.

507 **6.2.2 Semiconductor Tracker**

508 The SCT is located outside the pixel detector and has the same barrel and
509 endcap geometry as the pixel detector. SCT sensors are $80 \mu\text{m} \times 12$ cm with
510 a $80 \mu\text{m}$ strip pitch. In the barrel the strips are parallel to the z -axis and are
511 segmented in ϕ . In the endcaps, the strips extend radially. Sensors are grouped in
512 modules containing two layers of strips rotated 40 mrad with respect to each other.
513 This offset allows for the two-dimensional position of a track to be determined by
514 identifying the crossing point of the strips that registered a hit. SCT modules
515 measure tracks with an accuracy of $17 \mu\text{m}$ in $r - \phi$ and $580 \mu\text{m}$ in $z(r)$ in the
516 barrel (end-cap) region.

517 **6.2.3 Transition Radiation Tracker**

518 The transition radiation tracker (TRT), enveloping the SCT, is a gaseous
519 straw-tube tracker mainly used for electron/pion track separation. Each straw
520 is 4 mm in diameter and filled with a Xe- CO_2 - O_2 gas mixture. An anode wire at

521 the center of the straw is held at ground potential, while the walls of the straw
522 are kept at -1.4kV. When a charged particle passing through the TRT ionizes the
523 gaseous mixture, the resulting ions form an avalanche on the anode wire with a
524 gain of $\sim 10^4$. The signal from the anode wire is then digitized and discriminated.
525 Signals passing a low threshold cutoff are used to distinguish noise from tracks.
526 Signals passing a high threshold cutoff are sensitive to transition radiation (TR).
527 TR photons are emitted when charged particles pass between materials with dif-
528 ferent dielectric constants. The probability that a charged particle with energy E
529 and mass m passing between two materials emits a TR photon in the keV range
530 is proportional to $\gamma = E/m$. In the TRT straws these often then convert via the
531 photoelectric effect, causing a large avalanche triggering the high-threshold. Since
532 electrons have a smaller mass than pions, electron tracks are more likely to trig-
533 ger the high threshold. This then provides discrimination between electrons and
534 charged hadrons.

535 The barrel region of the TRT extends from $r = 563\text{-}1066$ mm and $|z| < 712$
536 mm. Barrel Straws are 144 cm long (divided $\sim \eta \approx 0$) and orientated parallel to
537 the beam direction. End-cap straws extend radially and are 37 cm long. There
538 are 53,544 straws in the barrel and 160,000 straws in the end-caps. Radiator mats
539 of polypropylene/polyethylene fibers in the barrel are aligned perpendicular to the
540 barrel straws (with holes for the straws to pass through). In the end-cap region,
541 radiator foils are layered between the radial TRT straws.

542 The arrival time of the signal pulse is sensitive to the distance between the
543 charged particle track and the anode wire and allows for a hit resolution of $130\mu\text{m}$.
544 The TRT extends to $|\eta| = 2.0$ and provides about 36 hits per track.

545 **6.3 Calorimeters**

546 The ATLAS electromagnetic and hadronic calorimeters (EMC and HCAL,
547 respectively) absorb and measure the energy of high energy hadrons, photons,
548 and electrons with $|\eta| < 4.9$. Both systems use sampling calorimeters which
549 consist of alternating layers of dense absorbing and active layers. In the absorbing
550 layer particles interact and lose energy, creating showers. These showers are then
551 detected and measured in the active layer. The amount of charge measured in the
552 active material scales with the energy of the incident particle, and thus provides a
553 measurement of the particle's energy. An overview of the layout of the calorimeter
554 system is shown in Figure 6.6.

555 The EMC measures and contains the energy of electromagnetically interacting
556 particles. It consists of layered accordion-shaped Lead absorber plates and elec-
557 trodes immersed in liquid Argon with 170k channels.. Using accordion-shaped
558 electrode and absorbers ensures ϕ symmetry and coverage. The EMC is com-
559 posed of a barrel part ($|\eta| < 1.475$), two end-caps ($1.375 < |\eta| < 3.2$), and a
560 presampler ($|\eta| < 1.8$). The presampler, containing only liquid Argon, corrects
561 for upstream energy losses of electrons and photons. The EMC barrel is segmented
562 into three layers. The first layer has finest segmentation with readout cells ex-
563 tending $\Delta\eta \times \Delta\phi = 0.025/8 \times 0.1$. This provides a precise shower measurements
564 used to separate prompt photons from $\pi^0 \rightarrow \gamma\gamma$ decays. The second layer has
565 coarser segmentation and is approximately 16 radiation lengths long. A radiation
566 length is the average distance an electron travels before losing all but $1/e$ of its
567 energy to bremsstrahlung. The last layer is the most coarse and measures the tail
568 of the electromagnetic shower. A schematic of the ECAL is shown in Figure 6.7.

569 The hadronic calorimeter located outside the EMC and is used to contain
570 and measure the energy of hadronically interacting particles. It consists of a tile

571 calorimeter (TileCal), hadronic end-cap calorimeter (HEC), and liquid Argon for-
 572 ward calorimeter (FCAL). TileCal is located behind the LAr EMC and uses steel
 573 absorbers and liquid Argon as the active material. TileCal consists of three barrel
 574 layers in the central and forward regions, extending up to $|\eta| < 1.7$. Photons
 575 generated from hadronic interactions are collected via wavelength-shifting fibers
 576 connected to photomultiplier tubes, as shown in Figure 6.8. The HEC lies behind
 577 the EMC endcap wheels. It uses copper absorbers and liquid Argon as the active
 578 material and covers $1.5 < |\eta| < 3.2$. Finally, the FCAL covers $3.1 < |\eta| < 4.9$
 579 and consists of three modules all using liquid Argon as the active material. The
 580 first module uses copper absorber and was designed for electromagnetic measure-
 581 ments. The second and third modules consist of tungsten absorber and are used
 582 to measure the kinematics of hadronically interacting particles. A schematic of
 583 the HCAL is shown in Figure 6.8.

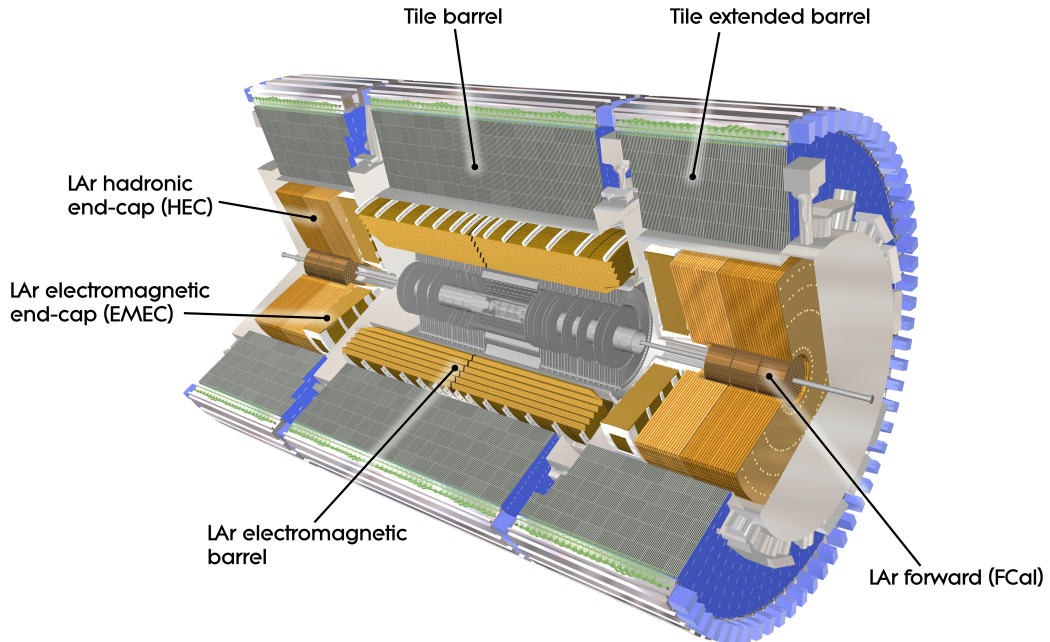


Figure 6.6: Overview of ATLAS electromagnetic and hadronic calorimeters.

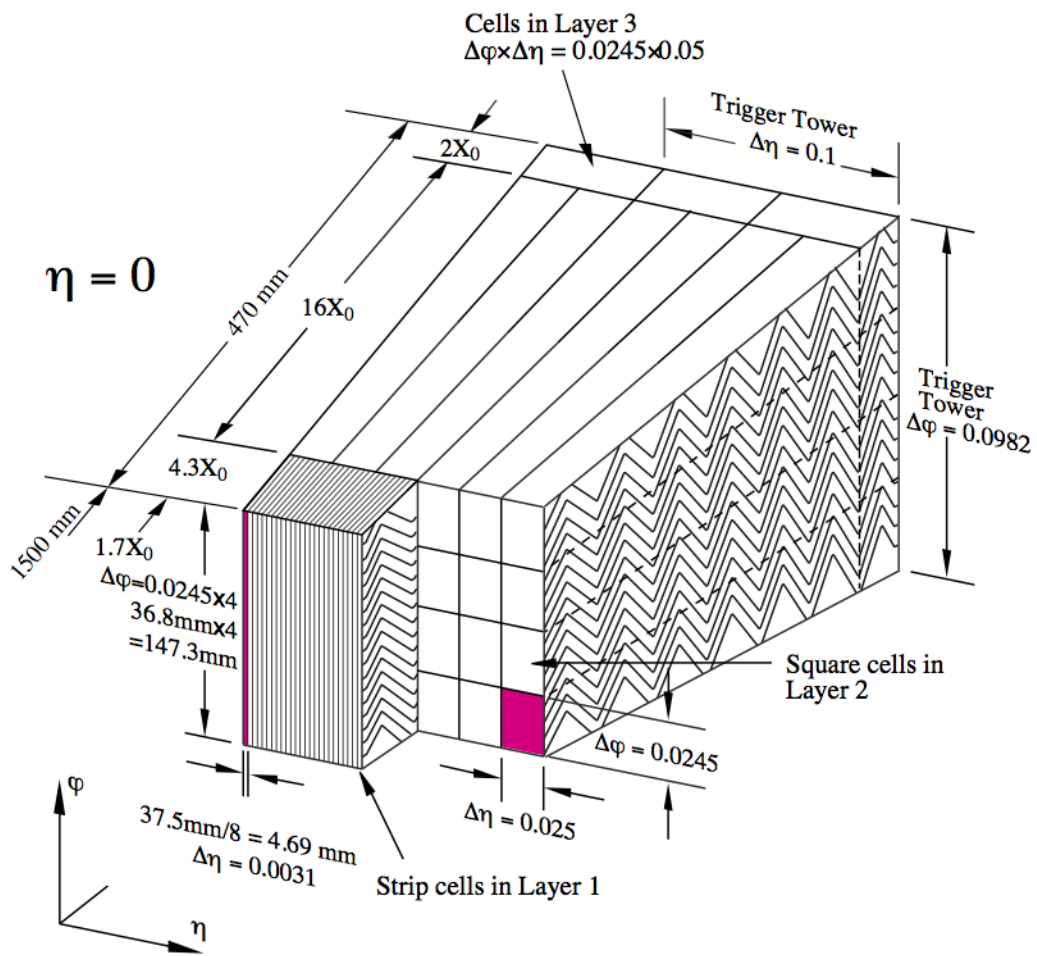


Figure 6.7: Schematic of ECAL.



Figure 6.8: Schematic of HCAL.

584 The energy resolution of the calorimeter subsystems are:

$$585 \quad \frac{\sigma_E}{E} = \frac{10\%}{\sqrt{E}} \oplus 0.7\% \text{ EMC}$$

$$586 \quad \frac{\sigma_E}{E} = \frac{50\%}{\sqrt{E}} \oplus 3\% \text{ hadronic barrel}$$

$$587 \quad \frac{\sigma_E}{E} = \frac{100\%}{\sqrt{E}} \oplus 10\% \text{ hadronic end-cap}$$

588 6.4 Muon Spectrometer

589 The muon spectrometer (MS) is the outermost detector system in ATLAS.

590 Muons with a $p_T > 4$ GeV are energetic enough to reach the MS. To measure the
591 momentum of these muons barrel and end-cap toroid magnets are used covering
592 $|\eta| < 1.4$ and $1.6 < |\eta| < 2.7$. For $1.4 < |\eta| < 1.6$, a combination of the barrel
593 and end-cap toroidal magnetic fields bend muon trajectories. The detector in the
594 barrel region form three concentric rings at $R = 5, 7.5, 10$ m and are segmented
595 in ϕ to accommodate the magnets. The end-cap region consists of three circular
596 planes perpendicular to z and located at $|z| = 7.4, 14, 21.5$ m from the interaction
597 region. An additional detector at $|z| = 10.8$ m covers the transition region between
598 the barrel and end-cap.

599 The MS readout consists of four subsystems: Monitored Drift Tubes (MDT),
600 Cathode Strip Chambers (CSC), Resistive Plate Chambers (RPC), and Thin Gap
601 Chambers (TGC). The first two subsystems are used primarily for measuring
602 muon track parameters, while the RPC and TGC subsystems are used for muon
603 triggering. A schematic of this system is shown in Figure 6.9.

604 The MDT subsystem consists of precision tracking chambers for $|\eta| < 2.7$,
605 except for the inner most end-cap layer ($2.0 < |\eta| < 2.7$), where CSCs are used.
606 The basic unit of MDT chambers are thin walled Aluminum tubes with a diameter
607 of 3 cm and length of 0.9-6.2 m. These tubes are filled with a mixture of Ar-CO₂
608 gas with a 50μm W-Rn wire running down the center of the tube, which is kept at

609 3080 V. Since the maximum drift time of these chambers is ~ 700 ns, they are not
610 used for triggering. MDT chambers consist of 3-4 layers of tubes mounted on a
611 rectangular support system, as seen in Figure 6.10, orientated along ϕ to measure
612 the coordinate in the bending plane of the magnetic field with a resolution of 35
613 μm .

614 The MDT subsystem can only handle hit rates below $150\text{Hz}/\text{cm}^2$. For this
615 reason, CSCs are used in the innermost end-cap layer where hit rates are larger.
616 CSCs can handle hit rates up to $1000\text{Hz}/\text{cm}^2$. CSC are multiwire proportional
617 chambers. These chambers are filled with a Ar- CO_2 gas mixture and evenly spaced
618 wires kept at 1900 V. These wires are orientated in the radial direction but not
619 read out. Instead on one side of the cathode are copper strips parallel to the wires,
620 measuring η , while on the other side of the cathode are strips parallel to the wires
621 measuring ϕ . The width between strips is approximately 1.5 mm providing a
622 resolution of 60 μm in the bending-plane and 5 mm in the non-bending plane.

623 Since the CSC and MDT systems do not have prompt timing signals, the RPC
624 and TGC systems are used for triggering. The RPC system is used in the barrel
625 region ($|\eta| < 1.05$). RPC consist of two parallel resistive plates separated by a 2
626 mm insulated spacer with 100 mm spacing kept at 9.8 kV, as shown in Figure 6.11.
627 A gaseous mixture of $\text{C}_2\text{H}_2\text{F}_4$, C_4H_{10} , and SF_6 fills the space between the two
628 plates. Metallic strips on the outer faces of the plates are used to read out signals
629 produced by the gas ionizing. The middle barrel layer consists of two layers of
630 RPCs on either side of the MDT layer and one layer on the outermost MDT
631 layer. Each layer contains two orthogonal sets of metallic strips providing η and
632 ϕ measurements. The timing resolution of RPCs is 1.5 ns, and therefore may be
633 used to identify bunch crossings.

634 Finally, the TGCs are used in the end-cap regions and are primarily used to

635 provide L1 trigger decisions and ϕ measurements. TGCs are multi-wire propor-
 636 tional chambers consisting of arrays of gold-coated tungsten wires placed between
 637 two cathode planes. These wires are separated by 1.8 mm and cathodes are 1.4 mm
 638 from the wires. Orthogonal to the wires, on the opposite side of the cathode plane
 639 are copper strips held at 2900 V. The chambers are filled with a mixture of CO_2
 640 and n-pentane gas, the latter acts as a quenching gas to prevent avalanches initi-
 641 ated by secondary γ -rays from the primary avalanche. Figure 6.12 is a schematic
 642 of a TGC. The timing resolution of TGCs is less than 25 ns and therefore they
 643 are used for bunch crossing measurements.

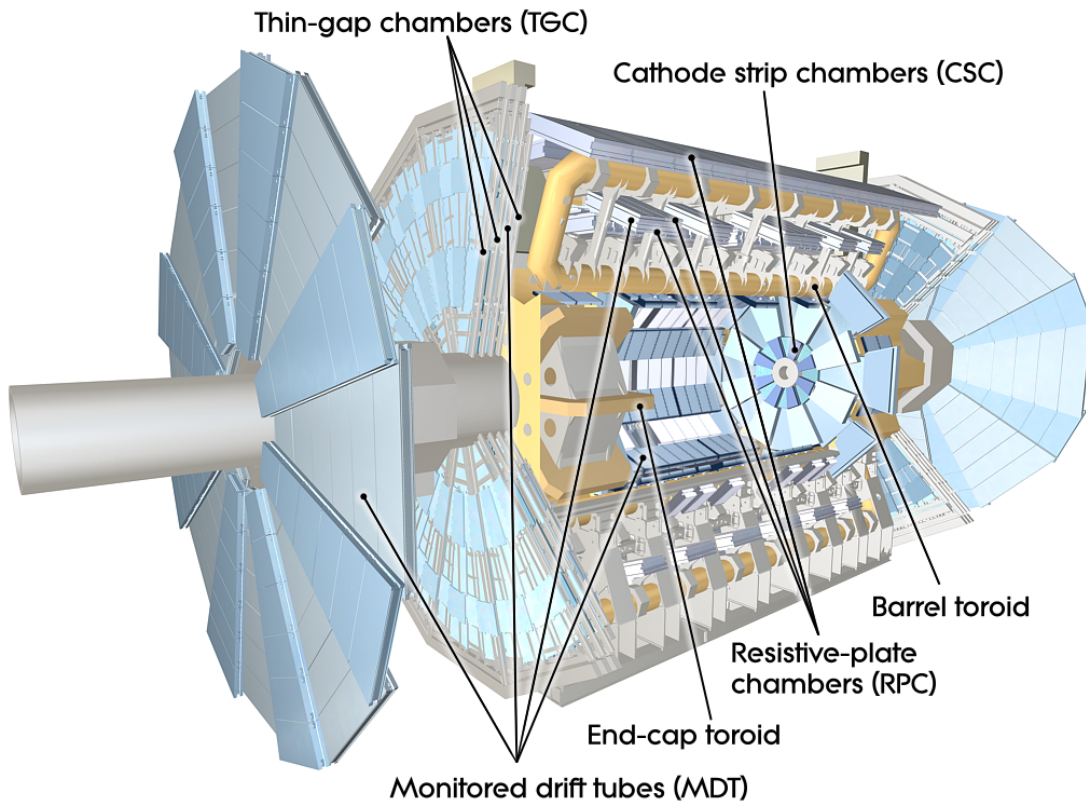


Figure 6.9: Schematic of Muon Spectrometer [cite G35]

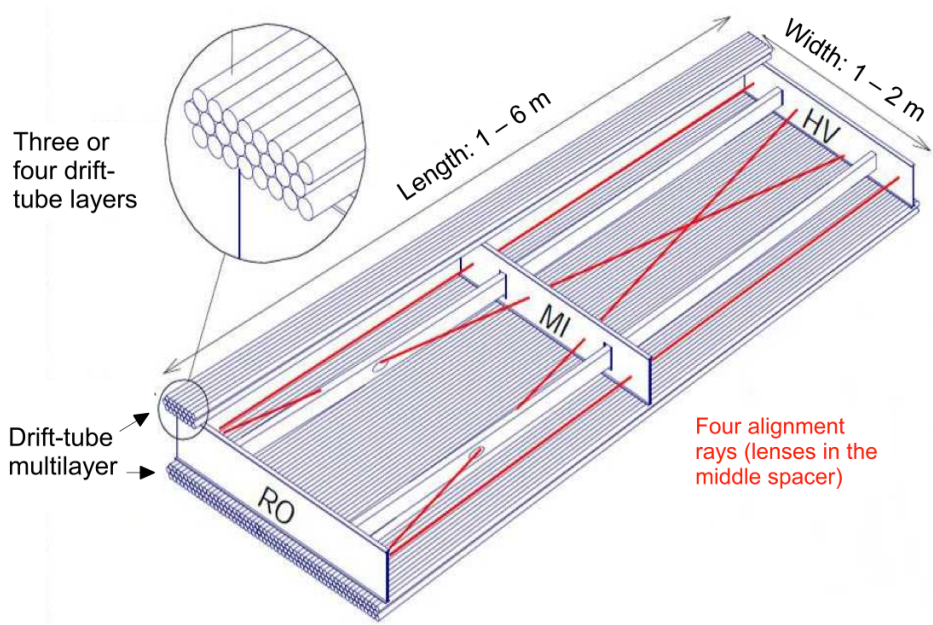


Figure 6.10: Schematic of MDT chamber. [cite G35]

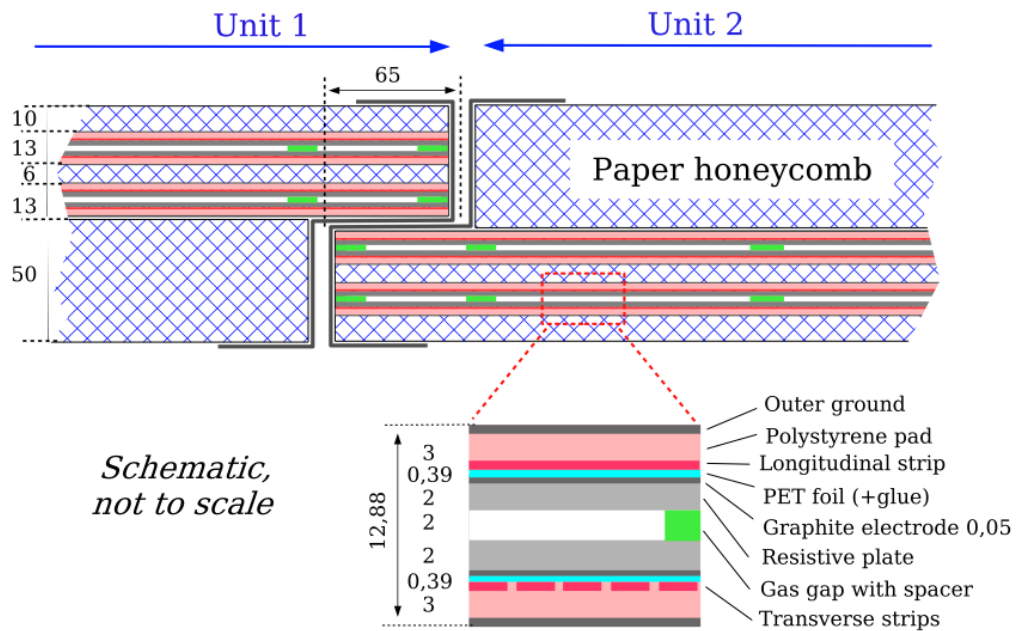


Figure 6.11: Schematic of RPC chamber, which is used for triggering in the central region of the detector [cite G35].

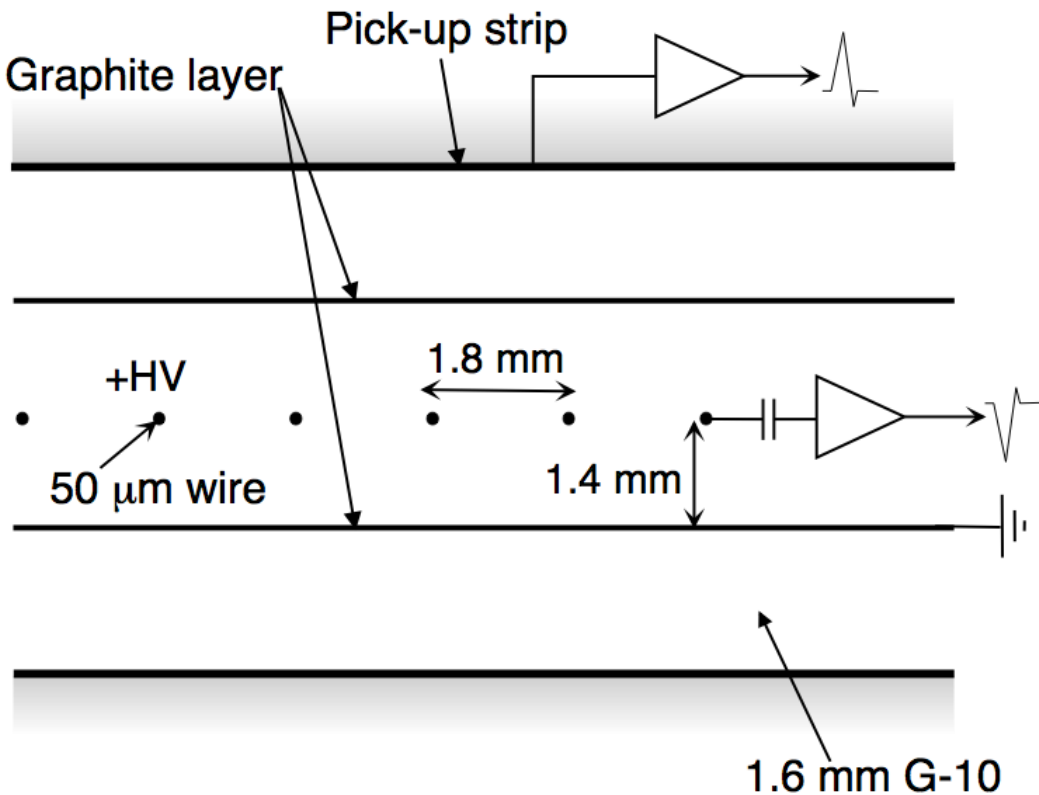


Figure 6.12: Schematic of TGC chamber, which is used for triggering in the muon end-cap region. [cite G35]

6.5 Magnet System

A particles with charge, q , and velocity v , moving in magnetic field, B , experiences a force, $F = qv \times B$. This force can cause charged particles to have a curved trajectory in magnetic fields, which the ID and MS use to determine the particles p_T . The central solenoid provides the magnetic field for the ID and the toroidal magnets provide the magnetic field for the MS.

The layout of the magnet system is shown in Figure 6.13. The central solenoid consists of a single-layer Al-stabilized NbTi conductor coil wound inside an Al

652 support cylinder. The solenoid is 5.8 m long, 50 cm thick and has an inner radius
653 of 1.23 m. It is cooled to 4.5 K to reach superconducting temperatures and shares
654 the liquid argon calorimeter vacuum vessel to minimize material in the detector.
655 A current of 7.730kA produces a 1.998 T solenoidal magnetic field, pointing in
656 the $+z$ direction.

657 The toroidal magnet system consists of a barrel and two end-cap toroidal
658 magnets used to create a magnetic field outside the calorimeters that is orientated
659 along ϕ . Each barrel toroid is 25.3 m long with an inner and outer diameter of 9.4
660 and 20.1 m and weighs 830 tonnes. Endcap toroids are 5 m long with an inner and
661 outer radius of 1.65 and 10.7 m. Both toroid systems use Al-stabilized Nb/Ti/Cu
662 conductors. The magnetic field strength in the barrel and endcap regions are 0.5
663 and 1 T, respectively.

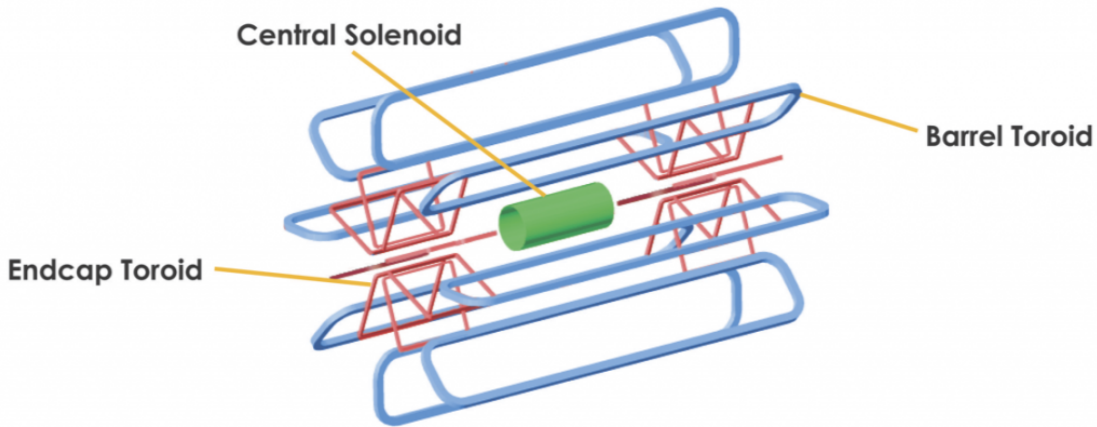


Figure 6.13: Layout of ATLAS magnet systems.

664 **6.6 Trigger System**

665 Since collisions occur every 25 ns and reading out all detector channels and
666 storing that information is not currently feasible (would require saving 60 million
667 megabytes per second), the majority of events are not kept for analysis. ATLAS

668 uses a multi-stage trigger system to select approximately 1,000 of the 1.7 billion
669 collisions that occur each second (corresponding to a rate of 1 kHz from the 40
670 MHz proton collision rate). The first stage of the trigger system is the hardware
671 level (L1) trigger. This trigger reduces the event rate to \sim 100 kHz by identifying
672 Regions-of-Interest (ROIs) containing high p_T leptons, photons, jets, or E_T^{miss} by
673 using information from RPCs, TGCs, and calorimeters to make a 2.5 μ s decision.
674 This information is then passed to a high-level trigger (HLT) which further de-
675 creases event rates to \sim 1 kHz. The HLT uses finer granularity measurements
676 from the MS and ID to perform simplified offline reconstruction to decide which
677 events to keep.

Part IV

678

Method

679

680 **Chapter 7**

681 **Dataset and Simulated Samples**

682 **7.1 Dataset**

683 This analysis uses pp collision data collected from 2015 to 2018 at $\sqrt{s} = 13$
684 TeV, corresponding to 139/fb of data as shown in Figure 7.1 and 7.2. From this
685 dataset, only those events in which the tracker, calorimeters, and muon spectrom-
686 eter have good data quality are used. For a given event, the solenoid and toroidal
687 magnets must also be operating at their nominal field strengths. In addition to
688 this, events must pass further quality checks to reject events where detector sub-
689 systems may have failed. These selections reject events that containing LAr noise
690 bursts, saturation in the electromagnetic calorimeter, TileCal errors, and failures
691 in event recovery due to tracker failures. Events with information missing from
692 subsystems (usually due to busy detector conditions) are rejected. Events must
693 also contain a primary vertex with at least two associated tracks, where the pri-
694 mary vertex is selected as the vertex with the largest $\sum p_T^2$ over tracks associated
695 with the vertex and $p_T > 0.5$ GeV.

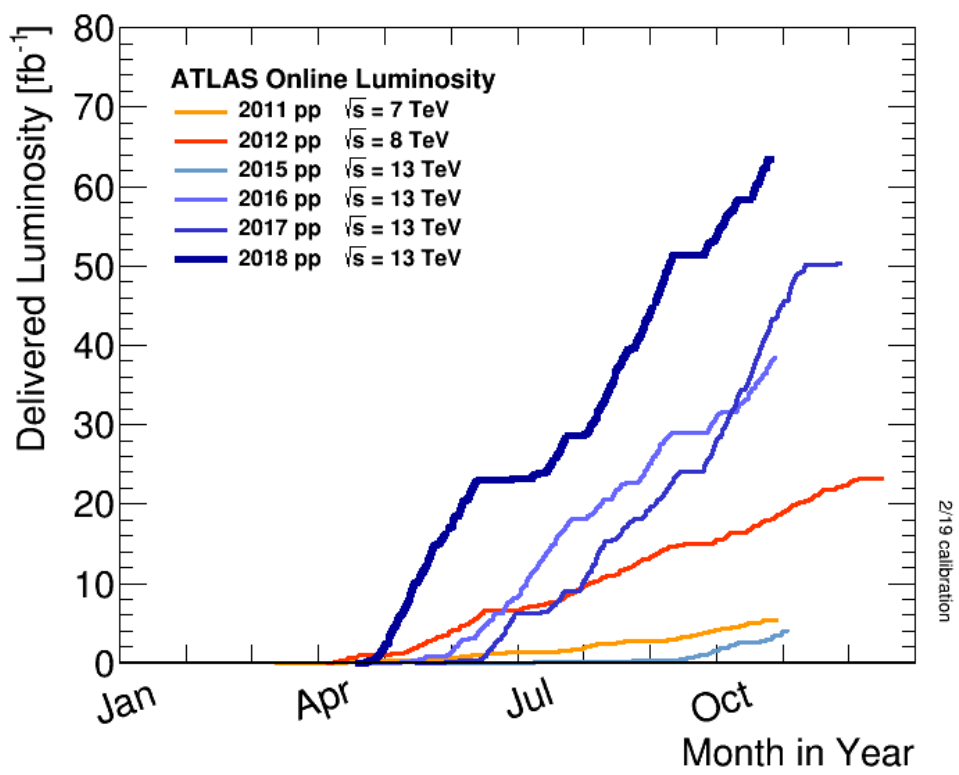


Figure 7.1: Integrated luminosity for data collected from ATLAS from 2011 - 2018



Figure 7.2: Mean number of interactions per crossing for data collected from ATLAS from 2011 - 2018

696 7.2 Simulated Samples

697 Samples are simulated in order to model backgrounds, evaluate signal ac-
698 ceptance, optimize event selection and estimate systematic and statistical uncer-
699 tainties. The dominant backgrounds for this analysis are $W/Z + \text{jets}$, diboson
700 (WZ/WW), $t\bar{t}$, single top and multijet production.

701 $W/Z+\text{jet}$ events are simulated using Sherpa 2.2.1 at NLO [cite [29]] and merged
702 with the Sherpa parton shower using the ME+PS@NLO prescription [13]. These
703 events are then normalized to NNLO cross sections. The $t\bar{t}$ and single-top back-
704 grounds are generated with Powheg-Box with NNPDF3.0NLO PDF sets in the
705 matrix element calculation [cite[35]]. For all processes, the parton shower, frag-
706 mentation, and underlying event are simulated using Pythia 8.320 with the A14
707 tune set[cite[ATL-PHYS-PUB-2014-02]]. Diboson processes are generated using
708 Sherpa 2.2.1.

709 Signal samples are simulated using MadGraph 5-2.2.2 [cite 42] and Pythia
710 8.186 with NNPDF230LO. RS Graviton samples are generated with $k/M_{PL}=1$.
711 HVT Model A (B) samples are simulated with $g_V = 1(3)$, as the difference in the
712 width of the samples is smaller than detector resolution. Model C is generated by
713 setting $g_H = 1$ and $g_f = 0$ to model VBF production of HVT bosons. Signals are
714 generated for masses between 300 GeV and 5 TeV.

715 **Chapter 8**

716 **Objects**

717 **8.1 Electrons**

718 Electrons are reconstructed from electromagnetic showers in the LAr EM
719 calorimeter. During reconstruction cells of $\Delta\eta \times \Delta\phi = 0.025 \times 0.025$ are grouped
720 into 3×5 clusters. These clusters are then scanned for local maxima that seed
721 electron clusters. These clusters must then be matched to ID track from the PV.
722 This requirement minimizes non-prompt electron and fake electron backgrounds.
723 Electrons must pass identification and isolation requirements. Electron identifica-
724 tion (loose, medium, tight) classification is based on a multivariate discriminant
725 that identifies electrons using a likelihood based method. For this analysis, events
726 are required to have one tight electron and no additional loose electrons. Elec-
727 trons are also required to be isolated. The electrons are considered isolated if the
728 quotient of the sum of the transverse momentum (of calorimeter energy deposits)
729 in a cone around the electron of size $\Delta R = 0.2$ and the transverse momentum
730 of the electron to be less than $0.015 * p_T$ or 3.5 GeV, whichever is smaller. This
731 requirement rejects non-prompt photons and other fake leptons. Electrons in this
732 analysis are also required to have $p_T > 30$ GeV and $|\eta| < 2.47$. Electrons are also

733 required to have $p_T > 30$ GeV.

734 Electrons are calibrated to determine data-driven scale factors using $J/\Psi \rightarrow$
735 ee , $Z \rightarrow ee$, $Z \rightarrow \ell\ell\gamma$ processes. These corrections account for the non-uniform
736 response of the detector which introduces modeling and reconstruction uncertain-
737 ties.

738 8.2 Muons

739 As muons traverse the entire detector, they are reconstructed from ID and
740 MS tracks. For this analysis the muon identification and isolation working points
741 are chosen to minimize the contributions from non-prompt muons. Towards this
742 end, each selected event must contain exactly one muon that passes the medium
743 identification working point, and no additional muons (that pass the loose working
744 point). For the medium working point, two types of reconstructed muons are
745 used: combined and extrapolated muons (CB and ME, respectively). For CB
746 muons, ID and MS tracks are reconstructed independently and a combined track
747 fit is performed by adding or removing MS tracks to improve the fit quality.
748 ME muons are reconstructed from only MS tracks with hits in at least two layers,
749 which ensures the track originates from the PV. ME muons extend the acceptance
750 for muon reconstruction outside the ID from $2.5 < |\eta| < 2.7$. The medium
751 identification working point uses CB and ME tracks. CB tracks must have at
752 least 3 hits in two MDT layers. ME tracks are required to have at least three
753 MDT/CSC hits. To further minimize contributions from fake muons, the selected
754 muons are required to be isolated from other tracks, as muons from W, Z decays are
755 often isolated from other particles. To insure the selected muons are isolated, the
756 scalar sum of the transverse momentum of tracks in a cone of $\Delta R = 0.3$ compared
757 to the transverse momentum of the muon must be less than 0.06. Muons are also

758 required to have $p_T > 30$ GeV.

759 Muons are calibrated using well-studied resonances $J/\Psi \rightarrow \mu\mu$ (low- p_T), $Z \rightarrow$
760 $\mu\mu$ (high- p_T). Figure 8.1 shows the combined muon p_T uncertainty from this
761 calibration. The total systematic uncertainty is less than 1% for all p_T ranges
762 considered in this analysis.

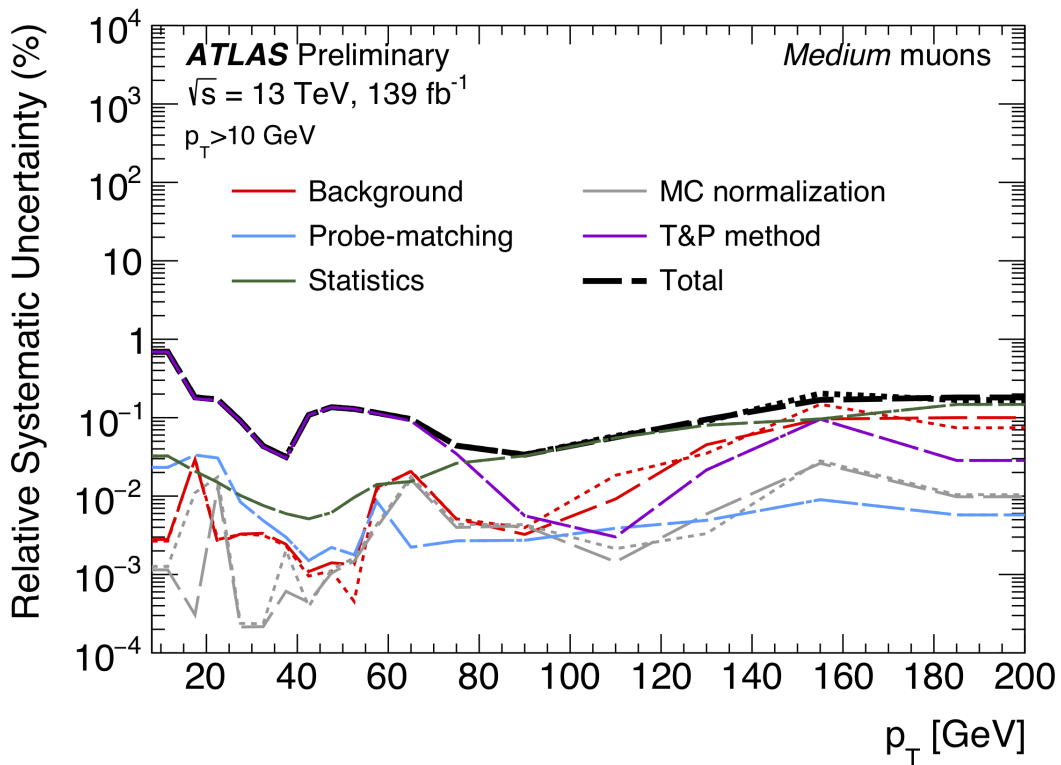


Figure 8.1: This figure shows the breakdown of the muon reconstruction efficiency scale factor measured in $Z \rightarrow \mu\mu$ as a function of p_T [5].

763 8.3 Jets

764 Three types of jets are used in this analysis: variable radius, small-R and
765 large-R jets. Variable radius jets are used to reconstruct Z bosons decaying to
766 two b -jets in the jet catchment area of large-R jet in the Merged regime. Small-R

767 jets are used to reconstruct the hadronically decaying W/Z candidates in the
768 resolved analysis and the forward jets from resonances produced through vector
769 boson fusion. Large-R jets are used to reconstruct the hadronically decaying boson
770 in the merged regime.

771 For all of these jet collections, the jet energy is calibrated sequentially as shown
772 in Figure 8.2. After the jet direction is corrected to point to the PV, the energy
773 of the jet is corrected. First, the jet energy is corrected to account for pileup
774 contributions based on the p_T and area of the jet (these corrections are extracted
775 from a $pp \rightarrow jj$ sample). Following this, another pileup correction is applied that
776 scales with μ and N_{PV} .

777 MC-based corrections are then applied that are meant to transform the jet
778 energy and η back to truth level. Therefore, these corrections account for the
779 non-compensating nature of the ATLAS calorimeters and inhomogeneity of the
780 detector. Following this, the Global Sequential Calibration is applied that re-
781 duces flavor dependence of jet calibrations and accounts for energy leakage of jets
782 outside the calorimeters. Finally, in-situ corrections are applied that account for
783 differences in jet responses between data and simulation ($\gamma/Z + \text{jet}$ and fake lep-
784 ton samples are used). These differences can be due to mismodelling of the hard
785 scatter event, pile-up, jet formation, etc.

786 To further reject fake jets, jets must pass quality requirements based on the
787 following variables ([cite P42]):

- 788 - f_Q^{LAr} : fraction of energy of jet's LAr cells with poor signal shape
- 789 - f_Q^{HEC} : fraction of energy of jet's HEC cells with poor signal shape
- 790 - E_{neg} : sum of cells with negative energy
- 791 - f_{EM} : fraction of jet's energy deposited in EM calorimeter

- 792 - f_{HEC} : fraction of jet's energy deposited in HEC calorimeter
- 793 - f_{max} : maximum energy fraction in any single calorimeter layer
- 794 - f_{ch} : ratio of the scalar sum of the p_T of a jet's charged tracks to the jet's p_T
- 795 Jets selected for the resolved analysis must pass one of the following criteria:
- 796 - $f_{HEC} > 0.5$ and $|f_Q^{HEC}| > 0.5$ and $\langle Q \rangle > 0.8$
- 797 - $|E_{neg}| > 60$ GeV
- 798 - $f_{EM} > 0.95$ and $f_Q^{LAr} > 0.8$ and $\langle Q \rangle > 0.8$ and $|\eta| < 2.8$
- 799 - $f_{max} > 0.99$ and $|\eta| < 2$
- 800 - $f_{EM} < 0.05$ and $f_{ch} < 0.05$ and $|\eta| < 2$
- 801 - $f_{EM} < 0.05$ and $|\eta| > 2$

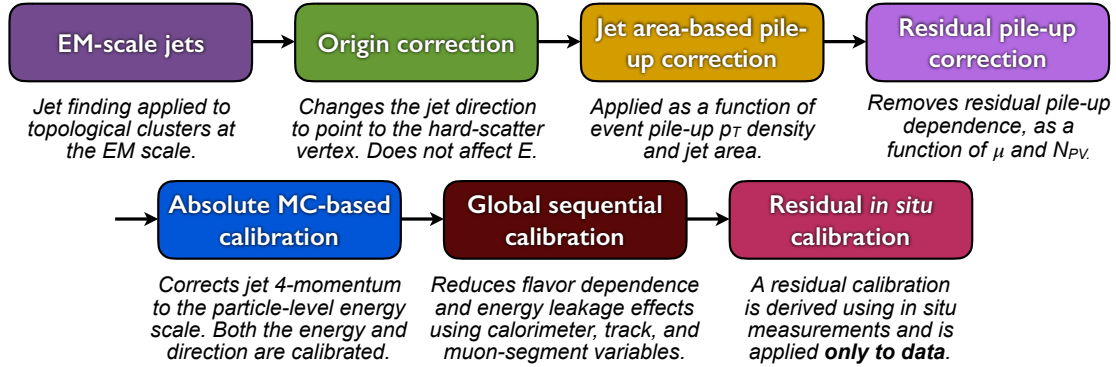


Figure 8.2: [8] This diagram shows the calibration stages for EM jets.

802 **8.3.1 Small-R jets**

803 Small-R jets are used to reconstruct the hadronically decaying W/Z candi-
804 date when the two resulting jets are well-separated in $\eta\text{-}\phi$ space. Small-R jets
805 are also used to identify forward jets from resonances produced through vector
806 boson fusion. Small-R jets are constructed from topologically connected clusters
807 of calorimeter cells (topoclusters), seeded from calorimeter cells with energy de-
808 posits significantly above the noise threshold. These cells are then used as inputs
809 to the $\text{anti}-k_t$ algorithm [16] with a radius parameter, $R = 0.4$.

810 Jets used in this analysis must have $p_T > 30$ GeV and $|\eta| < 2.5$. To further
811 reduce fake jets the jet-vertex-tagger (JVT) is used to reject pile-up jets [7]. The
812 JVT uses two track-based variables, corrJVF and R_{p_T} to calculate the likelihood
813 that the jet originated from the PV. The corrJVF compares the scalar sum of the
814 p_T of tracks associated with the jet and PV to the scalar sum of the p_T of tracks
815 associated with the jet. This variable also includes a correction that reduces the
816 dependency of corrJVF with the number of reconstructed vertices in the event.
817 The other discriminant, R_{p_T} , is given by the ratio of the scalar sum of the p_T of
818 tracks associated with the jet and PV to the p_T of the jet. Both of these variables
819 peak around zero for pileup jets, as these jets are unlikely to have tracks associated
820 with the PV. JVT cuts are applied to all jets with $p_T > 120$ GeV. Central jets
821 ($|\eta| < 2.4$) are required to have a $\text{JVT} > 0.59$ and forward jets ($2.4 < |\eta| < 2.5$)
822 are required to have $\text{JVT} > 0.11$.

823 **8.3.2 Large-R jets**

824 Large-R ($R = 1.0$) jets are used to reconstruct the hadronically decaying W/Z
825 candidate when the resulting jets are not well-separated in $\eta\text{-}\phi$ space, and overlap
826 forming one large-R jet. Track-Calorimeter Clusters (TCCs) are used to reconstruct these

jets [cite ANA 50]. These jets are constructed using a pseudo particle flow method
 using ID tracks matched to calorimeter clusters. To remove contamination in the
 jet from pileup and the underlying event, jets are trimmed using a re-clustering
 algorithm. This algorithm removes subjets with $p_T^{subjett} < 0.1 p_T^{jet}$.

The angular resolution of the calorimeter degrades sharply with jet p_T , but the
 jet energy resolution improves. The tracker has excellent angular resolution which
 improves with p_T . Therefore, by matching tracks to jets, TCCs have more precise
 energy and angular resolution than jets constructed from calorimeter information
 only. These jets are required to have $p_T > 200$ GeV, $|\eta| < 2.0$ and $m_J > 50$ GeV.

TCC jets are trimmed as detailed in [cite ANA 45], which suppresses pileup
 and soft radiation in the jet, the jet mass is calculated as the four-vector sum
 of the jet's constituents (assuming massless constituents). The jet mass peaks
 around the W/Z boson mass for $W/Z \rightarrow qq$ jets, and more broadly for quark and
 gluon induced jets.

These jets are then tagged as W jet if it passes optimized jet mass and sub-
 structure (D_2) cuts for W bosons, and a Z jet if it passes the cuts for the Z
 boson. The jet substructure variable D_2 is given by the ratio of energy correlation
 functions. These functions are derived from the energies and pair-wise angles of
 a jet's constituents [cite ANA 46, 47]:

$$D_2^{\beta=1} = E_{CF3} \left(\frac{E_{CF1}}{E_{CF2}} \right)^3 \quad (8.1)$$

where the energy correlation functions are defined as:

$$E_{CF1} = \sum_i p_{T,i} \quad (8.2)$$

$$E_{CF2} = \sum_{ij} p_{T,i} p_{T,j} \Delta R_{ij} \quad (8.3)$$

$$E_{CF3} = \sum_{ijk} p_{T,i} p_{T,j} p_{T,k} \Delta R_{ij} \Delta R_{jk} \Delta R_{ki} \quad (8.4)$$

848 A two-dimensional optimization of the jet mass and D_2 thresholds was per-
 849 formed to provide maximum sensitivity for this analysis. This optimization was
 850 done by maximizing the signal sensitivity (using HVT W' and G_{KK} samples)
 851 against the single quark and gluon jet backgrounds in jet p_T bins. Figure 8.3
 852 shows the optimized thresholds on D_2 and jet mass as a function of jet p_T . Figure
 853 8.4 shows the efficiency of the optimized W/Z taggers as a function of jet p_T .

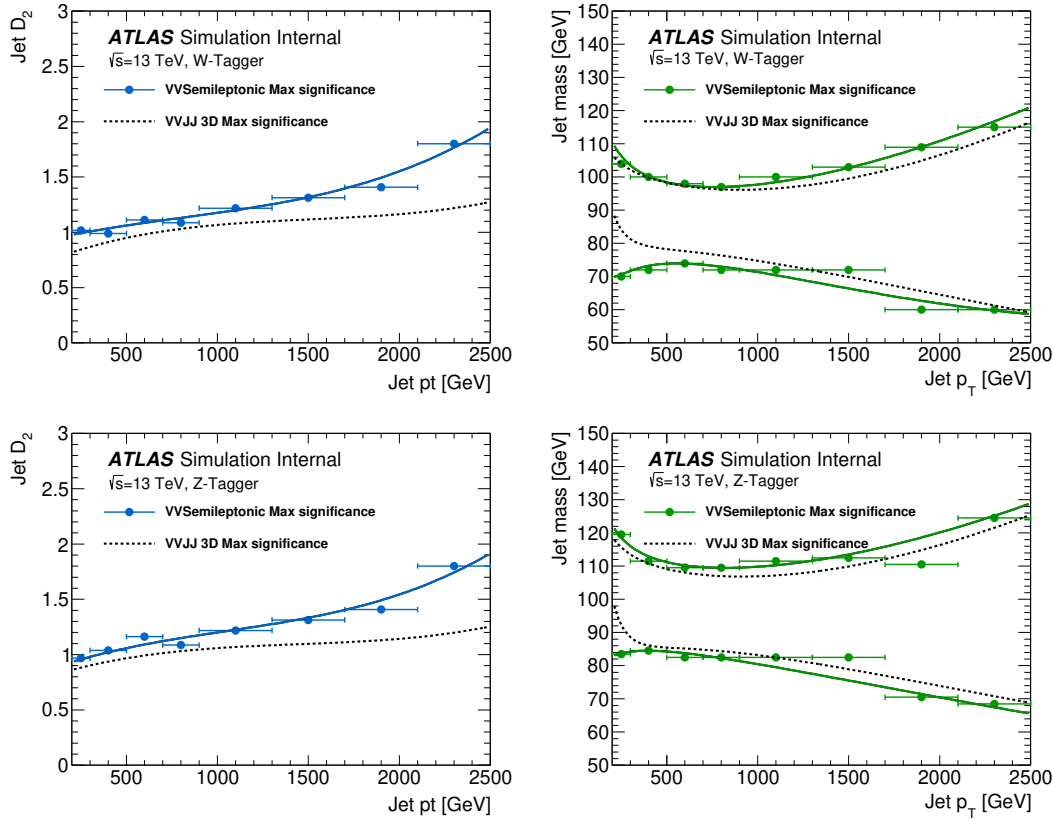


Figure 8.3: The upper cut on D_2 (a) and jet mass window cut i.e. the upper and lower boundary of the mass (b) of the W -tagger as a function of jet p_T . Corresponding values for Z -tagger are shown in (c) and (d). The optimal cut values for maximum significance are shown as solid markers and the fitted function as solid lines. Working points from $VV \rightarrow JJ$ [ATLAS-HDBS-2018-31-002] is also shown as dashed lines as a reference. Natasha reword?

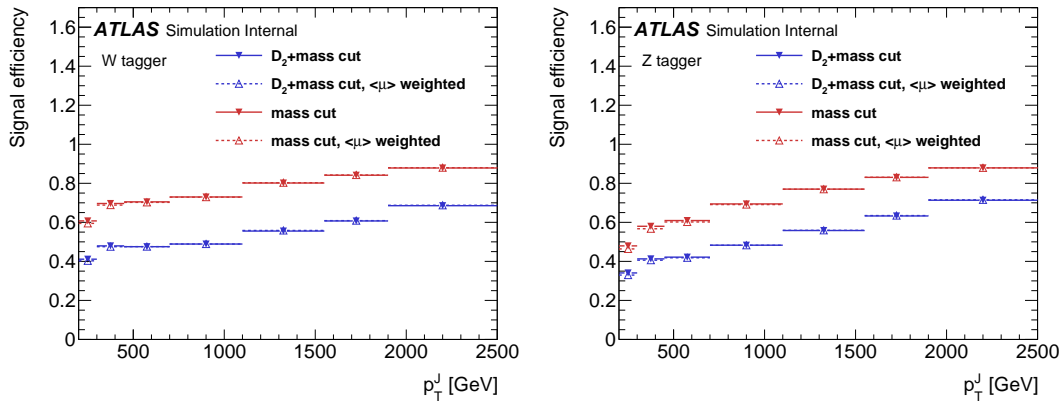


Figure 8.4: Natasha write caption

854 8.3.3 Variable Radius jets

855 To more accept more boosted Z bosons decaying to $b\bar{b}$ that would normally be
 856 rejected due to topological cuts discussed 9.4 variable radius (VR) track jets are
 857 used to identify b -jets (discussed in 8.3.4) within the catchment area of large- R
 858 jets [15]. VR jets are constructed from ID tracks using the anti- k_t algorithm with
 859 a radius parameter that depends on the p_T of the track, shown in Equation 8.5.

$$R_{eff}(p_{T,i}) = \frac{\rho}{p_{T,i}} \quad (8.5)$$

860 For this search $\rho = 30$ GeV and an upper and lower limit on cone size are set
 861 to 0.02 and 0.4, respectively, to prevent unphysical asymptotic behavior of ρ .
 862 Collinear VR jets are possible, so track jets that are not separated by the the
 863 smaller jet's cone size are not used. Additionally, VR jets are required to have
 864 $p_T > 10$ GeV and $|\eta| < 2.5$.

865 **8.3.4 Jet Flavor Tagging**

866 To further classify events, the small-R and VR jets originating from a b-quark
867 are classified using a multivariate b -tagging algorithm (BDT), MV2c10 [cite G 210
868 199]. This algorithm uses the impact parameters of the jet's ID tracks, secondary
869 vertices (if they exist), and reconstructed flight paths of b and c hadrons in the
870 jet to determine if the jet was induced by a b -quark. For this analysis the 85%
871 efficient working point of this algorithm is used giving c , τ , and light-flavor jet
872 rejection of 3, 8, and 34 respectively in simulated $t\bar{t}$ samples.

873 **8.4 MET/Neutrinos**

874 As neutrinos are uncharged and colorless they do not leave tracks or jets in the
875 detector. For this reason, neutrinos are reconstructed calculated the E_T^{miss} , the
876 negative vector sum of p_T all the physics objects and an extra "soft" term. The
877 "soft" term accounts for energy deposits not associated with any of the objects in
878 the event. For this analysis the soft term is given by the sum p_T of all ID tracks
879 not associated with objects in the event. The selected tracks must be matched to
880 the primary vertex, which decreases pile-up contamination [cite G 217 218]. The
881 tight working point is used [Natasha look up what this means].

882 **8.5 Overlap Removal**

883 Reconstructed jets and leptons in this analysis can arise from the same energy
884 deposits. For instance, a cluster of energy from an electron can also be a valid
885 calorimeter seed for a jet. To mitigate this confusion of multiple objects originating
886 from a single jet or lepton overlapping objects are removed via a procedure referred
887 to a overlap removal. In this procedure the separation of the two objects, $\Delta(R) =$

888 $\sqrt{(\Delta\eta)^2 + (\Delta\phi)^2}$ determines which object is removed from the event.

889 The overlap selections used in this analysis are:

- 890 - when an electron shares a track with another electron with the lower p_T
891 electron is rejected, as it is more likely to be a fake electron
- 892 - when a muon and electron share a track the muon is rejected if it is a
893 calo-muon, otherwise the electron is rejected
- 894 - when $\Delta R < 0.2$ for an electron and jet, the jet is rejected to maximize signal
895 acceptance
- 896 - when $\Delta R > 0.2$ for an electron and jet, the electron is rejected as likely
897 originated from decays within the jet
- 898 - when $\Delta R < \min(0.4, 0.04 + 10\text{GeV}/p_T^\mu)$ the muon is rejected, again maximiz-
899 ing signal acceptance, otherwise the jet is rejected
- 900 - when $\Delta R < 1.0$ for the a large-R jet and electron, the jet is rejected

901 8.6 Reconstructed Resonance Mass (m_{WV})

902 The WV system mass, m_{WV} is reconstructed from the lepton, neutrino, and
903 hadronically-decaying boson candidate. The momentum of the neutrino along the
904 z -direction is obtained by constraining the W boson mass of the lepton neutrino
905 system to be $80.3 \text{ GeV}/c^2$. For complex solutions to this constraint, p_Z is taken
906 as the real component of the solution. For real solutions, the one with the smaller
907 absolute value is used. For the resolved analysis, m_{WV} is reconstructed by con-
908 straining the $W(Z)$ dijet system in the SRs, which improves the mass resolution:

$$p_{T,jj}^{corr} = p_{T,jj} \times \frac{m_{W/Z}}{m_{jj}} \quad (8.6)$$

$$m_{jj}^{corr} = m_{W/Z} \quad (8.7)$$

909 where m_{jj} and $m_{W/Z}$ are the reconstructed invariant mass of the hadronically-
910 decaying W/Z boson and the PDG values of the W/Z boson masses, respectively.
911 The reconstructed resonance mass is the final discriminating variable in this anal-
912 ysis. The distribution of this variable in the CR and SRs are used in the final
913 likelihood fit to search for evidence of an excess of events due to BSM resonances.
914 The distribution of m_{WV} are shown in Figures 12.1-12.9.

915 **Chapter 9**

916 **Event Selection and**

917 **Categorization**

918 **9.1 Pre-selection**

919 Before applying topological cuts to suppress backgrounds and reduce data
920 size in this search, preselection cuts are applied which include trigger and event
921 requirements. Events must contain exactly one tight lepton (no additional loose
922 leptons), the $p_T^{\ell\nu} > 75$ GeV, and there must be at least two small-R jets or one
923 large-R jet.

924 **9.2 Trigger**

925 The data were collected using the lowest unprescaled single-lepton or E_T^{miss}
926 triggers, as summarized in Table 9.1. Since the muon term is not considered in the
927 trigger E_T^{miss} calculation, the E_T^{miss} trigger is fully efficient to events with high- p_T
928 muons. For this reason, the E_T^{miss} trigger is used for events where $p_T^\mu > 150$ GeV, to
929 compensate for the poor efficiency of the single muon trigger above $p_T^\mu > 150$ GeV.

Table 9.1: The list of triggers used in the analysis.

Data-taking period	$e\nu qq$ channel	$\mu\nu qq$ ($p_T(\mu\nu) < 150$ GeV) channel	$\mu\nu qq$ ($p_T(\mu\nu) > 150$ GeV) channel
2015	HLT_e24_lhmedium_L1EM20 OR HLT_e60_lhmedium OR HLT_e120_lhloose	HLT_mu20_iloose_L1MU15 OR HLT_mu50	HLT_xe70
2016a (run < 302919) $(L < 1.0 \times 10^{34} \text{ cm}^{-2} \text{ s}^{-1})$	HLT_e26_lhtight_nod0_ivarloose OR HLT_e60_lhmedium_nod0 OR HLT_e140_lhloose_nod0 HLT_e300_etcut	HLT_mu26_ivarmedium OR HLT_mu50	HLT_xe90_mht_L1XE50
2016b (run ≥ 302919) $(L < 1.7 \times 10^{34} \text{ cm}^{-2} \text{ s}^{-1})$	same as above	same as above	HLT_xe110_mht_L1XE50
2017	same as above	same as above	HLT_xe110_pufit_L1XE55
2018	same as above	same as above	HLT_xe110_pufit_xe70_L1XE50

930 **9.3 non-VBF/VBF RNN**

931 To classify events as originating from non-VBF or VBF production a recursive
932 neural network (RNN [22]) is used. This approach is more powerful than a cut-
933 based classification as it improves signal efficiency and analysis sensitivity by
934 exploiting correlations between variables that the RNN learns. In particular, a
935 RNN architecture is ideal as it can handle variable numbers of jets in the events.

936 The RNN uses the four-momentum of candidate VBF jets to classify events
937 as VBF or non-VBF topologies. Sometimes jets are incorrectly reconstructed,
938 so the number of jets in the event is expected to vary across the input samples.
939 VBF candidate jets are identified by removing jets from the event that are likely
940 from $W/Z \rightarrow qq$. For the resolved regime this means removing the two leading
941 small-R jets from the VBF candidate jet list. For the merged regime this means
942 removing small-R jets separated by less than 1.0 in dR from the large-R jet. VBF
943 candidate jets are also required to be within $|\eta| < 4.5$. From the list of remaining
944 VBF candidate jets, the two highest- p_T jets are chosen.

945 The architecture of the RNN is shown in Figure 9.2. The RNN is composed
946 of Long Short Term Memory Cells (LSTM) that extract meaningful information
947 and retains³ it. The logic embedded in the LSTM is shown in Figure ???. LSTMs
948 are useful for VBF event classification for events with two jets, where using the
949 kinematic properties of both jets (and their correlations) will lead to more efficient
950 event classification.

951 In this RNN architecture, the VBF candidates are first passed to a masking
952 layer which checks the number of jets in the event. If there is only one jet, only one
953 vertical LSTM layer is used. The output of masking is then passed to a LSTM,
954 with a tanh activation function. The output of the LSTM is then passed to a
955 second horizontal LSTM layer (and vertical LSTM layer if there are two jets in

956 the event). Finally the output of the last LSTM cell is passed to a dense layer
957 and then to a sigmoid activation layer, leading to an overall RNN score.

958 The weights and other parameters of the network are learned by training the
959 network with VBF and non-VBF signals over 200 epochs with an Adam Optimizer
960 [14]. To prevent overfitting during training, dropout is applied to RNN weights
961 and training is truncated if the network parameters are unchanged after ten it-
962 erations [24]. Figure 9.4 shows the ROC curve for the RNN using k-fold cross
963 validation [20].

964 Figure 9.3 shows the RNN discriminant for backgrounds, non-VBF signals,
965 and VBF signals. The RNN score is ~ 0 for non-VBF signals and background
966 processes and ~ 1 for VBF processes. Figure 9.5 shows the limits for various signal
967 processes based on the RNN cut applied. Requiring the RNN score to be > 0.8
968 was chosen as it provided the best significance (and signal efficiency) for this final
969 state and the $\nu\nu qq$ and $\ell\ell qq$ channels, which this channel will be combined with
970 for future publications.

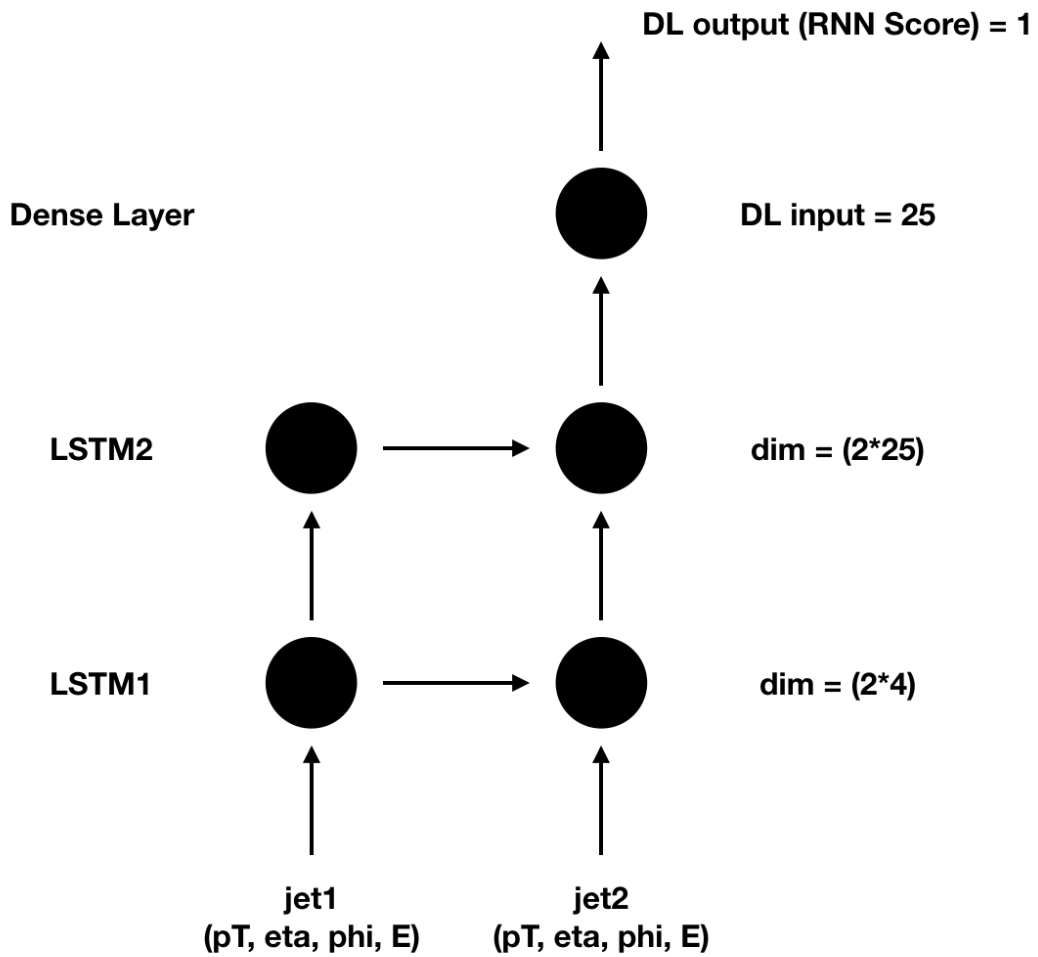


Figure 9.1: RNN architecture. Natasha add caption

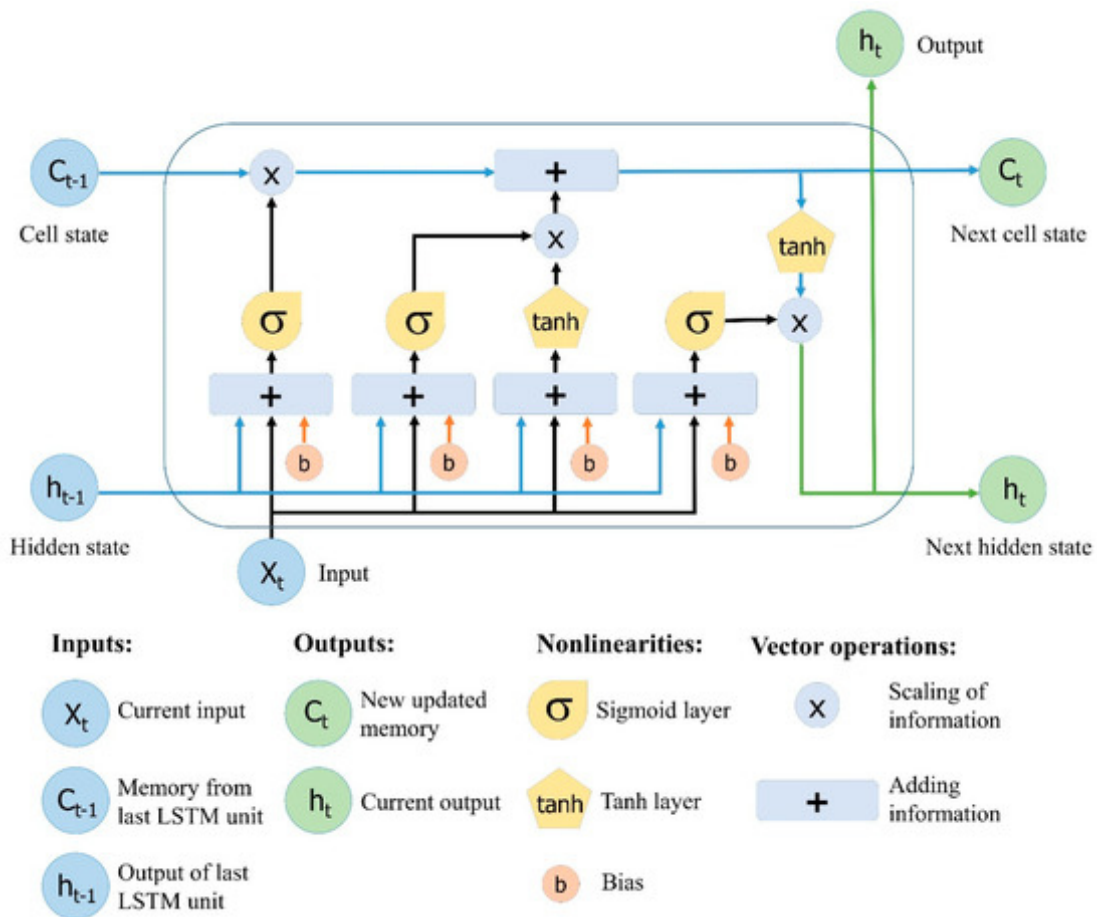


Figure 9.2: This figure shows the embedded logic in LSTM cells. This image was taken from [23], where a more in depth discussion about LSTMs may be found.

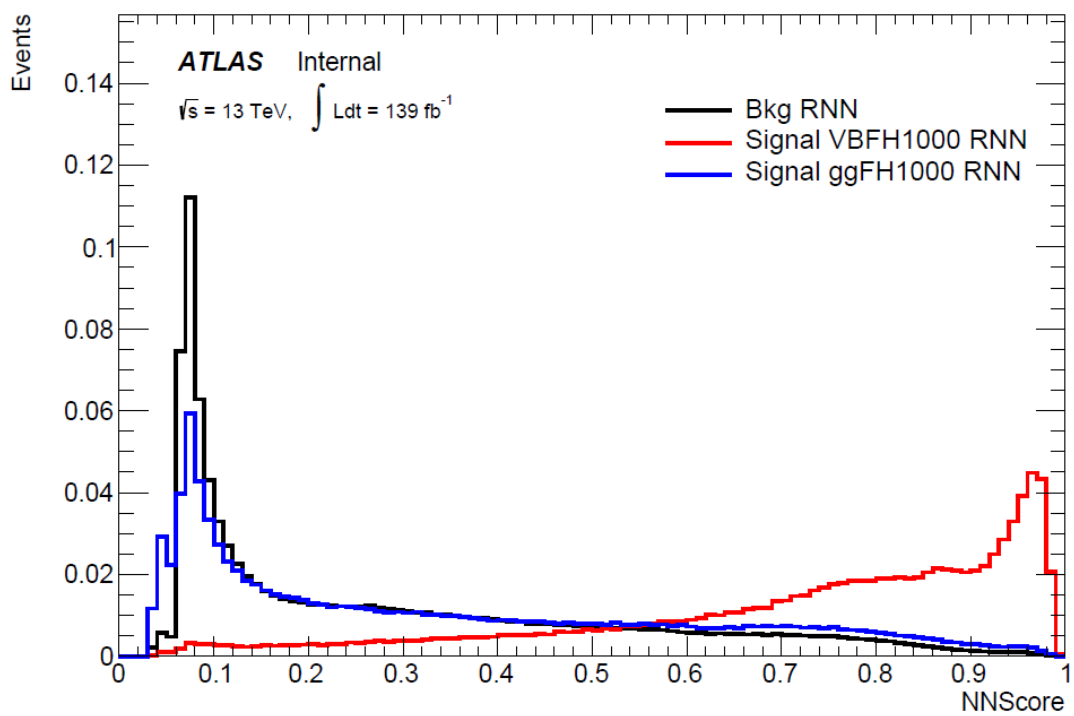


Figure 9.3: RNN Score distribution for ggF and VBF signals and backgrounds.

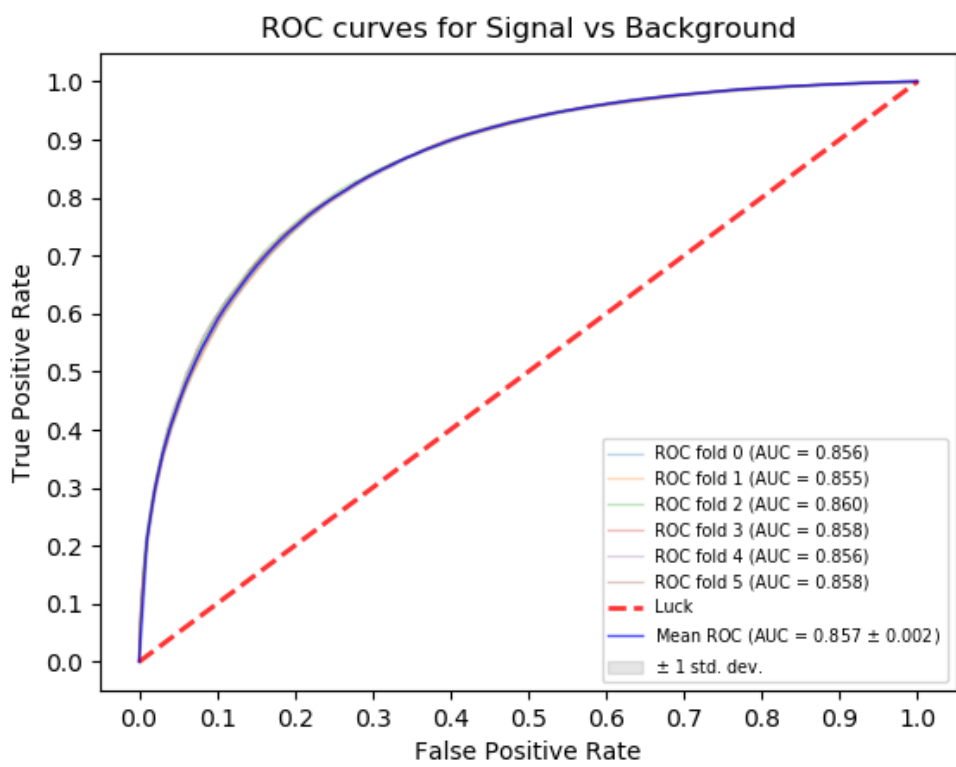


Figure 9.4: ROC curve using k-fold validation for RNN.

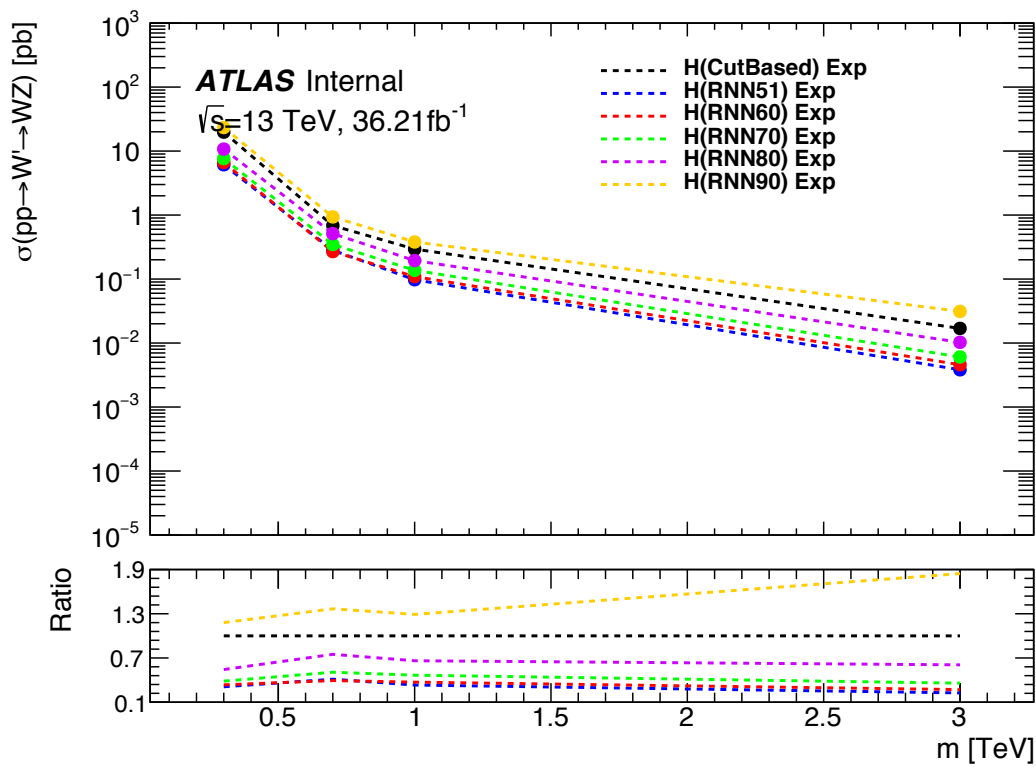


Figure 9.5: Comparison of GGF Z' limits for different RNN score selections. The bottom panel shows the ratio of the upper limits set for different RNN cuts to the cut-based analysis. In this panel smaller numbers, indicate that the expected upper limit is smaller than the cut-based analysis, which is desired.

971 9.4 Signal Region Definitions

972 Signal regions are constructed to be dominated by signal and used in the final
973 likelihood fit to look for a bump in the reconstructed resonance mass distribution.
974 Once an event is classified by the RNN, it must pass topological cuts that maximize
975 S/\sqrt{B} . To efficiently select events with a $W \rightarrow \ell\nu$ candidate exactly one tight
976 lepton is required and $E_T^{miss} > 100(60)$ GeV and $p_{T,\ell\nu} > 200(75)$ GeV in the
977 merged (resolved) analysis to suppress the fake lepton backgrounds.

978 For the merged analysis, in addition to the $W \rightarrow \ell\nu$ and $W/Z \rightarrow J$ selections
979 above, the $\min(p_{T,\ell\nu}, p_{T,J})/m_{WV} > 0.35(0.25)$ for the non-VBF (VBF) category.
980 To reduce $t\bar{t}$ contamination, events with at least one b jet with $\Delta R > 1.0$ from
981 the large-R jet are excluded. High purity signal regions require the D_2 and W/Z
982 mass window cut to be passed, whereas the low purity region only requires the
983 W/Z mass window cut to be passed.

984 For the HVT W' resonance search tagged and untagged regions are used to
985 increase signal acceptance. For events to be classified as tagged the large-R jet
986 must contain exactly two b-tagged jets. Untagged events must have no more than
987 one b-tagged jet matched to the large-R jet. These selections are shown in Table
988 9.2.

989 Events failing the merged selection are then re-analyzed in the resolved cat-
990 egory. To enhance resolved signals, the event should contain two high- p_T boson
991 candidates that are back-to-back in the ϕ as shown by the cuts in Table 9.3.
992 Again, to suppress the $t\bar{t}$ backgrounds, events are required to have no additional
993 b-jets. A summary of the resolved selections is shown in Table 9.3.

994 The analysis cutflow in Figure 9.6 which shows how the different categories
995 are prioritized. Events classified as VBF events are classified as Merged high
996 purity, low purity or resolved signal region selections sequentially. If the event

Table 9.2: Summary of selection criteria used to define the signal region (SR), W +jets control region (W CR) and $t\bar{t}$ control region ($t\bar{t}$ CR) for merged 1-lepton channel.

Selection	SR		W CR (WR)		$t\bar{t}$ CR (TR1)			
	HP	LP	HP	LP	HP	LP		
$W \rightarrow \ell\nu$	Num of Tight leptons			1				
	Num of Loose leptons			0				
	E_T^{miss}			> 100 GeV				
	$p_T(\ell\nu)$			> 200 GeV				
$W/Z \rightarrow J$	Num of large- R jets			≥ 1				
	D_2 cut	pass	fail	pass	fail	pass	fail	
	W/Z mass window cut	pass	pass	fail	fail	pass	pass	
	Numb. of associated VR track jets b -tagged	For $Z \rightarrow J$: ≤ 1 ($= 2$) for untagged (tagged) category						
	$\min(p_{T,\ell\nu}, p_{T,J}) / m_{WV}$	> 0.35(0.25) for DY/ggF (VBF) category						
	Top-quark veto	Num of b -tagged jets outside of large- R jet	0			≥ 1		
Pass VBF selection			no (yes) for DY/ggF (VBF) category					

997 does not pass any of these selections but passes a VBF control region selection it
 998 is classified as a VBF CR event. If the event fails all VBF categories, it is then
 999 checked if it passes the Merged high purity, low purity or resolved signal region
 1000 selections (NB: for the WZ decay modes all the regions have tagged and untagged
 1001 categories). If the event fails all the non-VBF signal region selections, it is then
 1002 kept for non-VBF control region selections, if it passes those selections.

Table 9.3: The list of selection cuts in the resolved analysis for the WW and WZ signal regions (SR), $W+jets$ control region (WR) and $t\bar{t}$ control region (TR).

cuts	SR	W CR (WR)	$t\bar{t}$ CR (TR1)		
$W \rightarrow \ell\nu$	Number of Tight leptons	1			
	Number of Loose leptons	0			
	E_T^{miss}	> 60 GeV			
	$\cancel{p}_T(\ell\nu)$	> 75 GeV			
$W/Z \rightarrow jj$	Number of small-R jets	≥ 2			
	Leading jet p_T	> 60 GeV			
	Subleading jet p_T	> 45 GeV			
	$Z \rightarrow q\bar{q}$	$78 < m_{jj} < 105$ GeV	$50 < m_{jj} < 68$ GeV or $68 < m_{jj} < 98$ GeV	$105 < m_{jj} < 150$ GeV	$50 < m_{jj} < 150$ GeV
	Num. of b -tagged jets	For $Z \rightarrow jj$: ≤ 1 ($= 2$) for untagged (tagged) category			
Topology cuts	$\Delta\phi(j, \ell)$	> 1.0			
	$\Delta\phi(j, E_T^{\text{miss}})$	> 1.0			
	$\Delta\phi(j, j)$	< 1.5			
	$\Delta\phi(\ell, E_T^{\text{miss}})$	< 1.5			
	$\min(p_{T,\ell\nu}, p_{T,jj}) / m_{WW}$	$> 0.35(0.25)$ for DY/ggF (VBF) category			
Top veto	Number of additional b -tagged jets	0	≥ 1		
	Pass VBF selection	no (yes) for DY/ggF (VBF) category			

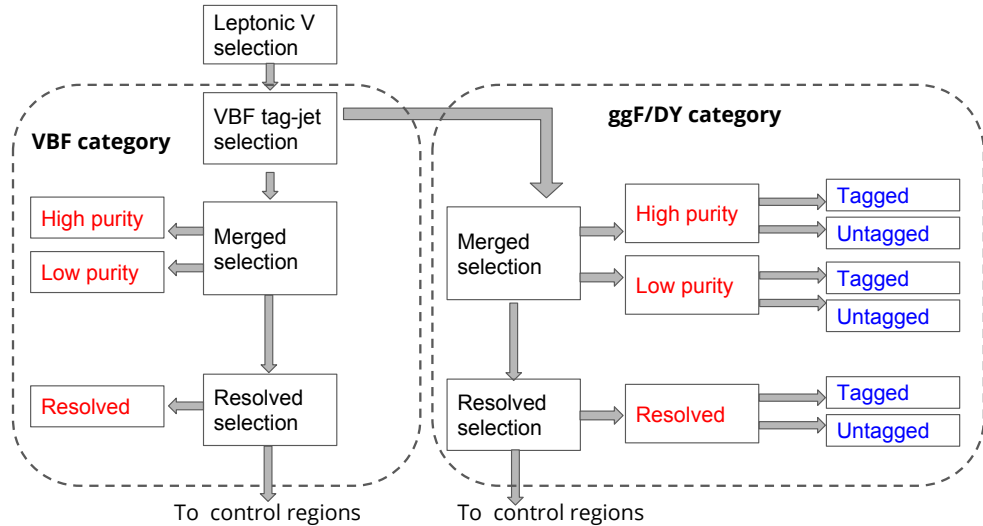


Figure 9.6: Event Categorization. Natasha write more.

1003 9.5 Selection Acceptance and Efficiency

1004 The acceptance times efficiency for the signal region selection is defined as:

$$A \cdot \epsilon = \frac{N_{\text{events selected}}^{\text{truth}}}{N_{\text{events generated}}^{\text{truth}}} \cdot \frac{N_{\text{events selected}}^{\text{reco}}}{N_{\text{events selected}}^{\text{truth}}} = \frac{N_{\text{events selected}}^{\text{reco}}}{N_{\text{events generated}}^{\text{truth}}} \quad (9.1)$$

1005 The distributions of $A \cdot \epsilon$ as a function of the resonance mass for the different spin
1006 models are shown in Figures 9.8 - ??.

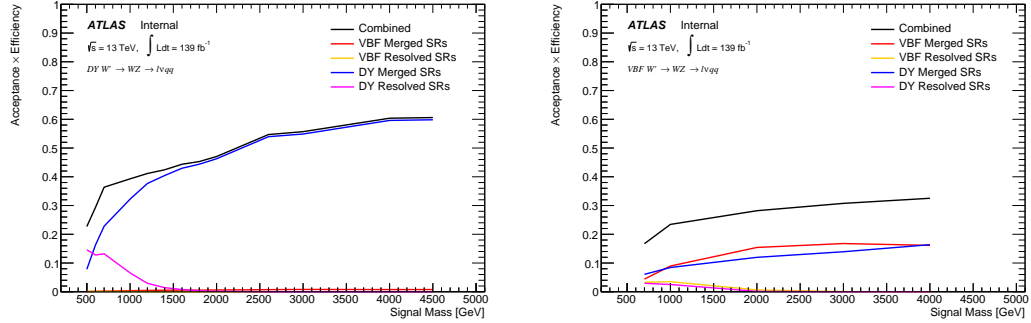


Figure 9.7: Selection acceptance times efficiency for the $W' \rightarrow WZ \rightarrow \ell\nu qq$ events from MC simulations as a function of the W' mass for (a) Drell-Yan and (b) VBF production, combining the merged HP and LP signal regions of the $WW \rightarrow \ell\nu J$ selection and the resolved regions of the $WW \rightarrow \ell\nu jj$ selection.

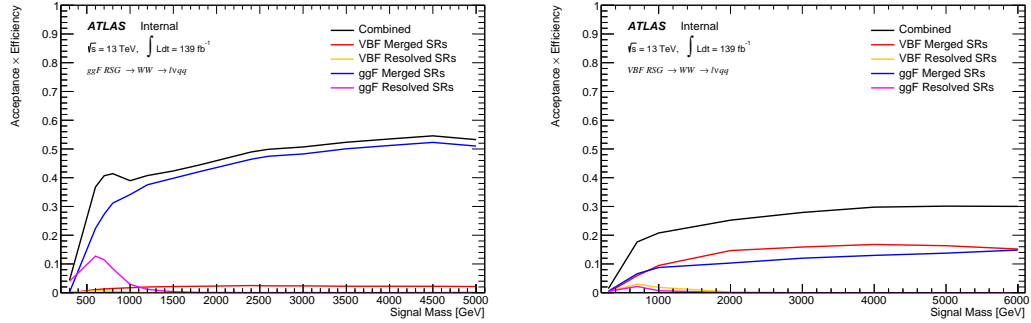


Figure 9.8: Selection acceptance times efficiency for the $G \rightarrow WW \rightarrow \ell\nu qq$ events from MC simulations as a function of the G mass for (a) Drell-Yan and (b) VBF production, combining the merged HP and LP signal regions of the $WW \rightarrow \ell\nu J$ selection and the resolved regions of the $WW \rightarrow \ell\nu jj$ selection.

1007 **9.6 Background Estimate**

1008 Backgrounds from VV , $t\bar{t}$, single-top, $W+\text{jets}$, $Z+\text{jets}$ are simulated as de-
1009 scribed in 7.2. The dominant backgrounds for this search are from $W+\text{jet}$ and $t\bar{t}$
1010 processes. To more accurately model the distribution of m_{VV} from these back-
1011 grounds in the SRs, control regions are constructed for each as described in 9.6.1.
1012 The $t\bar{t}$ and $W+\text{jets}$ control regions are called TCR and WCR, respectively. There
1013 are separate control regions for VBF and non-VBF regions as well as for each
1014 region (merged HP, merged LP, resolved). For the HVT W' search there are also
1015 tagged and untagged control regions (where tagged refers to events with two b -jets
1016 inside the large-R jet).

1017 The aforementioned backgrounds containing real leptons and are well-modeled
1018 with simulated samples. Backgrounds with fake leptons (also referred to as the
1019 multijet background) are not well-modeled with simulation. For this reason, the
1020 multijet background is extracted from data as described in 9.6.2.

1021 **9.6.1 Control Regions**

1022 The distributions for the variables used in merged analysis for top control
1023 regions are shown in Figure 9.9-9.12.

1024 The distributions for the variables used in the resolved analysis in the TCR
1025 are shown in Figure 9.13, 9.14.

1026 To more accurately model the two dominant backgrounds in this analysis,
1027 $W+\text{jets}$ and $t\bar{t}$, control regions are constructed for each. These control regions
1028 are dominated by these processes and used to extract normalization factors in
1029 the final likelihood fit that are then used in the signal region estimates. For the
1030 $t\bar{t}$ control region the event must contain at least one such b jet. The WCR is
1031 constructed using the $m_{jj/J}$ mass window sidebands. All other backgrounds are

₁₀₃₂ estimated using simulation, except fake lepton backgrounds, which are derived
₁₀₃₃ using a data-driven method.

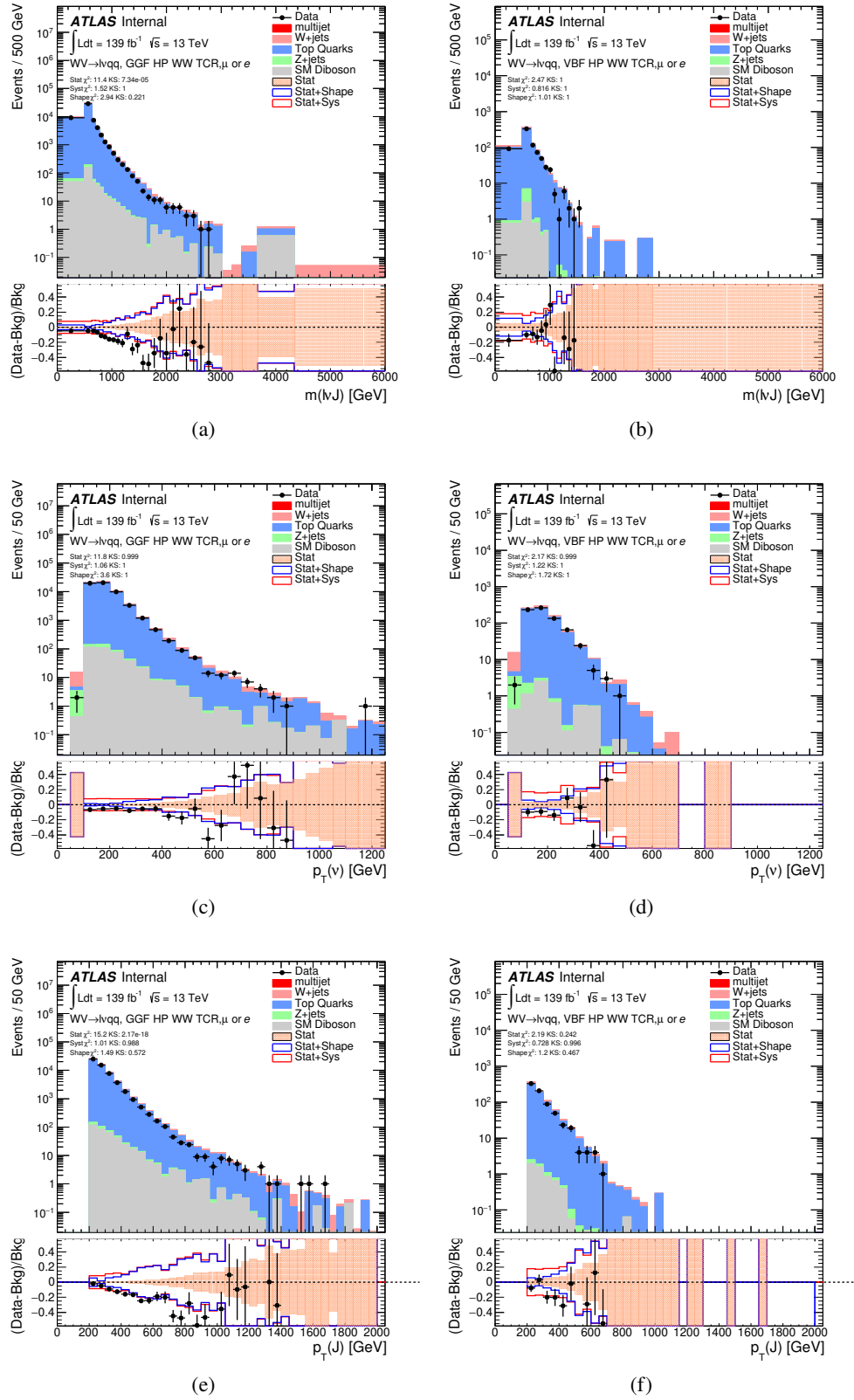


Figure 9.9: Data MC comparison for the merged WW HP TCR. The bottom panel shows the ratio of the difference between data and simulation to simulation⁹¹. The red bands include the all systematic and statistical uncertainties on the background.

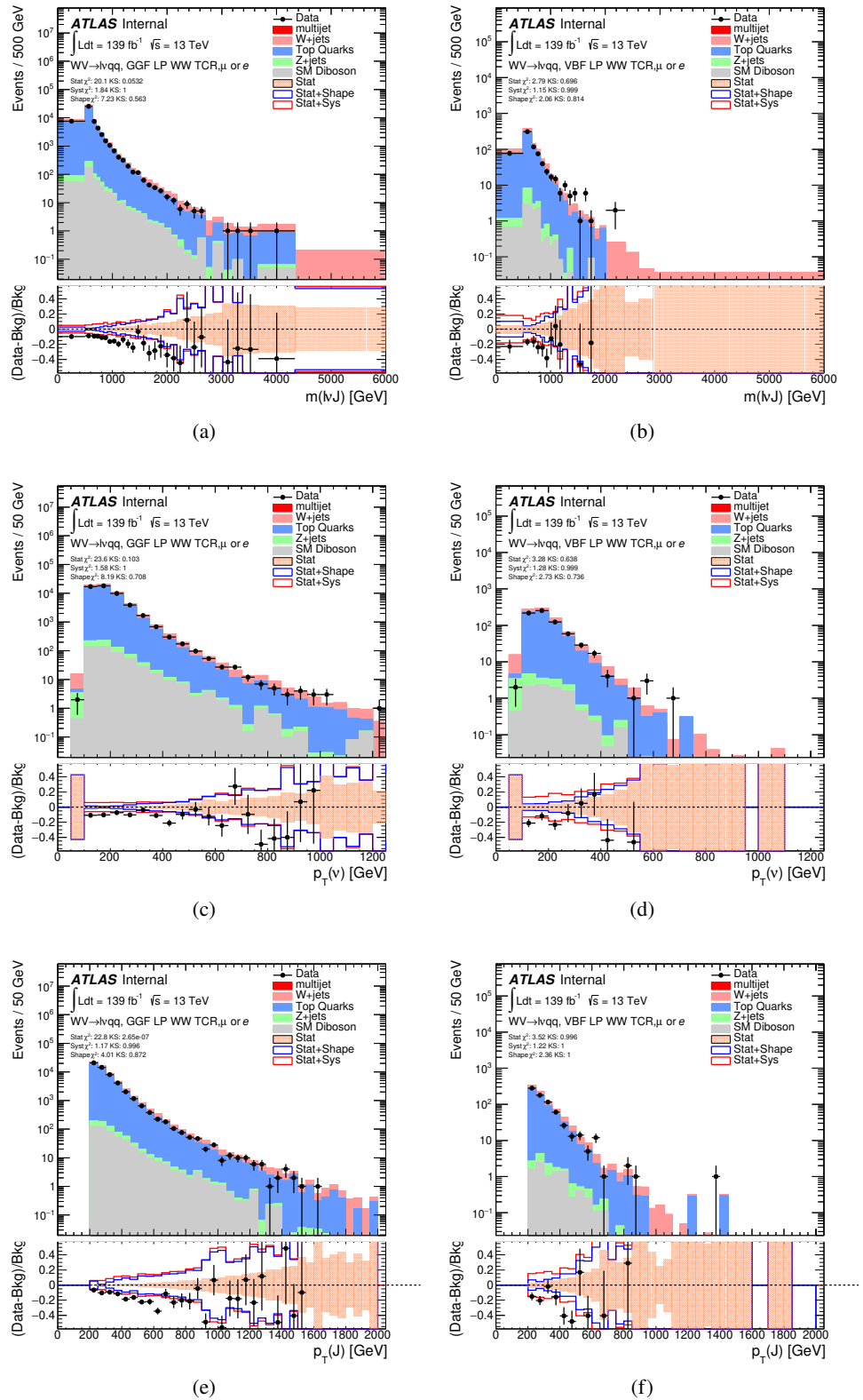


Figure 9.10: Data MC comparison for the merged WW LP TCR. The bottom panel shows the ratio of the difference between data and simulation to simulation. The red bands include the all systematic and statistical uncertainties on the background.

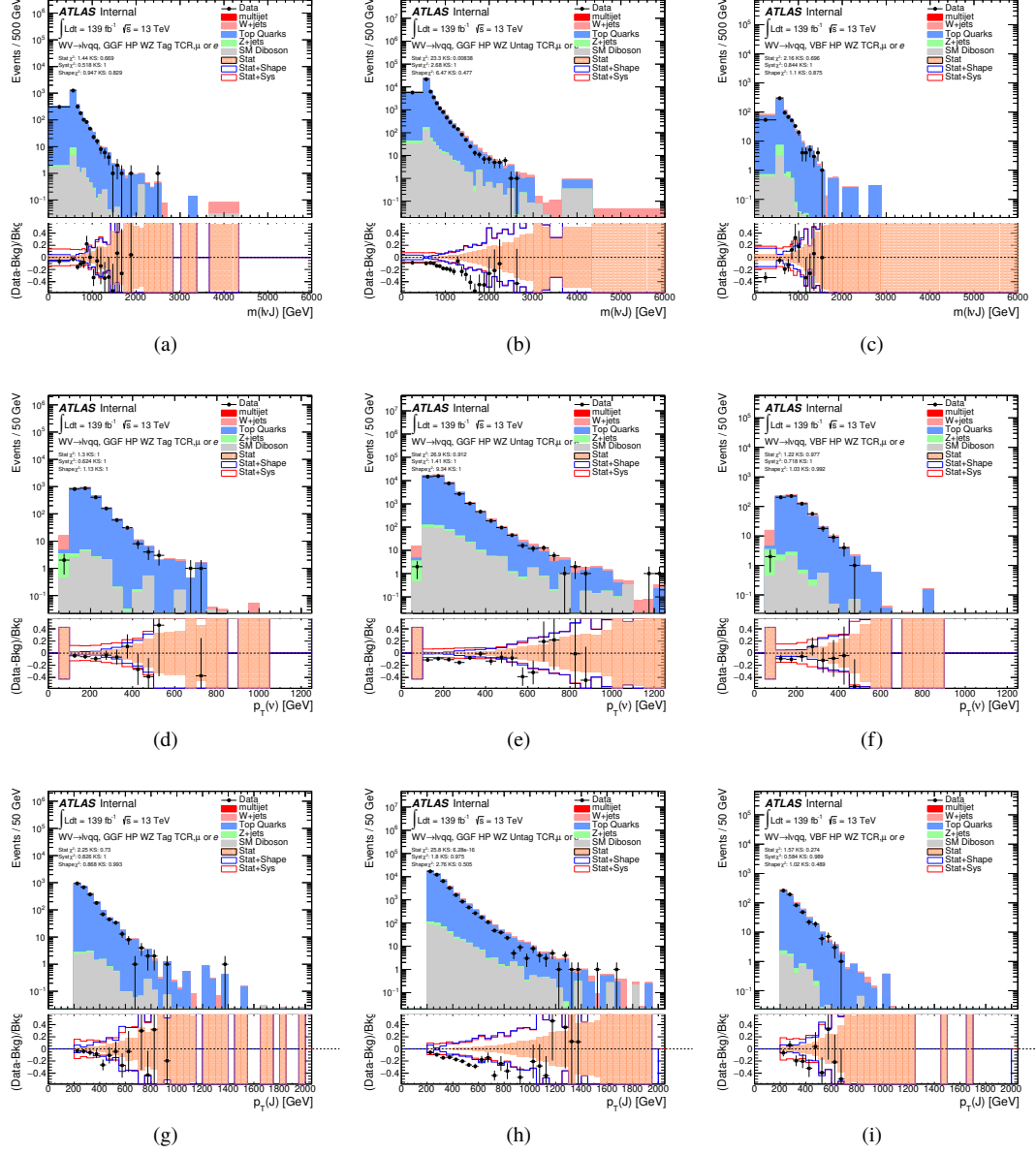


Figure 9.11: Data MC comparison for the merged WZ HP TCR. The bottom panel shows the ratio of the difference between data and simulation to simulation. The red bands include the all systematic and statistical uncertainties on the background.

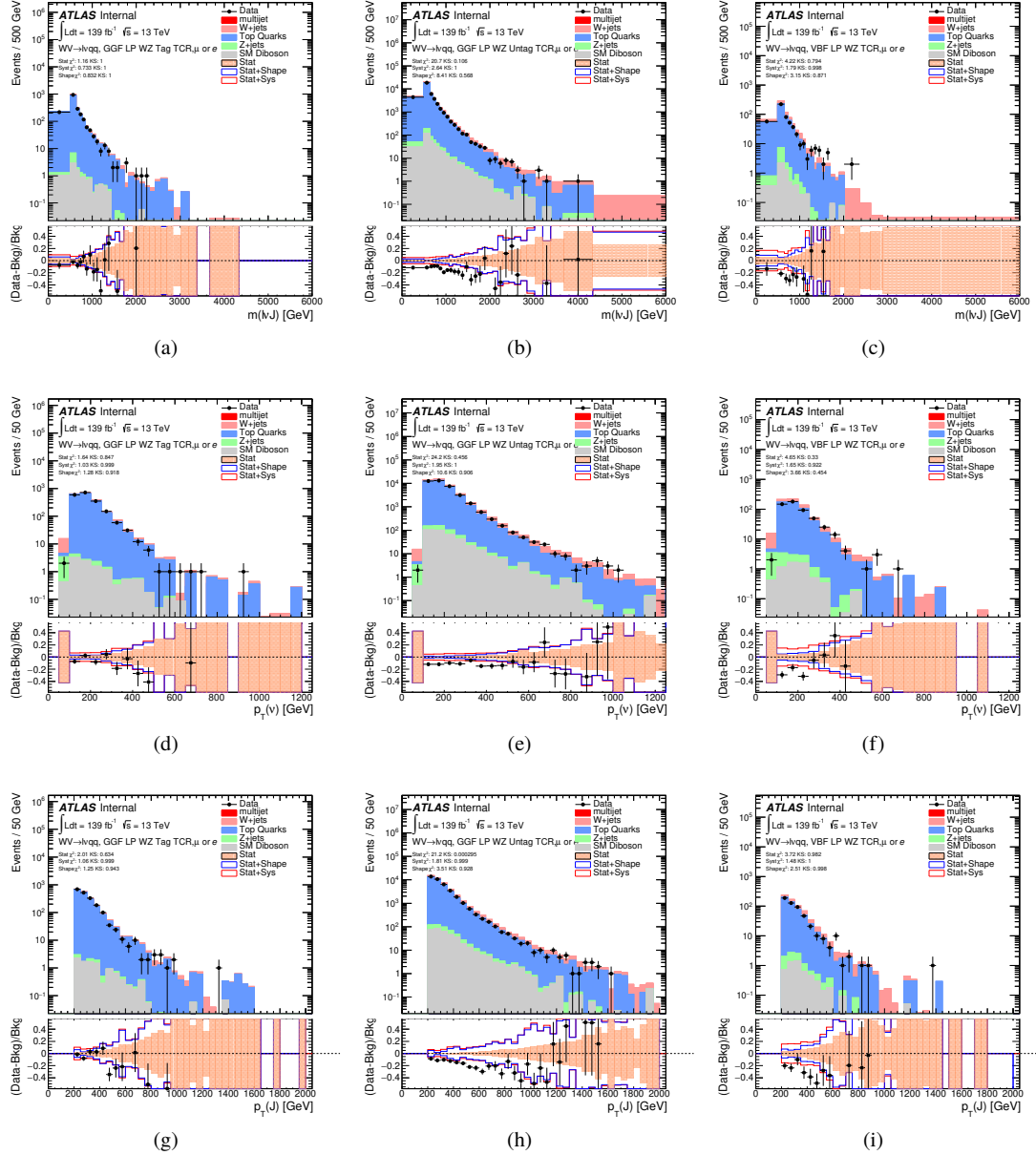


Figure 9.12: Data MC comparison for the merged WZ LP TCR. The bottom panel shows the ratio of the difference between data and simulation to simulation. The red bands include the all systematic and statistical uncertainties on the background.

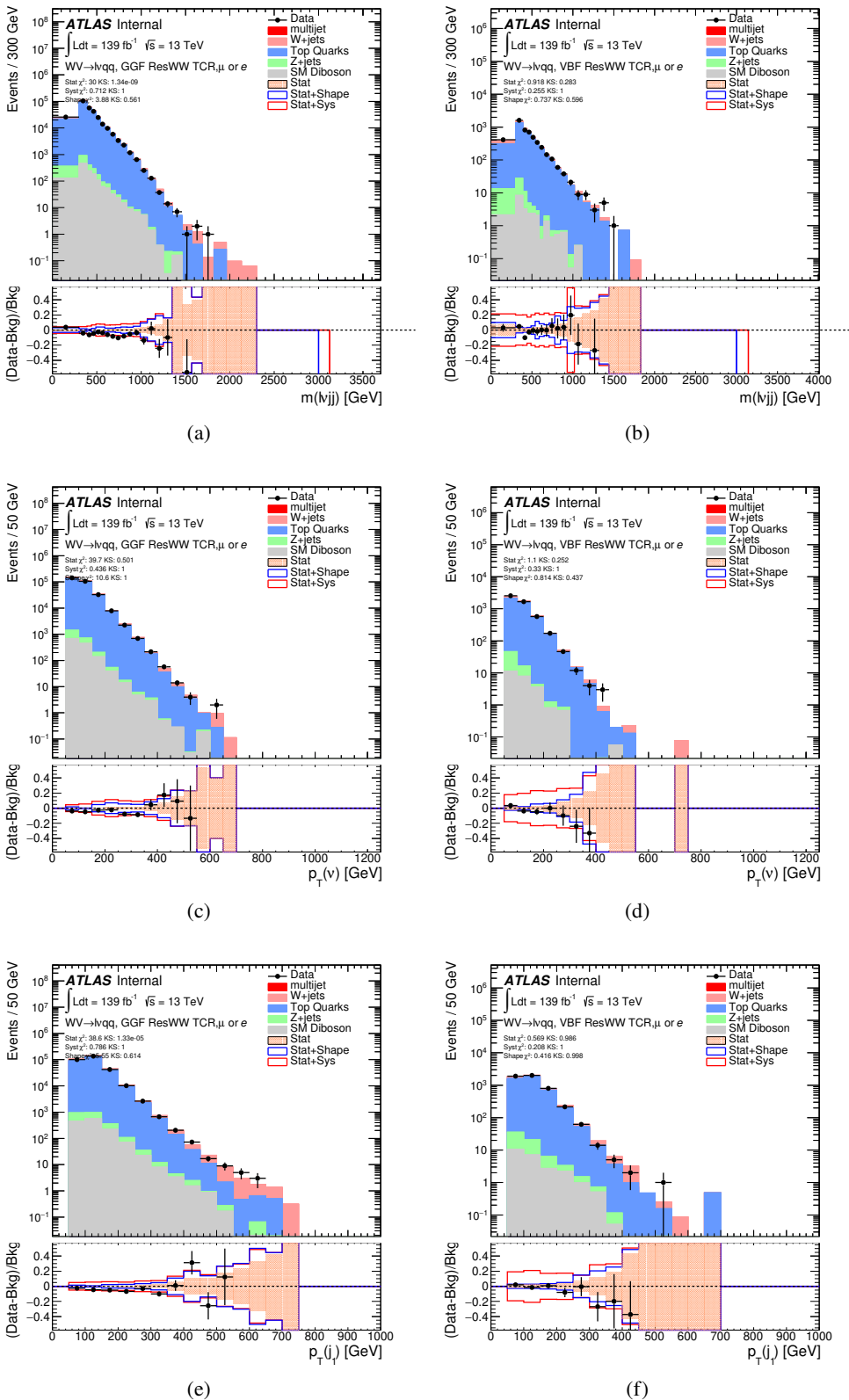


Figure 9.13: Data MC comparison for the resolved WW TCR. The bottom panel shows the ratio of the difference between data and simulation to simulation. The red bands include the all systematic and statistical uncertainties on the background.⁹⁵

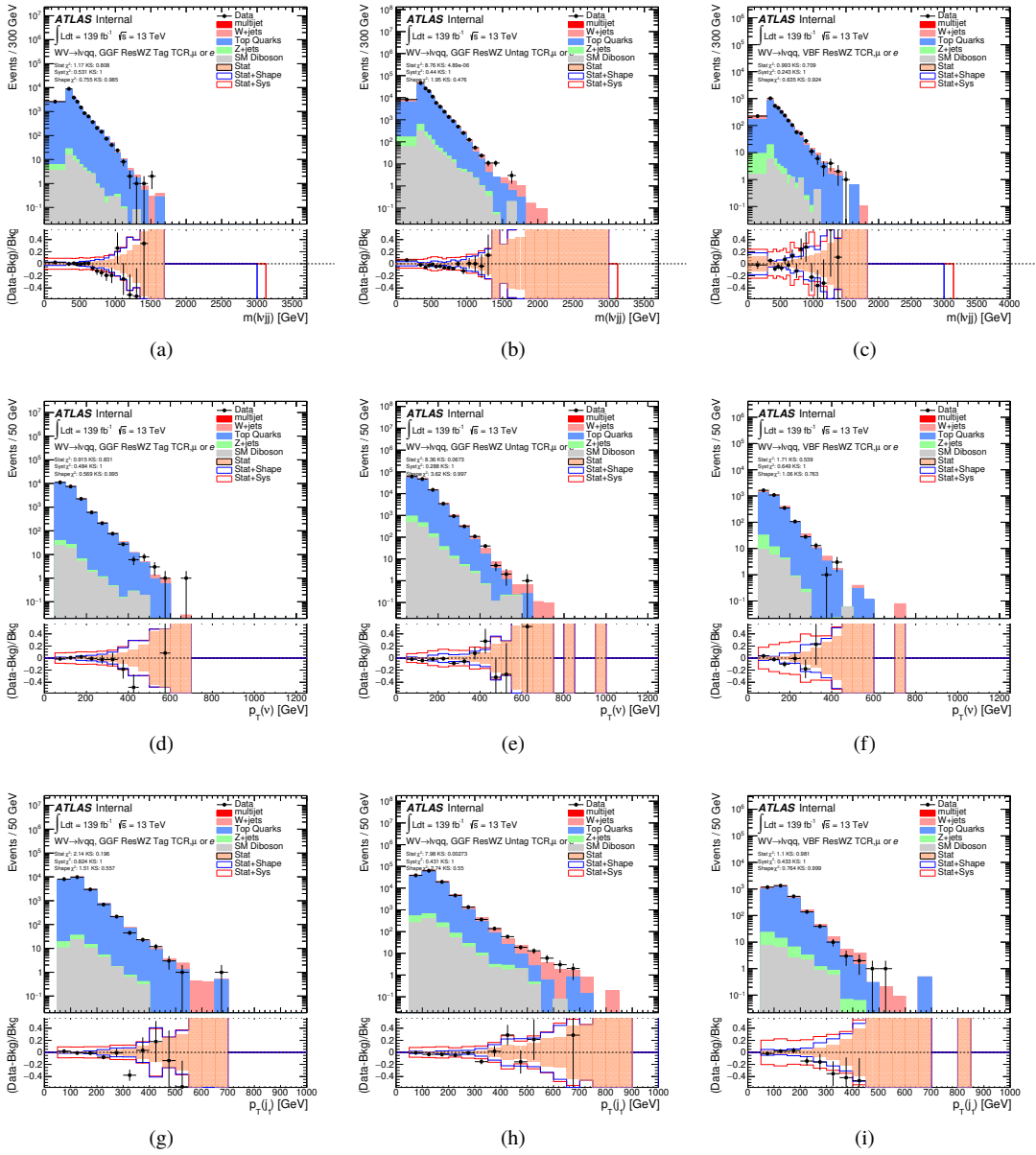


Figure 9.14: Data MC comparison for the resolved WZ TCR. The bottom panel shows the ratio of the difference between data and simulation to simulation. The red bands include the all systematic and statistical uncertainties on the background.

1034 **9.6.2 Fake Lepton Backgrounds**

1035 The fake lepton backgrounds for this search are not well-modeled with simu-
1036 lation. For this reason, this background is extracted from data. Fake electrons
1037 often arise from fake jets and converted photons while non-prompt muons usually
1038 arise from heavy flavor decay products.

1039 Fake electrons generally fail the electron ID criteria and fake muons fail the
1040 muon isolation requirement. Therefore, separate multijet samples are derived for
1041 the fake electron and muon samples. For each sample the m_{WV} template shape
1042 is derived for the SR and WCR selections using the same SR and WCR cuts but
1043 with inverted lepton requirements as seen in Table 9.4. NB: By inverting the
1044 lepton isolation/identification criteria the SRs and CRs are orthogonal.

1045 To derive the multijet template in a given SR, first the multijet template in
1046 the WCR is derived, called the MJCR template. This template is calculated using
1047 events that pass the WCR selection but with the inverted lepton criteria. The
1048 E_T^{miss} distribution for the MJCR is given by the difference between data and the
1049 simulated samples in the MJCR. The E_T^{miss} distribution of those events is then
1050 added to the simulated backgrounds in the WCR. The floating background and
1051 multijet normalizations of the MJCR in this region are then fit to the data. The
1052 fitted MJCR is then used as the multijet sample in the WCR.

1053 The fitted normalizations from the MJCR template are then used to construct
1054 the multijet template in the SR (MJSR). The MJSR is constructed from events
1055 that pass the SR selections but with the inverted lepton criteria. Again, the
1056 difference between the data and simulated backgrounds in this region gives MJSR
1057 template shape in m_{WV} . This shape is then scaled by the fitted normalizations
1058 from the MJCR. These fitted electron and muon multijet templates are then
1059 used as the multijet samples in the SRs. The normalizations of the electron and

1060 muon multijet samples are parameters in the final likelihood fit.

1061 This template method was validated using WCR and full Run 2 data. The
1062 results of the fit are shown in Table 9.5. The multijet contribution in the muon
1063 channel for $p_T^W > 150$ GeV is consistent with zero, and therefore neglected in
1064 the final fit. Applying the extracted normalization factor to MJCR in WCRs for
1065 various kinematic variables such as E_T^{miss} , W transverse mass, lepton p_T , and the
1066 invariant mass as show in Figures 9.16 -9.25. These figures show good agreement
1067 between the data and background estimate.

Table 9.4: Definitions of “inverted” leptons used in multijet control region

	Criterion	signal lepton	inverted lepton
Electron	ID	TightLH	MediumLH !TightLH
	Calo Isolation	FixedCutHighPtCaloOnlyIso	FixedCutHighPtCaloOnlyIso
Muon	ID	WHSignalMuon	WHSignalMuon
	Track Isolation	FixedCutTightTrackOnlyIso	!FixedCutTightTrackOnlyIso $ptvarcone30/pt < 0.07^*$

*Only applied to events with $pTW < 150\text{GeV}$

1068

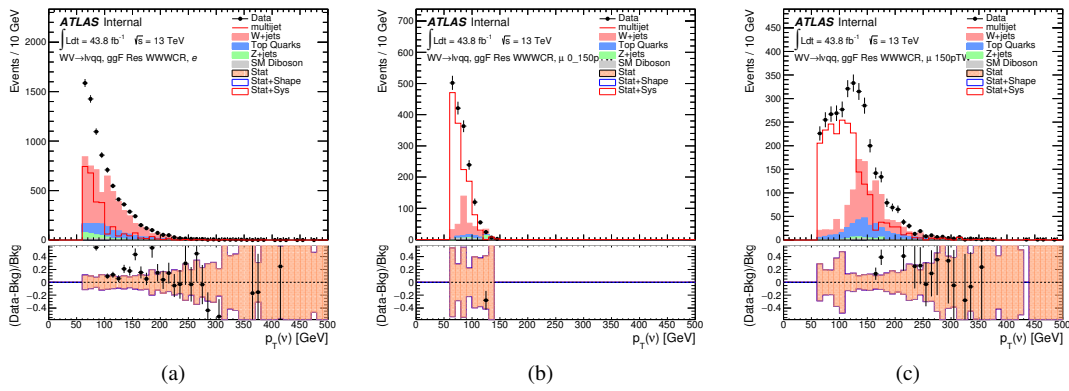


Figure 9.15: The E_T^{miss} distribution in MJCR for 2017 data in the electron channel(left), muon channel with W -boson $pT < 150$ GeV (center) and > 150 GeV (right). Multi-jet templates are calculated as remaining data components after excluding known MC

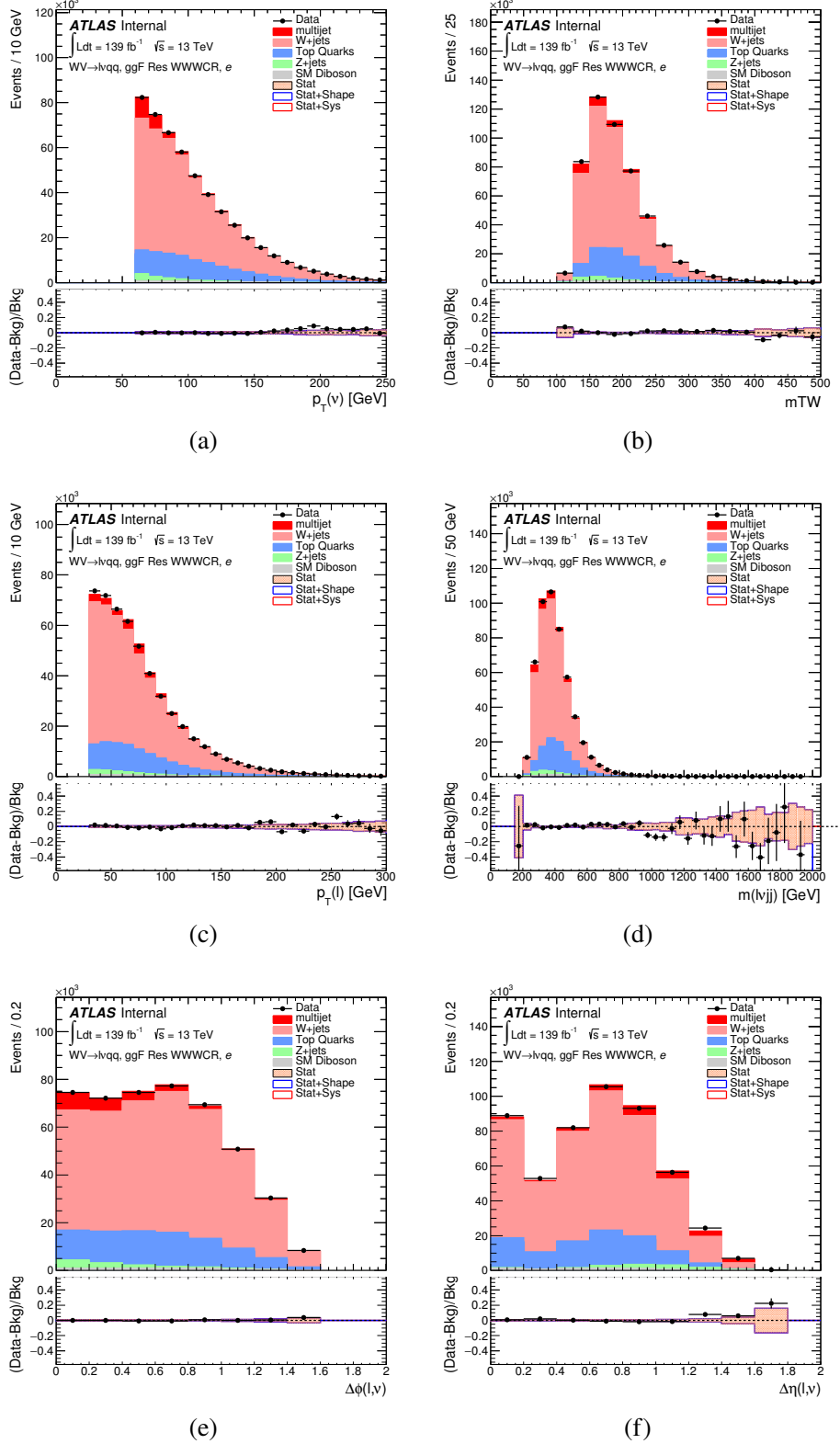


Figure 9.16: Postfit Data/MC comparison of distributions of E_T^{miss} , m_T , lepton and neutrino p_T , $m_{l\nu jj}$, lepton- ν angular distance in the WW electron channel. The MJ template is obtained from the pre-MJ-fit.

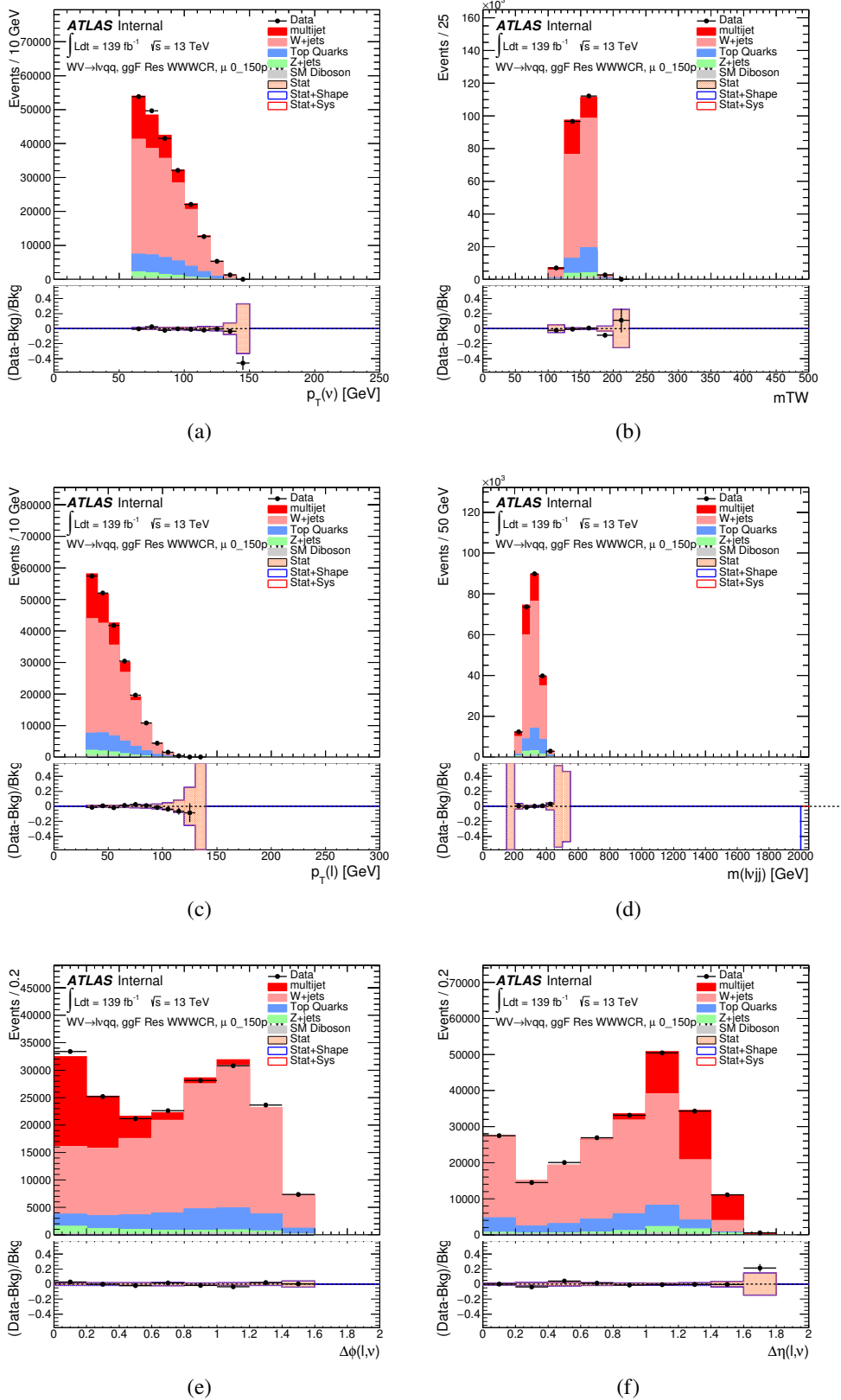


Figure 9.17: Postfit Data/MC comparison of distributions of E_T^{miss} , m_T^W , lepton and neutrino p_T , $m_{l\nu jj}$, lepton- ν angular distance in the WW muon channel. The MJ template is obtained from the pre-MJ-fit.

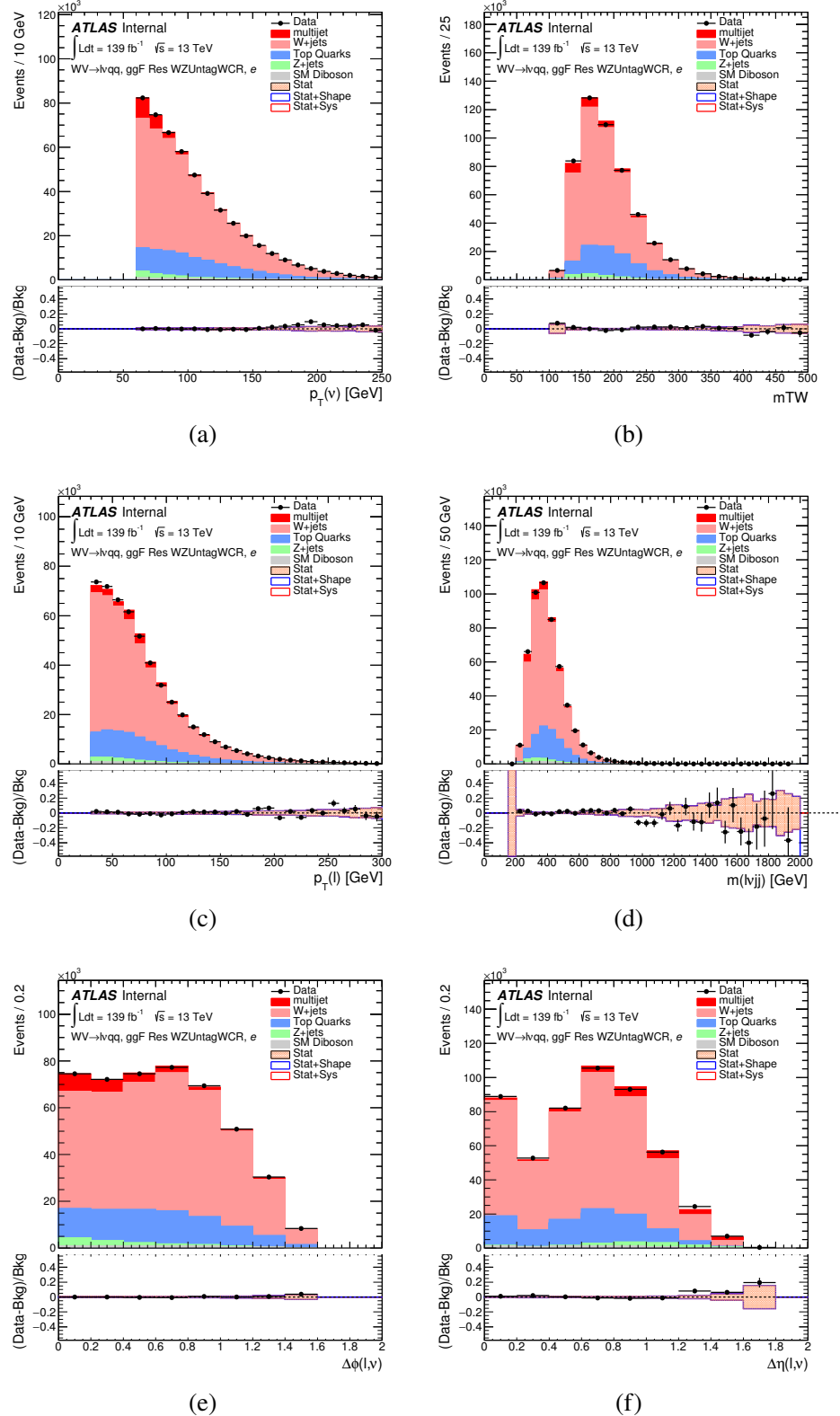


Figure 9.18: Postfit Data/MC comparison of distributions of E_T^{miss} , m_T^W , lepton and neutrino p_T , $m_{l\nu jj}$, lepton- ν angular distance in the WZ untag electron channel. The MJ template is obtained from the pre-MJ-fit.

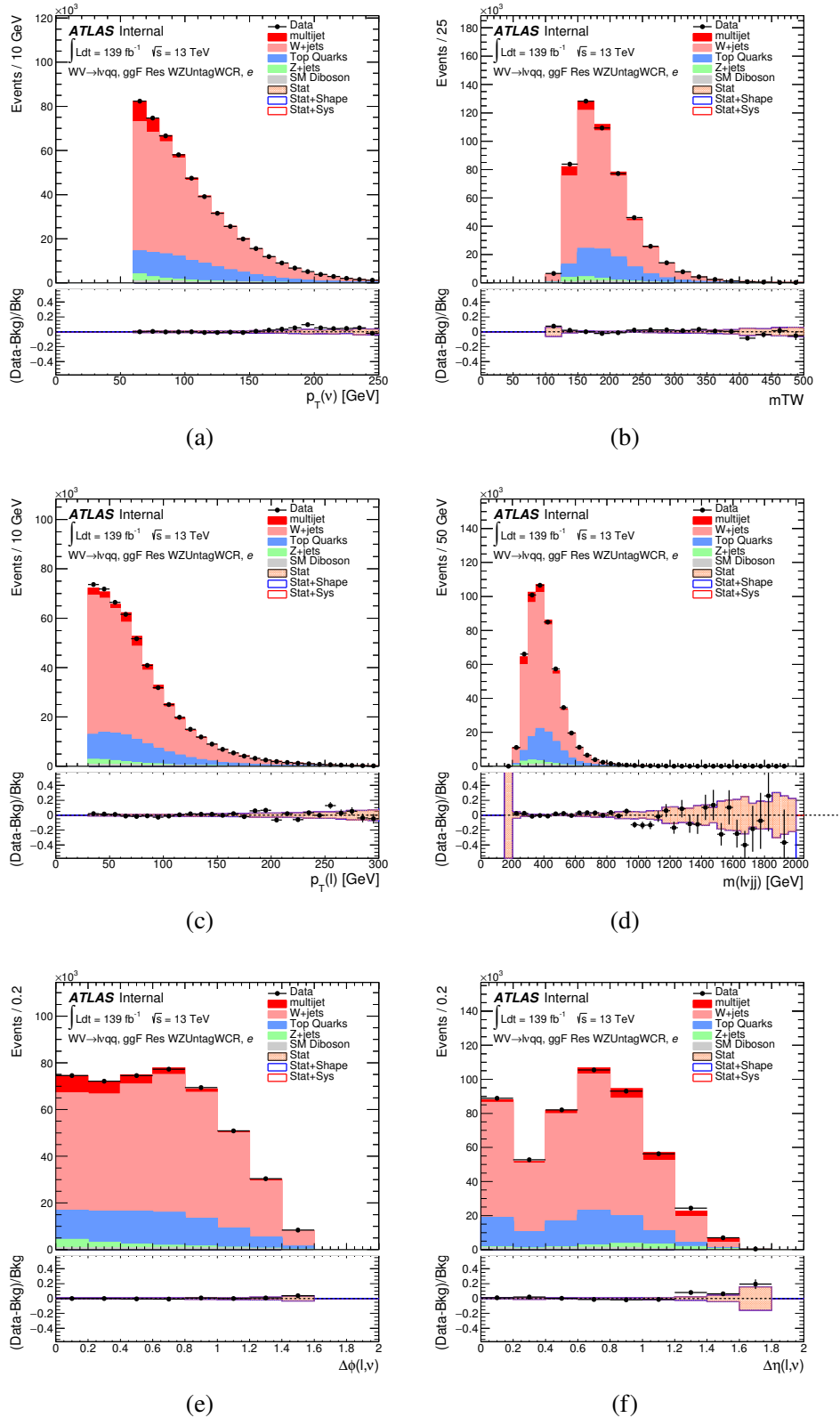


Figure 9.19: Postfit Data/MC comparison of distributions of E_T^{miss} , m_T^W , lepton and neutrino p_T , $m_{l\nu jj}$, lepton- ν angular distance in the WZ untag muon channel. The MJ template is obtained from the pre-MJ-fit.

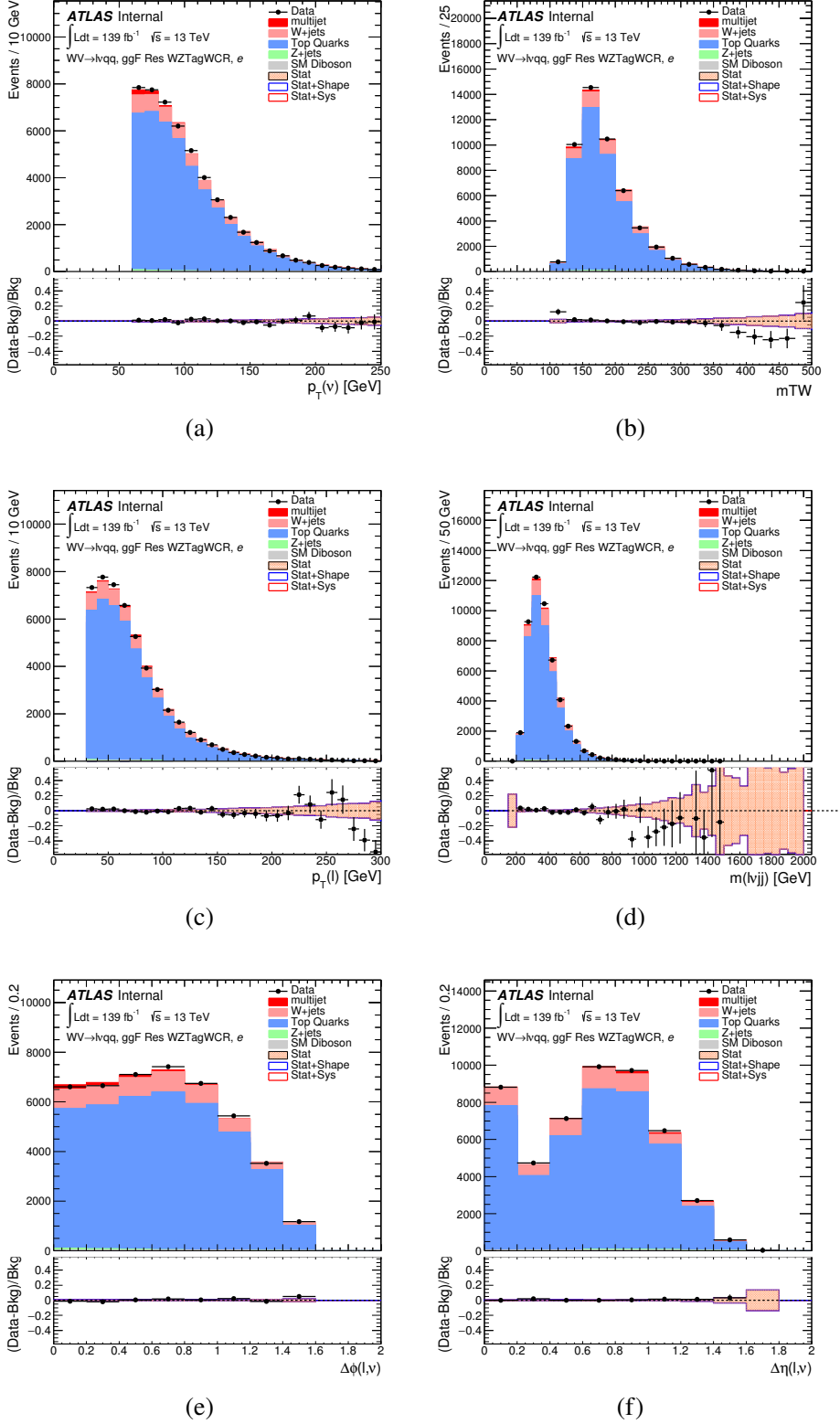


Figure 9.20: Postfit Data/MC comparison of distributions of E_T^{miss} , m_T^W , lepton and neutrino p_T , $m_{l\nu jj}$, lepton- ν angular distance in the WZ untag electron channel. The MJ template is obtained from the pre-MJ-fit.

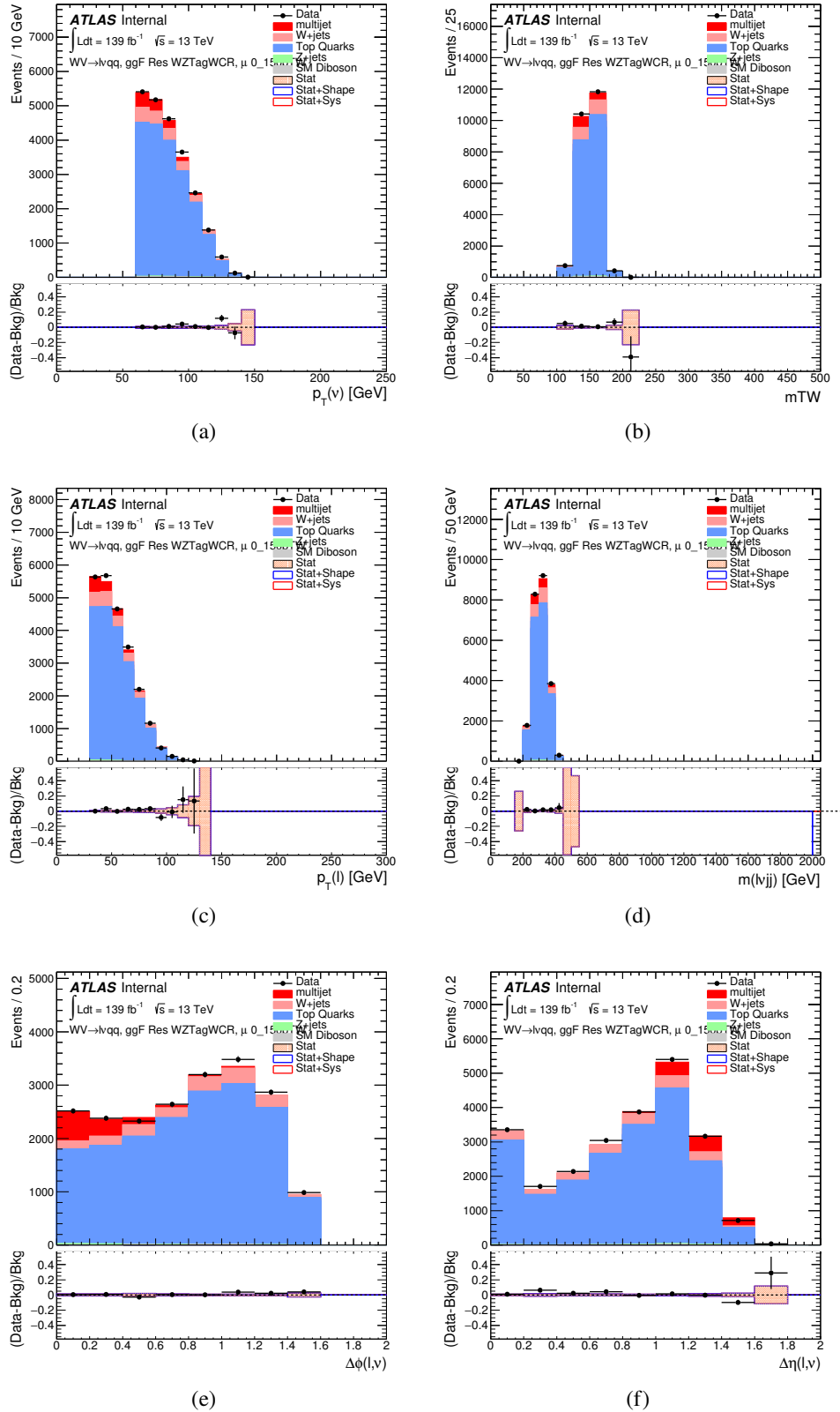


Figure 9.21: Postfit Data/MC comparison of distributions of E_T^{miss} , m_T^W , lepton and neutrino p_T , $m_{l\nu jj}$, lepton- ν angular distance in the WZ untag muon channel. The MJ template is obtained from the pre-MJ-fit.

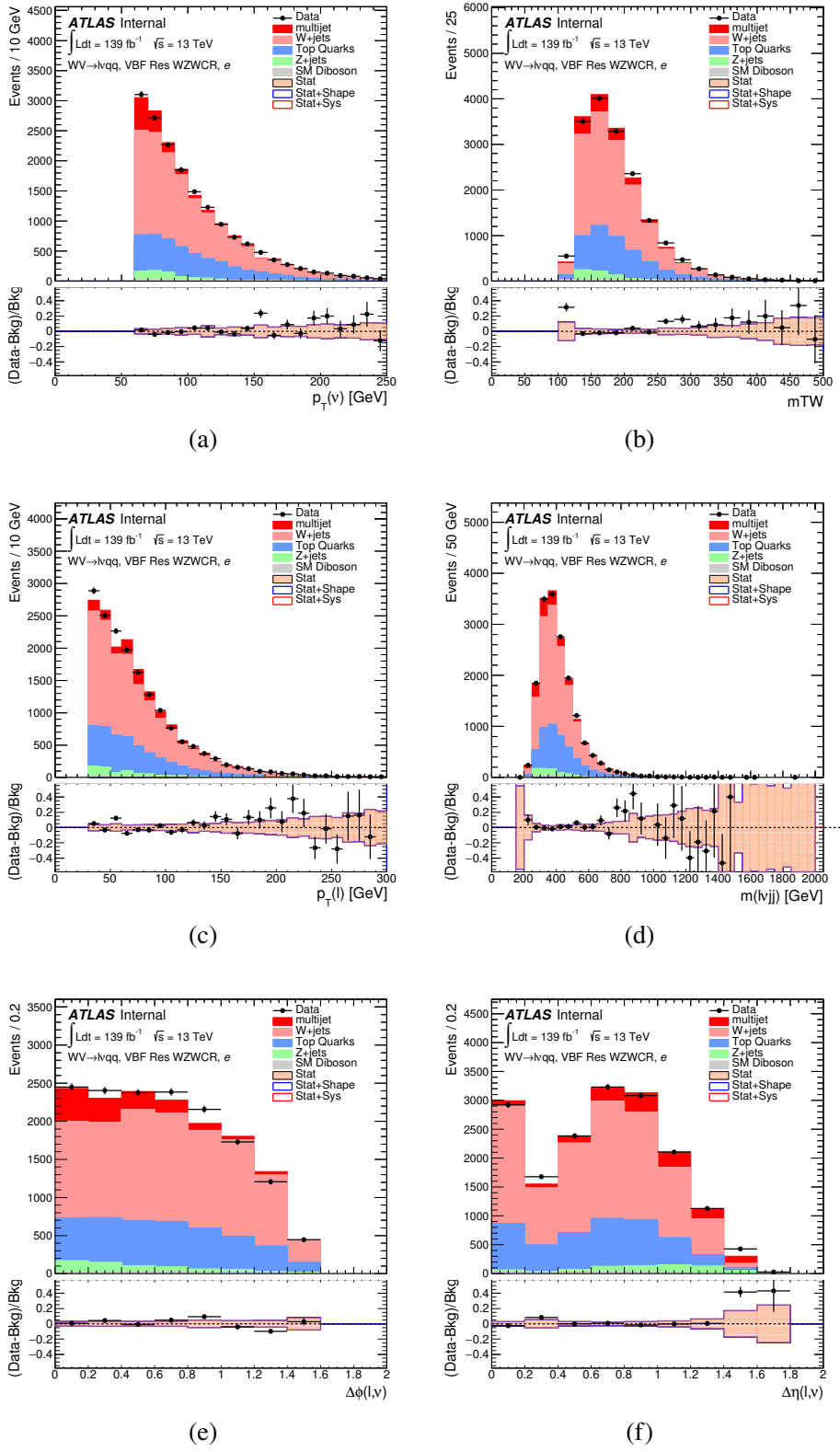


Figure 9.22: Postfit Data/MC comparison of distributions of E_T^{miss} , m_T^W , lepton and neutrino p_T , $m_{l\nu jj}$, lepton- ν angular distance in the VBF WW electron channel. The MJ template is obtained from the pre-MJ-fit.

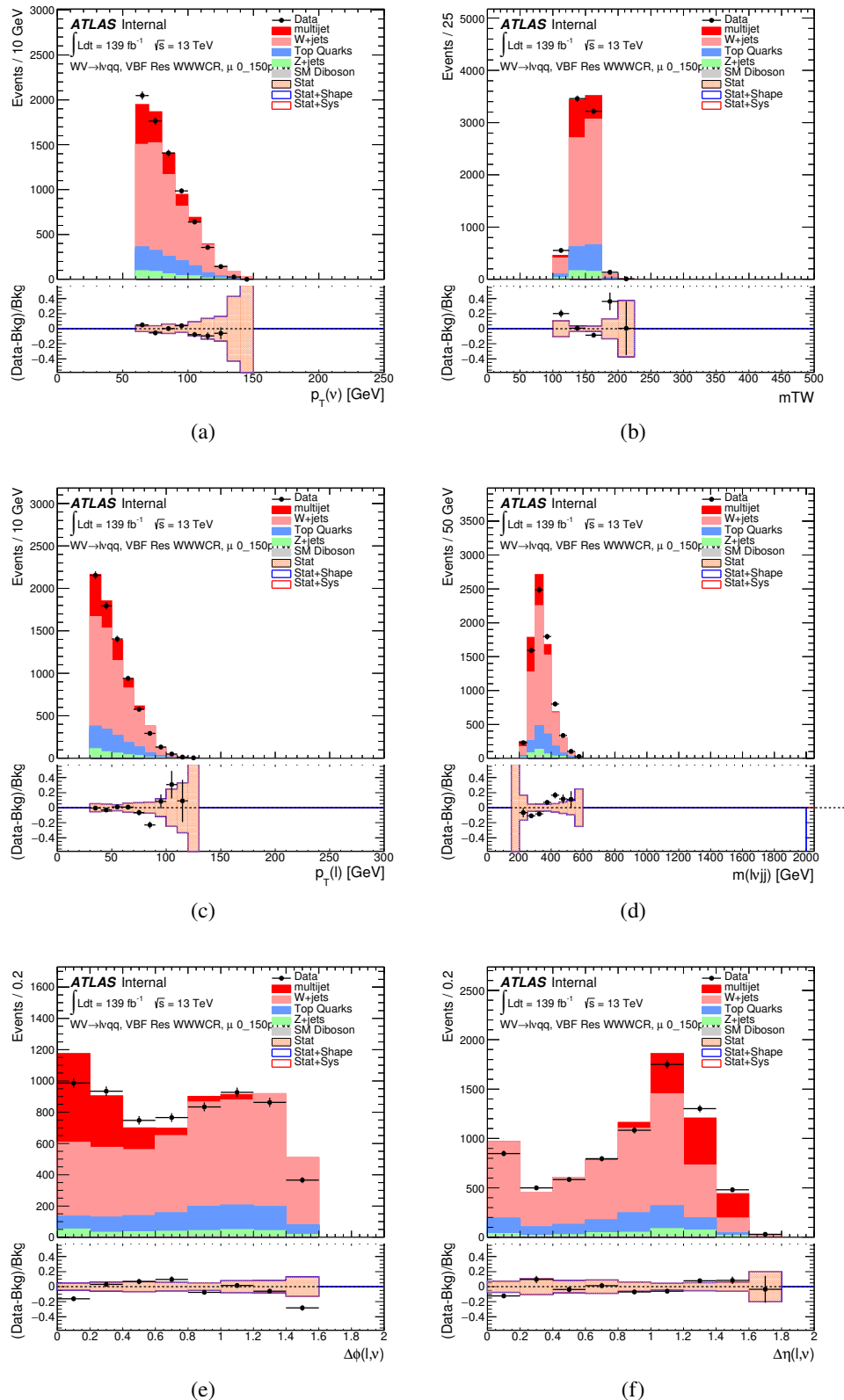


Figure 9.23: Postfit Data/MC comparison of distributions of E_T^{miss} , m_T^W , lepton and neutrino p_T , $m_{\ell\nu jj}$, lepton- ν angular distance in the VBF WW muon channel. The MJ template is obtained from the pre-MJ-fit.

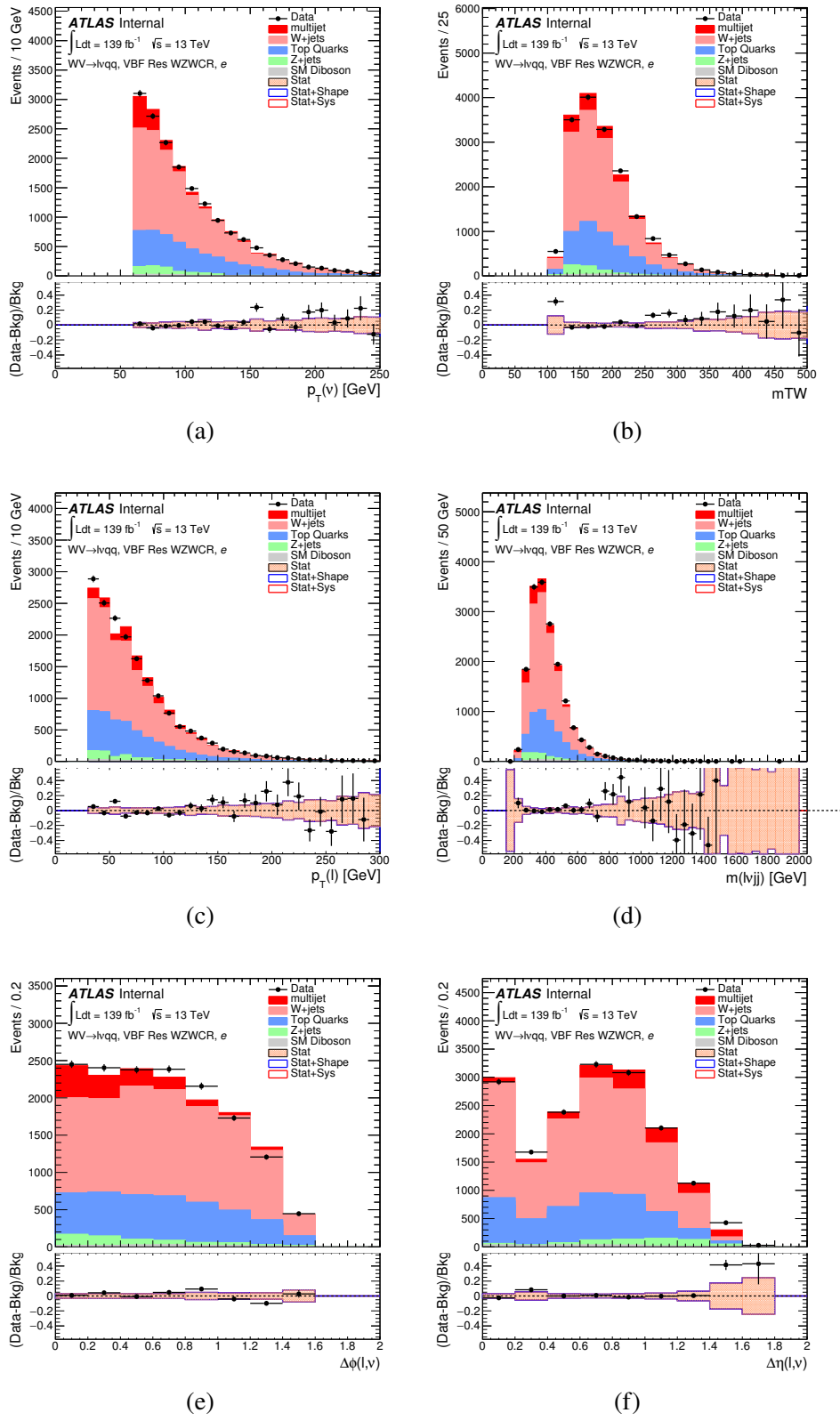


Figure 9.24: Postfit Data/MC comparison of distributions of E_T^{miss} , m_T^W , lepton and neutrino p_T , $m_{l\nu jj}$, lepton- ν angular distance in the VBF WZ electron channel. The MJ template is obtained from the pre-MJ-fit.

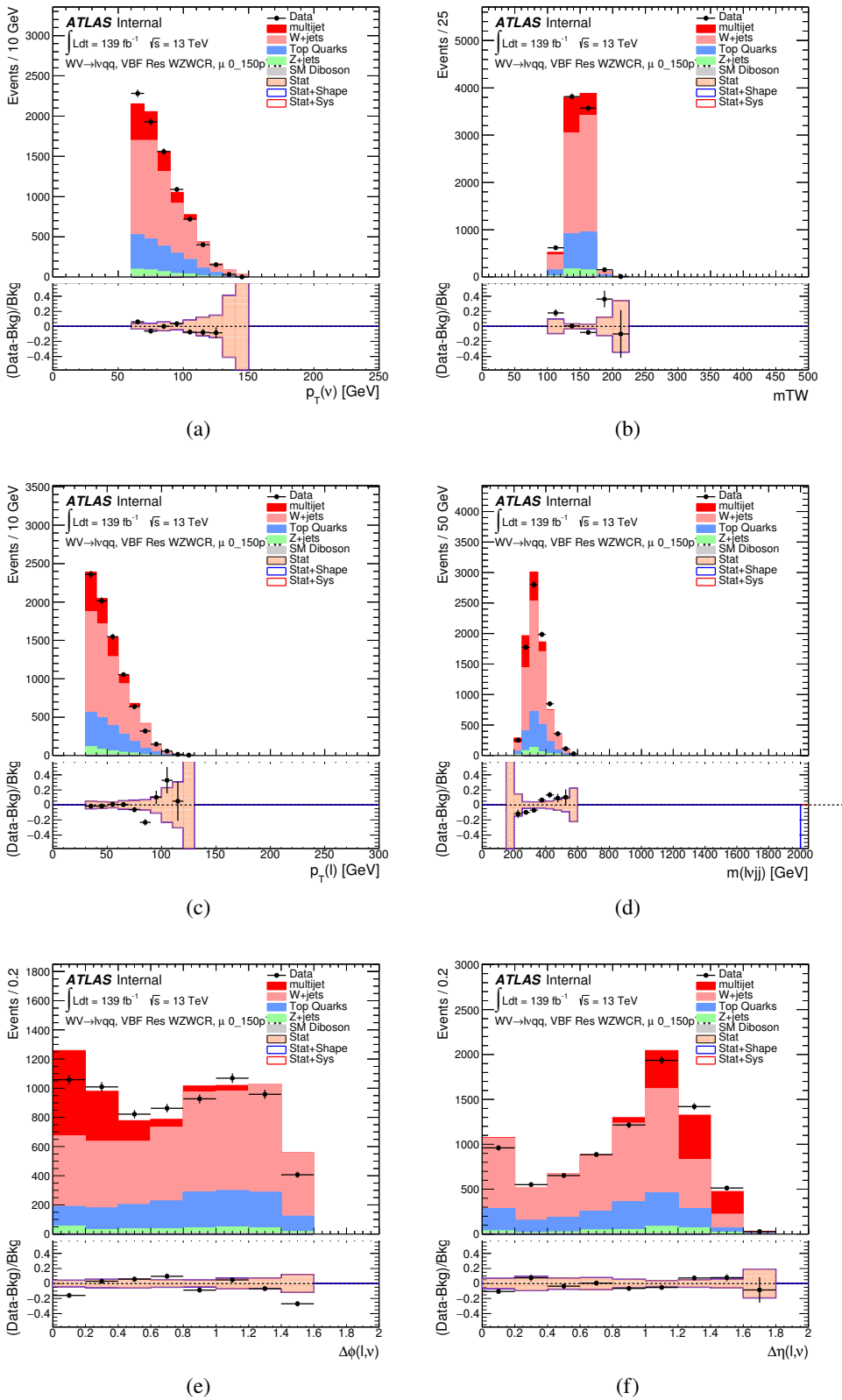


Figure 9.25: Postfit Data/MC comparison of distributions of E_T^{miss} , m_T^W , lepton and neutrino p_T , $m_{l\nu jj}$, lepton- ν angular distance in the VBF WZ muon channel. The MJ template is obtained from the pre-MJ-fit.

Full Run 2
ggF Res WWWCR

Sample	Yield	R.U.	SF
Top&W	645040 ± 1971.68	0.31%	0.998
Z&VV	24075.9		fixed
MJ_el	24156.3 ± 1224.62	5.06%	3.973
MJ_mu	35528.5 ± 923.94	2.60%	9.019

ggF Res WZ01bWCR

Sample	Yield	R.U.	SF
Top&W	644690 ± 1981.4	0.31%	0.997
Z&VV	24075.9		fixed
MJ_el	24366.5 ± 1232.69	5.05%	3.874
MJ_mu	35528.5 ± 921.27	2.58%	8.746

ggF Res WZ2bWCR

Sample	Yield	R.U.	SF
Top&W	71236.5 ± 688.74	0.97%	1.031
Z&VV	518.5		fixed
MJ_el	595.63 ± 449.34	75.44%	0.094
MJ_mu	1196.9 ± 222.13	18.56%	0.294

VBF Res WWWCR

Sample	Yield	R.U.	SF
Top&W	19032.3 ± 364.43	1.91%	0.928
Z&VV	1091.63		fixed
MJ_el	1425.73 ± 214.42	15.03%	0.235
MJ_mu	1281.36 ± 157.21	11.83%	0.314

VBF Res WZWCR

Sample	Yield	R.U.	SF
Top&W	21341.8 ± 392.21	1.84%	0.942
Z&VV	1111.75		fixed
MJ_el	1413.76 ± 230.36	16.29%	0.225
MJ_mu	1281.36 ± 157.21	12.27%	0.314

Table 9.5: Fit validation result in WCRs for 2015+16 data. The fit is done in various WCRs, in order to obtain the corresponding scale factors for MJ templates: ggF resolved WCR for the $WW \rightarrow lvqq$ selection, ggF resolved untagged WCR for the $WZ \rightarrow lvqq$ selection, ggF resolved tagged WCR for the $WZ \rightarrow lvqq$ selection, VBF resolved WCR for the $WW \rightarrow lvqq$ selection, and VBF resolved WCR for the $WZ \rightarrow lvqq$ selection. Post-fit event yields for electroweak processes and MJ contributions are shown. The SF column shows the corresponding normalization scale factors for electroweak processes from the fit. R.U. stands for relative uncertainty.

1069 **Chapter 10**

1070 **Systematic Uncertainties**

1071 This section describes the sources of systematic uncertainties of the m_{WV} dis-
1072 tribution. These uncertainties are divided into experimental and modeling uncer-
1073 tainties. Each systematic uncertainty is used as a nuisance parameter in the final
1074 likelihood fit.

1075 **10.1 Experimental Systematics**

1076 The uncertainty on the integrated luminosity of the dataset used is 1.7% and
1077 a systematic in the final fit. This uncertainty was calculated using $x - y$ beam
1078 separation scans [natasha ref P55].

1079 An additional source of systematic uncertainty is assigned to the pileup mod-
1080eling in MC samples. This ensures simulated detector response and particle re-
1081construction conditions are as similar as possible. The distribution of the average
1082 number of interactions per bunch crossing applied to simulation is called the μ pro-
1083file. The pileup modeling uncertainty is accounted for by re-weighting simulated
1084events so the average number of interactions per bunch crossing varies within its
1085uncertainty due to systematics from vertex reconstruction [ref ATL-COM-SOFT-

1086 2015-119]. The associated re-weighting factors are propagated through the entire
1087 analysis chain to construct a systematic uncertainty on m_{VV} .

1088 The single-lepton and E_T^{miss} triggers used are not fully efficient, so scale factors
1089 are applied to simulation to more accurately model the data. These scale factors
1090 are given by the ratio of the distribution of offline objects before trigger selection
1091 and after trigger selection. The associated uncertainty on these scale factors are
1092 used in the final fit.

1093 Uncertainties on small-R jet energy scale and resolution are measured in-situ
1094 by calculating the response between data and simulation. This analysis uses a
1095 reduced set of JES and JER uncertainties (totaling 30 and 8 systematics, re-
1096 spectively). These reduced sets of systematics are calculated using a principal
1097 component analysis, yield largely uncorrelated independent systematics. These
1098 uncertainties on JES and JER account for the dependence on p_T , η , μ , flavor re-
1099 sponse and global sequential corrections. Systematic uncertainties associated with
1100 b -tagging are also considered. These systematics are evaluated as uncertainties on
1101 the scale factor which account for the difference in b -tagging efficiencies in data
1102 and MC, and the flavor dependence (between b, c, and light jets).

1103 The uncertainty on the p_T scale of the large-R jets is determined by comparing
1104 the jet's p_T^{calo} to p_T^{track} in di-jet simulation and data. In addition to this uncertain-
1105 ties from tracking, modeling (Pythia vs Herwig), and statistical constraints are
1106 also calculated. The large-R jet p_T resolution is given by smearing the jet p_T with
1107 a Gaussian with a 2% width.

1108 The W/Z tagging efficiency SF is estimated by comparing the tagging effi-
1109 ciency in simulation with that in data for four regions of the W/Z tagger (D_2 fail,
1110 m_J fail; D_2 pass, m_J fail; D_2 fail, m_J pass; D_2 pass, m_J pass). (Additionally,
1111 separate scale factors are determined for events with large-R jets from W bosons

and top backgrounds.) A simultaneous template fit is used to fit the signal jets (jets initiated by W/Z bosons or top quarks) and background jets (all other jets from the simulated backgrounds) to the data in the four regions. using the m_J distributions. The SF for a given region is then given by:

$$SF = \frac{\epsilon_{data} = \frac{N_{fitted-signals}^{region}}{N_{all-regions}^{fitted-signals}}}{\epsilon_{MC} = \frac{N_{signal}^{region}}{N_{signal}^{all-regions}}} \quad (10.1)$$

The effects of experimental and theoretical uncertainties on the efficiency scale factor are determined by taking the ratio of efficiencies in data and simulation. By taking this ratio the uncertainties not arising for jet mass and D_2 cancel.

Lepton identification, reconstruction, isolation systematic uncertainties are determined by reconstructing the Z mass peak with a tag and probe method. The lepton energy and momentum scales are also measured with the Z mass peak.

As E_T^{miss} is calculated using all the physics objects in the event, all those objects associated errors result in an uncertainty on E_T^{miss} . Additionally, the unassociated tracks used to construct E_T^{miss} contribute to the uncertainty on E_T^{miss} .

10.2 Theory Systematics

Theoretical uncertainties for signal and background processes arise from uncertainties in the parameters used in Monte Carlo simulation. In particular for the $t\bar{t}$, $W/Z+jets$, diboson backgrounds and signal samples, the QCD scale, PDF, generator and hadronization uncertainties were evaluated. To assess the QCD scale uncertainty the renormalization and factorization scales were scaled up and down by a factor of two at the event generation stage of sample production. Uncertainties due to the choice of the parton distribution functions were evaluated by

1133 re-weighting samples from the nominal PDF to a set of error PDFs which account
1134 for the uncertainty of the fits used to produce the PDF set. In addition to this,
1135 samples are re-weighted to different PDF sets to account for the arbitrariness of
1136 the PDF choice. The difference between the m_{WV} distributions using different
1137 event generators is assessed by comparing samples generated with different gen-
1138 erators. Similarly, the uncertainty in hadronization models is accounted for by
1139 comparing samples created using different hadronization models (e.g. $t\bar{t}$ Powheg
1140 is compared to AMC@NLO, $W + jets$ compares Sherpa and MadGraph+Pythia
1141 samples). Figures 10.2 - 10.8 show the impact of these uncertainties on the $t\bar{t}$ and
1142 $W/Z + jets$ backgrounds. Additionally, contributions to the diboson background
1143 for the VBF analysis were found to be small and were accounted for by including
1144 a 5(10)% systematic in the diboson normalization in the final fit.

1145 The normalization of the $t\bar{t}$ and $W+jets$ processes impact the multijet tem-
1146 plate shape. The impact of these normalizations was assessed by including a
1147 shape systematic on the multijet background from varying the $t\bar{t}$ and $W+jets$
1148 normalization factors.

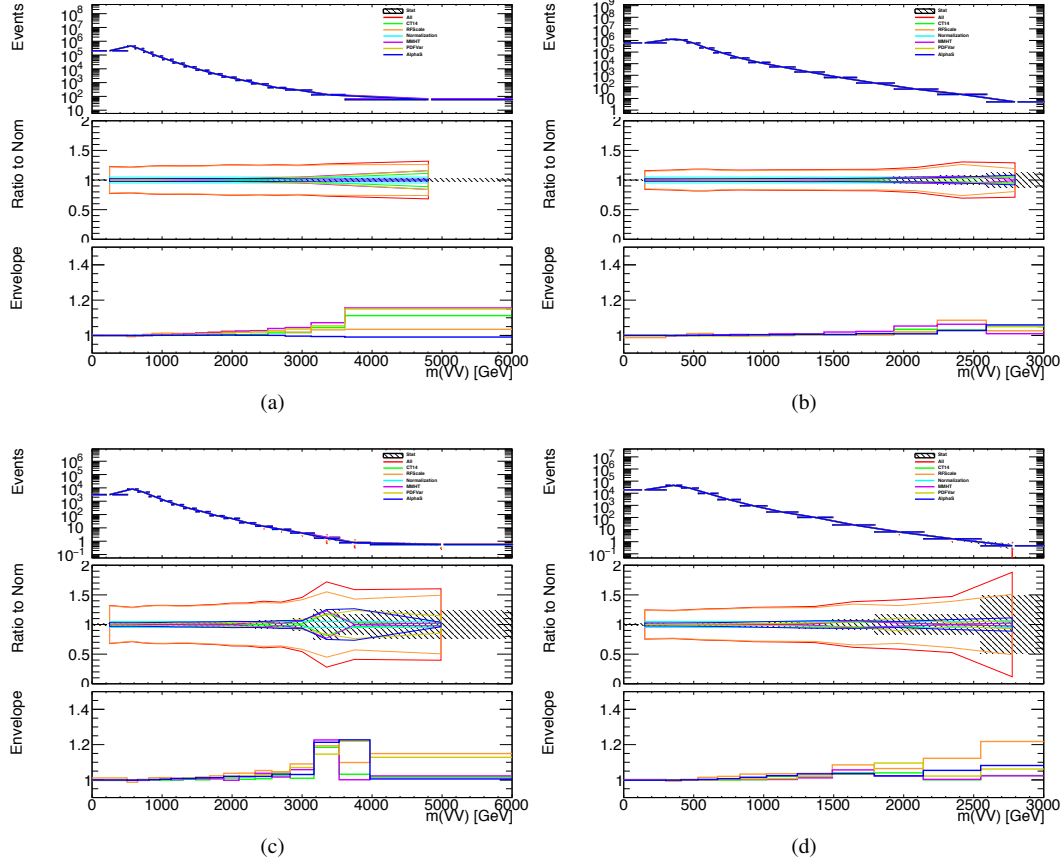


Figure 10.1: The $W/Z + \text{jet}$ systematics for the a) Merged ggF, b) Resolved ggF, c) Merged VBF, and d) Resolved VBF regions. The top subplot shows the nominal and variation distributions/bands, the middle shows the ratio of the two, and the final shows just the shape of the envelope (the final uncertainty).

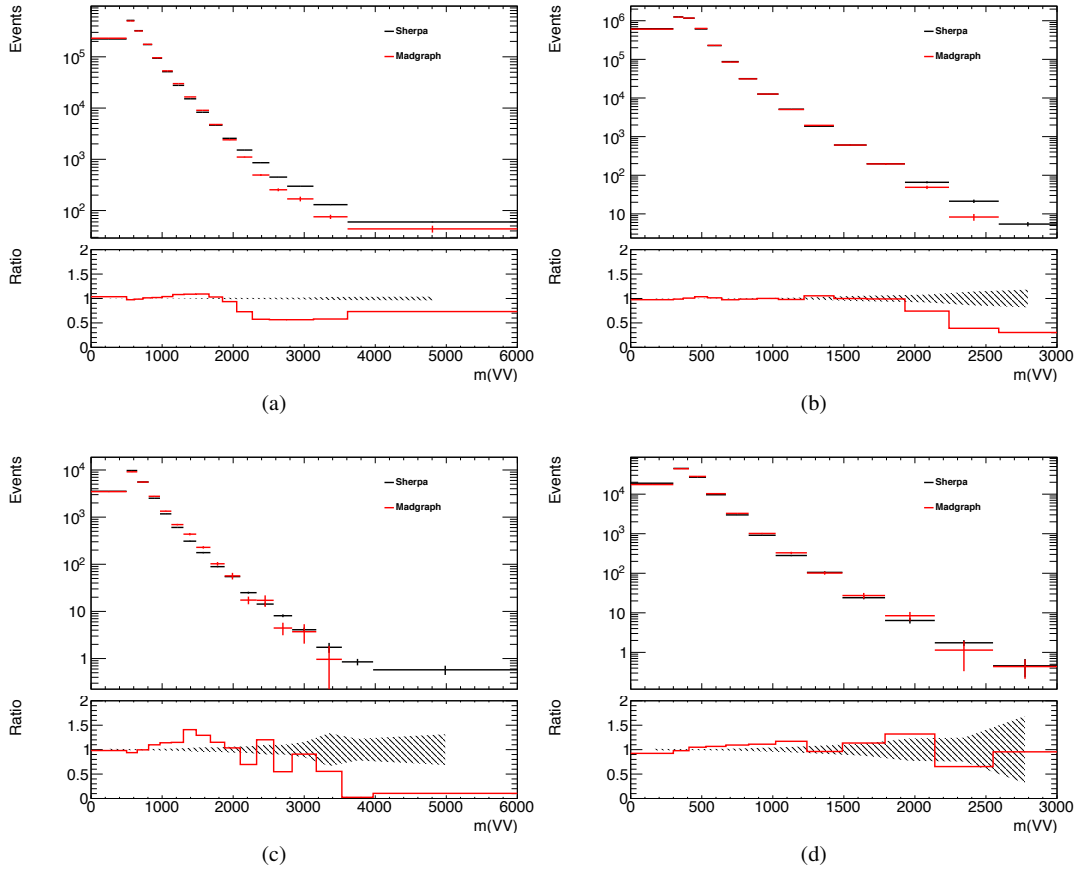


Figure 10.2: The two-point generator comparison between Sherpa and MadGraph for the $W/Z + \text{jet}$ samples in the a) Merged ggF, b) Resolved ggF, c) Merged VBF, and d) Resolved VBF regions. The normalization of the Madgraph sample is set to the Sherpa value to consider only shape effects. The bottom inset shows the ratio of the two.

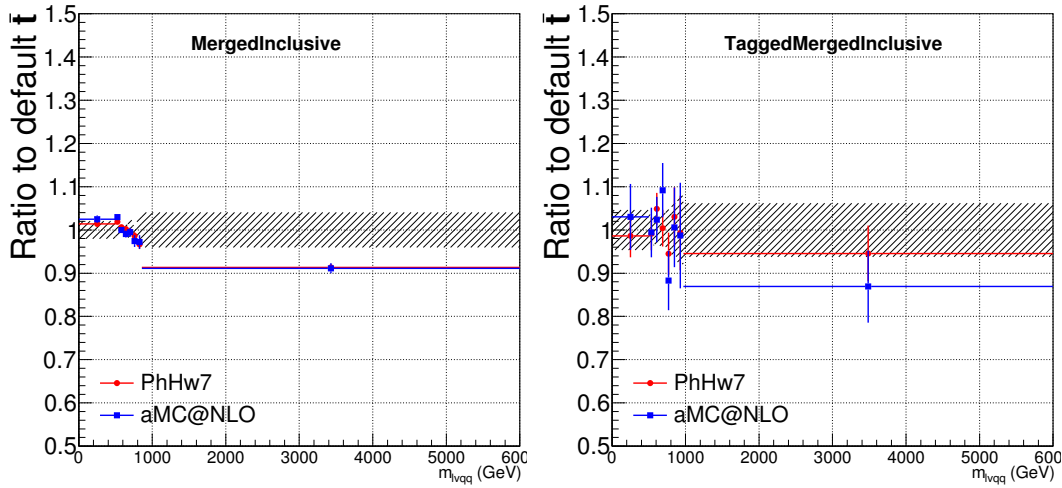


Figure 10.3: Ratio between the variations of generator (red) and hadronization (blue) variations for the Merged regime for $t\bar{t}$ sample.

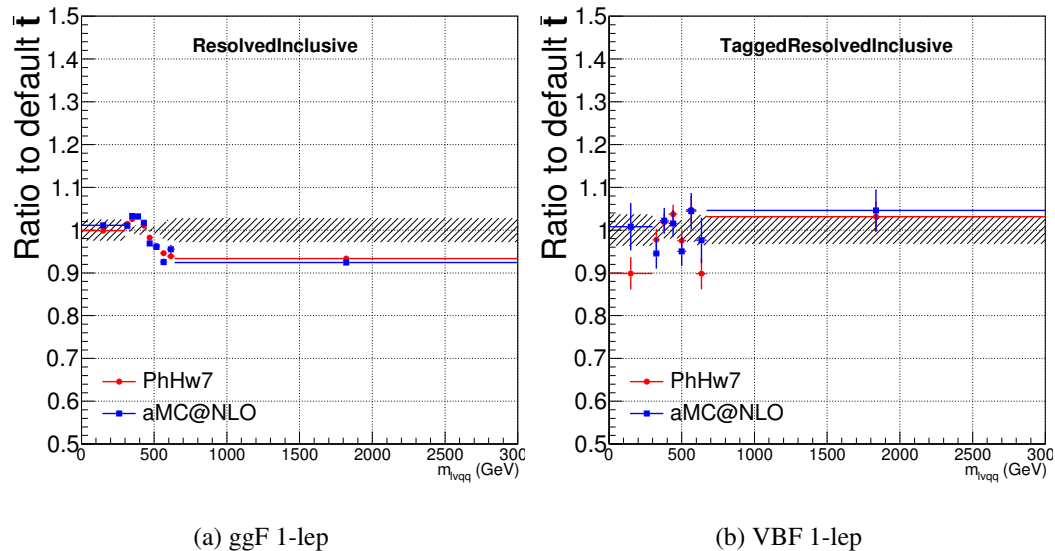


Figure 10.4: Ratio between the variations of generator (red) and hadronization (blue) variations for the Resolved regime for $t\bar{t}$ sample.

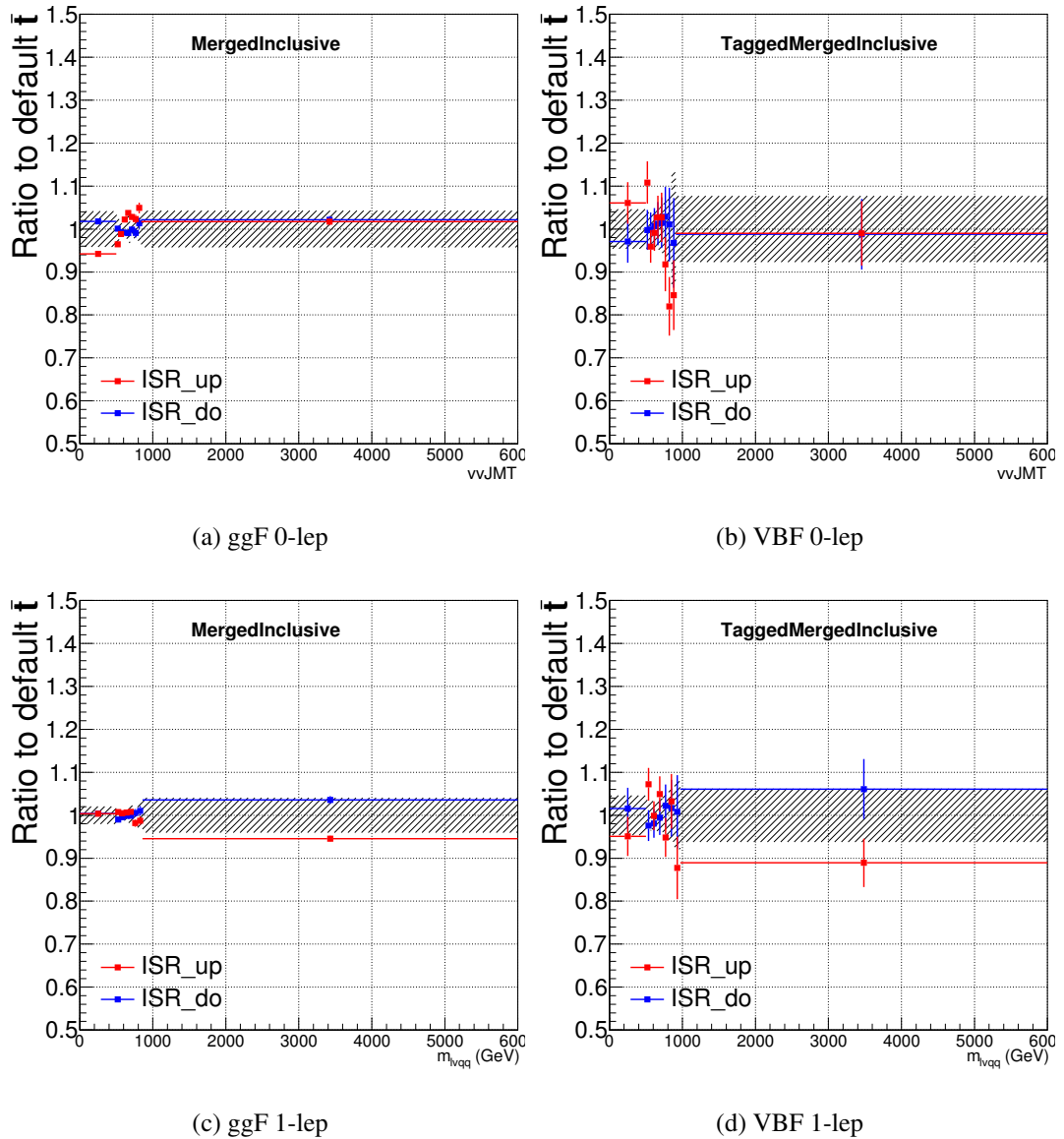


Figure 10.5: Ratio between the variations of ISR up (red) and down (blue) variations for the Merged regime for $t\bar{t}$ sample.

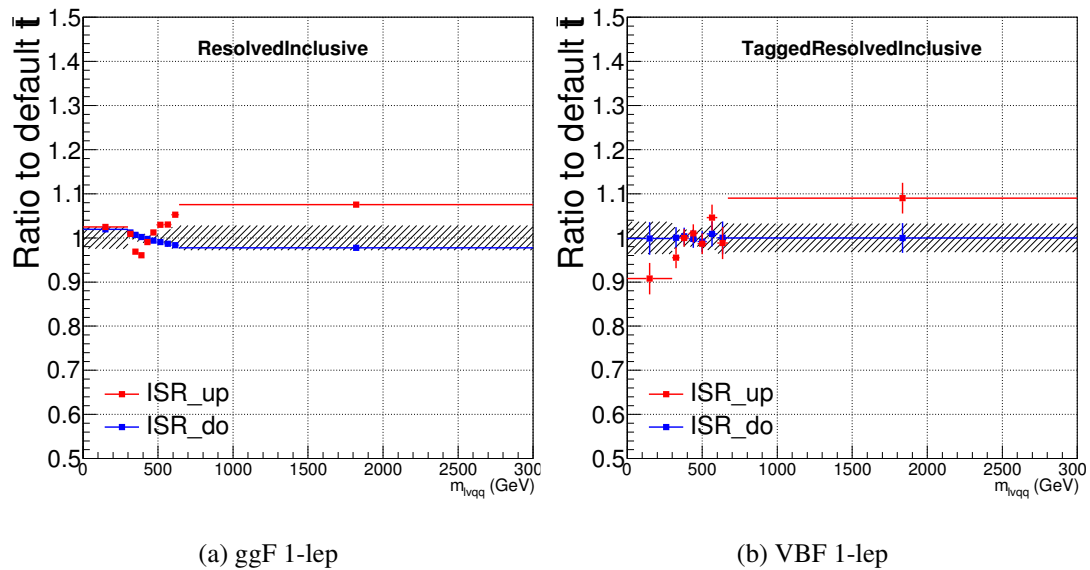


Figure 10.6: Ratio between the variations of ISR up (red) and down (blue) variations for the Resolved regime for $t\bar{t}$ sample.

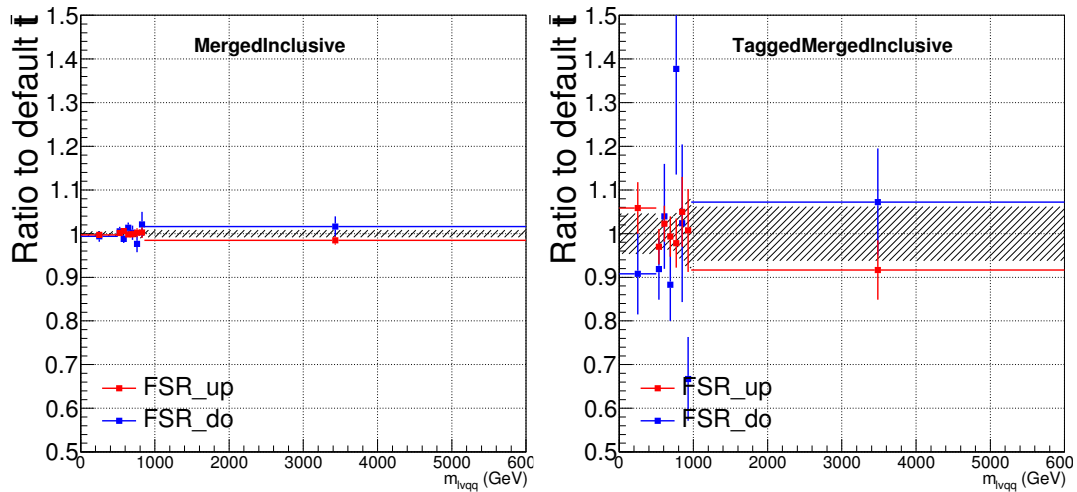


Figure 10.7: Ratio between the variations of FSR up (red) and down (blue) variations for the Merged regime for $t\bar{t}$ sample.

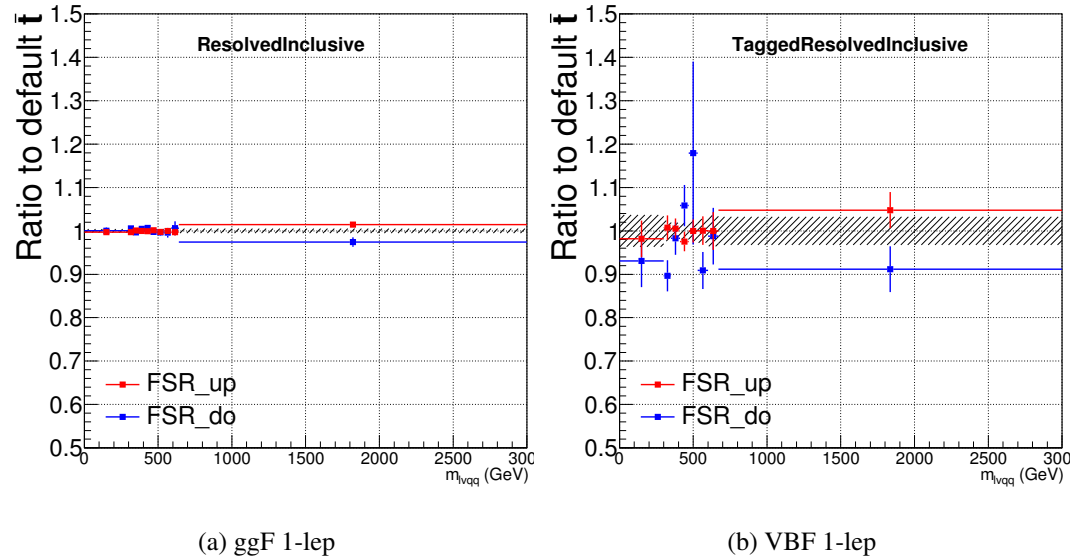


Figure 10.8: Ratio between the variations of FSR up (red) and down (blue) variations for the Resolved regime for $t\bar{t}$ sample.

₁₁₄₉ **Chapter 11**

₁₁₅₀ **Statistical Analysis**

₁₁₅₁ To determine the compatibility of the data collected with the proposed reso-
₁₁₅₂ nances a statistical procedure based on a likelihood function is used. A discovery
₁₁₅₃ test is used to measure the compatibility of the observed data with the back-
₁₁₅₄ ground only hypothesis. If the observed data is sufficiently incompatible with the
₁₁₅₅ background only hypothesis, this could indicate a discovery. In the absence of
₁₁₅₆ discovery, upper limits on the signal strength parameter, μ , are assessed using the
₁₁₅₇ CLs method.

₁₁₅₈ **11.1 Likelihood Function Definition**

₁₁₅₉ The likelihood function is product of Poisson probabilities for all analysis bins
₁₁₆₀ and systematic constraints:

$$\mathcal{L}(\mu, \boldsymbol{\theta}) = \prod_c \prod_i \frac{(\mu s_{ci}(\boldsymbol{\theta}) + b_{ci}(\boldsymbol{\theta}))^{n_{ci}}}{n_{ci}!} e^{-(\mu s_{ci}(\boldsymbol{\theta}) + b_{ci}(\boldsymbol{\theta}))} \prod_k (\theta'_k | \theta_k) \quad (11.1)$$

₁₁₆₁ Here c are the analysis channels considered and i runs over all the $m_{\ell\nu qq}$ bins

1162 used in the fit. The signal strength parameter, μ , multiplies the expected signal
1163 yield in each analysis bin, s_{ci} . The background content for channel c and bin i is
1164 given by b_{ci} . The dependence of signal and background predictions on system-
1165 atic uncertainties is described by the aforementioned set of nuisance parameters
1166 $\boldsymbol{\theta}$, which are parameterized by Gaussian or log-normal priors denoted here as
1167 θ_k . Statistical uncertainties of the simulated bin contents are also included as
1168 systematic uncertainties. Most systematics are correlated among all the analysis
1169 regions and considered to be independent from each other. The validity of this
1170 assumption is checked by evaluating the covariance of nuisance parameters.

1171 11.2 Fit Configuration

1172 The binning of $m_{\ell\nu qq}$ in signal regions for likelihood fit is determined by the
1173 statistical uncertainty of signal mass width. For each signal mass point, the signal
1174 mass resolution is given by the fitted Gaussian width of the $m_{\ell\nu qq}$. The fitted
1175 signal widths are then fit to a line to give a parameterized signal mass width, as
1176 shown in Figures 11.1 and 11.2. Bin widths are set first to this parameterized
1177 signal mass resolution. Then if the statistical uncertainty of the data or simulated
1178 background is more than 50%, bins are merged until the statistical uncertainty is
1179 less than 50%. All control regions contain only a single bin.

1180 For this analysis, each signal model is fit in the Merged and Resolved chan-
1181 nels for the relevant signal production mode simultaneously. The $W + \text{jets}$ and $t\bar{t}$
1182 normalizations are given by the best fit values in the overall fit and these fitted
1183 normalizations are then applied to those backgrounds in the SRs.

1184 Systematics may be affected by low statistics, leading to unsmooth m_{VV} dis-
1185 tributions with unphysically large fluctuations. This can lead to artificial pulls
1186 and constraints in the fit. To remove such issues a multi-step smoothing pro-

1187 cedure is applied to all systematic variation distributions in all regions. First,
1188 distributions are rebinned until the statistical error per bin is at least 5%. Next
1189 all local extrema are identified. The bins around smallest extrema are iteratively
1190 merged until only four local extrema remain. Then distributions are rebinned so
1191 that statistical uncertainties in each bin are $< 5\%$.

1192 For some systematics, up and down variations may be in the same direction
1193 with respect to the nominal distributions. This causes the variations to not cover
1194 the nominal choice, and the interpretation of the confidence interval is skewed as
1195 the nominal distribution should be bracketed by the up and down variations. This
1196 asymmetry may also lead to unconstrained systematics in the fit. To handle such
1197 asymmetric systematics, if the up and down variation for a given systematic are in
1198 the same direction for at least three m_{VV} bins the variation is averaged for those
1199 bins. The averaging procedure replaces bin-by-bin the up and down variation bins
1200 by $b_{\pm}^{new} = b_{nom} \pm \frac{|b_+ - b_-|}{2}$, where b_{nom} is the nominal bin content and b_{\pm} are the
1201 original up and down variation bin content. The same procedure is also applied to
1202 any variations where the integral of the difference between the up/down variation
1203 and the nominal distribution is twice that of the other down/up variation, further
1204 ensuring variations are symmetric around the nominal distribution.

1205 Finally, systematics that have a negligible effect on the m_{VV} distribution are
1206 not considered in the fit. Shape systematics where no bin in the variational dis-
1207 tribution deviates more than 1% from the nominal distribution (after normalizing
1208 all histograms to the nominal) are not included in the fit. Also, statistical bin
1209 uncertainties $< 1\%$ are ignored.

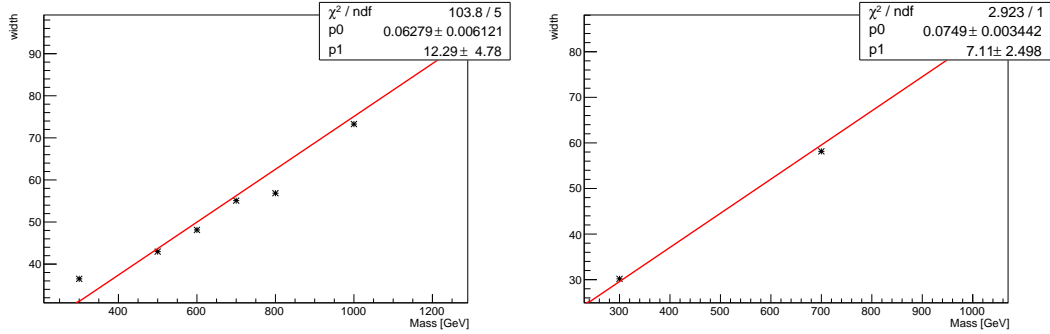


Figure 11.1: The HVT signal mass resolution as a function of mass fit with a straight line in the Resolved ggF region (left) and VBF (right) region.

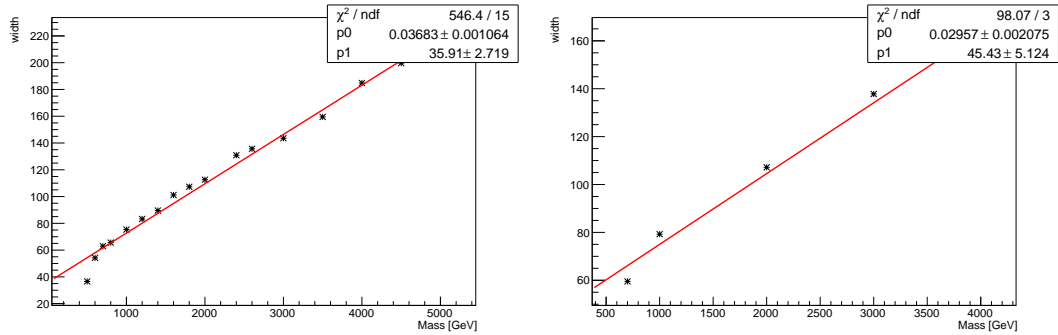


Figure 11.2: The HVT signal mass resolution as a function of mass fit with a straight line in the Merged ggF region (left) and VBF (right) region.

1210 11.3 Best Fit μ

1211 The best fit signal strength parameter is denoted by $\hat{\mu}$ and calculated by
 1212 maximizing the likelihood function with respect to all systematics and μ . The
 1213 corresponding set of systematics that maximize the likelihood are given by $\hat{\mu}$.
 1214 The first term in the likelihood is maximized when the expected number of signal
 1215 and background events is equal to the number of events in data ($n_{ci} = \mu s_{ci} +$
 1216 b_{ci}). Thus, by maximizing the likelihood, the fit determines values of μ and θ
 1217 that give the best agreement between expected and measured event yields. The

1218 second term in the likelihood is a penalty term which decreases the likelihood
1219 when systematics are shifted from their nominal values. This prevents the fit
1220 from profiling systematics in unphysical ways to maximize the likelihood. The
1221 uncertainty on μ is calculated by varying μ up and down until the natural log of
1222 the likelihood function shifts by one-half.

1223 11.4 Discovery Test

1224 To determine if the observed dataset is consistent with tested signal model a
1225 likelihood ratio is constructed:

$$\lambda(\mu) = \frac{\mathcal{L}(\mu, \hat{\theta}_\mu)}{\mathcal{L}(\hat{\mu}, \hat{\theta})} \quad (11.2)$$

1226 The denominator in this equation is the maximized value of \mathcal{L} over all system-
1227 atics and μ . The numerator is the maximized likelihood over all systematics for
1228 a given μ value, where the maximized systematics are given by $\hat{\mu}_\mu$. To test for
1229 the existence of signal the observed dataset the null hypothesis (H_0) is defined as
1230 the background only hypothesis and the alternate hypothesis includes signal and
1231 background (H_1). This test quantifies the compatibility of observed data with
1232 H_0 by calculating a p-value representing the probability of observing data as dis-
1233 crepant or more than the observed data under the H_0 . The test statistic used to
1234 calculate this p-value is given by (r_0):

$$r_0 = \begin{cases} -2 \ln \lambda(0), \hat{\mu} > 0 \\ +2 \ln \lambda(0), \hat{\mu} < 0 \end{cases} \quad (11.3)$$

1235 The expected distribution of the the test statistic under H_0 ($f(r_0|0)$) is used to
1236 calculate the p-value:

$$p_0 = \int_{r_0, obs}^{\infty} f(r_0 | 0) dr_0 \quad (11.4)$$

1237 Small p-values indicate the observed data is poorly described by H_0 . This
 1238 equivalent Z-score of a given p-value is usually used to further quantify the agree-
 1239 ment between the observed data and H_0 . The Z-score is given by the number of
 1240 standard deviations away from the mean of a Gaussian distribution, the integral
 1241 of the upper tail of the distribution would equal the p-value. Mathematically:

$$Z = \Phi^{-1}(1 - p_0) \quad (11.5)$$

1242 where Φ is the Gaussian cumulative distribution function. The statistical
 1243 significance of these tests are expressed as the Z -score. In particle physics, 3σ is
 1244 considered evidence for new phenomena and 5σ is the threshold for discovery.

1245 11.5 Exclusion Limits

1246 In the absence of discovery, upper limits on the signal strength, μ are set using
 1247 the CLs method [cite P60]. The test statistic for this test, q_μ , is constructed as:

$$\tilde{\lambda}_\mu = \begin{cases} \frac{\mathcal{L}(\mu, \hat{\theta}_\mu)}{\mathcal{L}(\hat{\mu}, \hat{\theta})}, \hat{\mu} > 0 \\ \frac{\mathcal{L}(\mu, \hat{\theta}_\mu)}{\mathcal{L}(0, \hat{\theta}_0)}, \hat{\mu} < 0 \end{cases} \quad (11.6)$$

$$\tilde{q}_\mu = \begin{cases} -2 \ln \tilde{\lambda}(\mu), \hat{\mu} < \mu \\ +2 \ln \tilde{\lambda}(\mu), \hat{\mu} > \mu \end{cases} \quad (11.7)$$

1248 As defined, larger values of q_μ correspond to increasing incompatibility between
 1249 the observed data and the background + signal hypothesis. The observed value
 1250 of the test statistic, $q_{\mu, obs}$, is then compared to its expected distribution, f , to

1251 calculate p-values to assess the likelihood of the background+signal hypothesis.

1252 Using these distributions, CL_s values are computed as:

$$1253 \quad CL_{s+b} = \int_{q_{\mu,obs}}^{\infty} f(q_{\mu}|\mu) dq_{\mu} \quad (11.8)$$

$$1254 \quad CL_b = \int_{q_0^{obs}}^{\infty} f(q_{\mu}|\mu = 0) dq_{\mu} \quad (11.9)$$

$$1255 \quad CL_s = \frac{CL_{s+b}}{CL_b} \quad (11.10)$$

1255 CL_{s+b} is the p-value for the signal + background hypothesis and CL_b is the
1256 p-value for the background only hypothesis. The CL_s value is interpreted as
1257 the probability to observe the background + signal hypothesis normalized to the
1258 probability of background-only hypothesis. Normalizing by CL_b prevents setting
1259 artificially strong exclusion limits due to downward fluctuations in data.

1260 For a given signal hypothesis, μ values are scanned simultaneously over all
1261 m_{WV} bins to find the μ value that yields $CL_s=0.05$, meaning the likelihood of
1262 finding data more incompatible with the signal+background hypothesis (relative
1263 to the background only hypothesis) is 5%. The 95% upper limit on the cross
1264 section is then calculated as the product of the μ value found, branching ratio,
1265 and theory cross section.

₁₂₆₆ **Chapter 12**

₁₂₆₇ **Results**

₁₂₆₈ **12.1 Expected and Measured Yields**

₁₂₆₉ The yield tables for the four analysis regions are shown in Tables ?? - ??.

₁₂₇₀ The fitted background normalizations are shown in Tables ??-??. The control

₁₂₇₁ region $m_{\ell\nu qq}$ distributions are shown in Figures 12.1 - 12.4. The signal region

₁₂₇₂ $m_{\ell\nu qq}$ distributions are shown in Figures 12.5 - ??.

	HP WCR	LP WCR	Resolved WCR
Electron Multi-jet	-	-	16507.83 ± 2314.87
Muon Multi-jet	-	-	19977.12 ± 2816.06
Diboson	1833.41 ± 177.78	3323.93 ± 320.92	9147.67 ± 961.63
Single-top	2160.62 ± 402.34	3551.09 ± 660.00	20058.36 ± 3817.26
$t\bar{t}$	15518.86 ± 338.22	24069.54 ± 453.15	138866.23 ± 1989.71
$W+jets$	40141.57 ± 357.79	88113.06 ± 487.87	673200.38 ± 4120.53
$Z+jets$	778.83 ± 78.93	1765.54 ± 179.10	16570.50 ± 1672.71
Total	60433.29 ± 664.92	120823.16 ± 1006.99	894328.12 ± 7247.12
Data	60264.00	120852.00	895362.00
	HP TCR	LP TCR	Resolved TCR
Electron Multi-jet	-	-	-
Muon Multi-jet	-	-	-
Diboson	421.11 ± 37.98	550.44 ± 53.10	996.87 ± 119.63
Single-top	4691.44 ± 846.11	3466.26 ± 631.03	16848.71 ± 3258.26
$t\bar{t}$	38945.18 ± 848.77	33836.95 ± 637.04	224226.14 ± 3212.76
$W+jets$	2258.34 ± 20.13	6564.78 ± 36.35	23466.41 ± 143.63
$Z+jets$	66.35 ± 6.72	213.26 ± 21.63	846.66 ± 85.47
Total	46382.43 ± 1199.25	44631.70 ± 899.23	266384.78 ± 4580.43
Data	46354.00	44629.00	266443.00
	WW SR	LP SR	Resolved 1-lepton SR
Electron Multi-jet	-	-	10788.40 ± 1512.85
Muon Multi-jet	-	-	15759.50 ± 2221.53
Diboson	4990.30 ± 376.50	3901.07 ± 313.22	16971.29 ± 1523.77
Single-top	3117.71 ± 565.07	2176.46 ± 400.52	20422.85 ± 3731.94
$t\bar{t}$	13785.77 ± 302.14	11005.12 ± 207.41	126965.25 ± 1819.66
$W+jets$	24718.56 ± 223.72	60080.66 ± 333.12	444133.56 ± 2719.02
$Z+jets$	478.18 ± 48.46	1226.69 ± 124.44	11686.32 ± 1179.69
Total	47090.52 ± 777.65	78389.98 ± 654.22	646727.19 ± 5963.98
Data	47330.00	78380.00	645610.00

Table 12.1: Expected and Measured for DY WW $W+jets$, $t\bar{t}$ control regions and signal regions.

	HP Untagged WCR	LP Untagged WCR	Resolved Untagged WCR
Electron Multi-jet	-	-	15080.03 ± 2277.99
Muon Multi-jet	-	-	27347.10 ± 2950.07
Diboson	1508.48 ± 154.20	2758.24 ± 284.50	9038.55 ± 728.69
Single-top	1756.59 ± 306.69	2913.18 ± 515.93	20511.74 ± 3523.47
$t\bar{t}$	13134.00 ± 238.30	21815.37 ± 334.98	140157.77 ± 2636.96
$W+jets$	40654.84 ± 333.65	87657.76 ± 501.96	665909.12 ± 4420.62
$Z+jets$	768.72 ± 77.97	1759.87 ± 178.96	16512.46 ± 1673.23
Total	57822.63 ± 540.40	116904.42 ± 862.16	894556.75 ± 7492.20
Data	57699.00	117306.00	895362.00
	HP Tagged WCR	LP Tagged WCR	Resolved Tagged WCR
Electron Multi-jet	-	-	384.58 ± 57.11
Muon Multi-jet	-	-	602.93 ± 190.12
Diboson	30.22 ± 4.69	48.95 ± 7.16	264.64 ± 28.24
Single-top	308.44 ± 56.19	371.59 ± 69.43	5752.39 ± 1029.97
$t\bar{t}$	1683.82 ± 48.73	2041.48 ± 70.00	58431.49 ± 614.30
$W+jets$	583.55 ± 75.37	1109.45 ± 85.78	11891.68 ± 903.01
$Z+jets$	13.19 ± 1.34	23.06 ± 2.34	324.74 ± 32.85
Total	2619.22 ± 106.00	3594.53 ± 130.90	77652.45 ± 1514.89
Data	2565.00	3546.00	77973.00
	HP Untagged TCR	LP Untagged TCR	Resolved Untagged TCR
Electron Multi-jet	-	-	-
Muon Multi-jet	-	-	-
Diboson	289.45 ± 28.45	346.78 ± 35.85	650.85 ± 65.56
Single-top	3107.99 ± 538.03	2250.64 ± 385.41	9606.87 ± 1698.22
$t\bar{t}$	30992.40 ± 562.33	26954.21 ± 413.89	91893.59 ± 1728.91
$W+jets$	2236.29 ± 18.35	4874.03 ± 27.91	16122.97 ± 107.03
$Z+jets$	71.54 ± 7.26	155.50 ± 15.81	577.71 ± 58.54
Total	36697.66 ± 779.03	34581.16 ± 567.59	118851.98 ± 2427.40
Data	36677.00	34573.00	118928.00
	HP Tagged TCR	LP Tagged TCR	Resolved Tagged TCR
Electron Multi-jet	-	-	-
Muon Multi-jet	-	-	-
Diboson	9.72 ± 1.13	8.75 ± 1.16	34.06 ± 4.98
Single-top	105.87 ± 20.65	119.66 ± 22.68	656.89 ± 132.96
$t\bar{t}$	1904.75 ± 50.61	1483.86 ± 47.05	17965.33 ± 188.87
$W+jets$	32.36 ± 4.28	85.74 ± 6.96	489.01 ± 37.13
$Z+jets$	1.27 ± 0.13	1.93 ± 0.20	19.14 ± 1.94
Total	2053.98 ± 54.84	1699.93 ± 52.70	19164.43 ± 234.01
Data	2047.00	1708.00	19143.00

Table 12.2: Expected and Measured for DY WZ $W+jets$, $t\bar{t}$ tag and untag control regions.

	HP Untagged SR	LP Untagged SR	Resolved Untagged SR
Electron Multi-jet	-	-	7782.17 ± 1175.56
Muon Multi-jet	-	-	17004.81 ± 1834.40
Diboson	3041.17 ± 273.77	2266.35 ± 212.79	14724.12 ± 1224.31
Single-top	2123.28 ± 373.83	1379.35 ± 240.92	18336.88 ± 3082.47
$t\bar{t}$	11678.86 ± 213.63	8906.34 ± 136.88	112669.24 ± 2122.46
$W+jets$	22741.32 ± 191.47	41726.76 ± 240.56	342934.00 ± 2280.21
$Z+jets$	442.03 ± 44.84	849.79 ± 86.42	9271.83 ± 939.52
Total	40026.65 ± 546.81	55128.59 ± 432.90	522723.03 ± 5131.71
Data	40193.00	54735.00	521813.00
	HP Tagged SR	LP Tagged SR	Resolved Tagged SR
Electron Multi-jet	-	-	199.22 ± 29.58
Muon Multi-jet	-	-	393.43 ± 124.06
Diboson	102.58 ± 11.59	65.44 ± 8.05	624.07 ± 58.10
Single-top	178.21 ± 33.62	155.53 ± 28.95	3470.39 ± 617.48
$t\bar{t}$	1017.93 ± 31.95	706.76 ± 26.20	38189.30 ± 401.91
$W+jets$	325.58 ± 41.62	575.36 ± 43.29	6161.96 ± 467.71
$Z+jets$	7.81 ± 0.80	11.62 ± 1.19	183.36 ± 18.55
Total	1632.11 ± 63.39	1514.70 ± 58.86	49221.74 ± 884.06
Data	1699.00	1559.00	48919.00

Table 12.3: Expected and Measured for DY WZ $W+jets$, $t\bar{t}$ tag and untag signal regions.

	HP WCR	LP WCR	Resolved WCR
Electron Multi-jet	-	-	898.48 ± 137.82
Muon Multi-jet	-	-	601.46 ± 182.74
Diboson	107.45 ± 45.20	166.87 ± 68.11	292.10 ± 235.29
Single-top	78.19 ± 18.22	132.71 ± 31.93	879.82 ± 216.89
$t\bar{t}$	400.71 ± 28.35	569.70 ± 48.88	5067.51 ± 155.69
$W+jets$	864.49 ± 63.44	1940.80 ± 89.41	18563.70 ± 408.99
$Z+jets$	19.51 ± 2.00	46.63 ± 4.77	795.20 ± 80.89
Total	1470.35 ± 84.89	2856.71 ± 126.74	27098.28 ± 594.01
Data	1495.00	2898.00	27120.00
	HP TCR	LP TCR	Resolved TCR
Electron Multi-jet	-	-	-
Muon Multi-jet	-	-	-
Diboson	14.95 ± 6.61	27.57 ± 14.12	24.33 ± 20.32
Single-top	68.31 ± 16.17	58.93 ± 13.56	278.60 ± 73.04
$t\bar{t}$	496.60 ± 31.72	401.23 ± 32.13	3834.49 ± 104.60
$W+jets$	50.68 ± 4.19	144.02 ± 7.86	450.01 ± 11.87
$Z+jets$	1.32 ± 0.14	5.35 ± 0.55	29.96 ± 3.07
Total	631.87 ± 36.45	637.10 ± 38.44	4617.39 ± 129.77
Data	636.00	634.00	4615.00
	HP SR	LP SR	Resolved SR
Electron Multi-jet	-	-	596.34 ± 91.52
Muon Multi-jet	-	-	481.01 ± 144.48
Diboson	148.84 ± 48.64	181.42 ± 67.30	395.52 ± 318.06
Single-top	79.49 ± 19.80	56.82 ± 14.89	782.07 ± 190.79
$t\bar{t}$	338.42 ± 24.14	236.80 ± 20.88	4261.70 ± 138.98
$W+jets$	501.13 ± 39.36	1347.76 ± 64.50	11445.73 ± 291.49
$Z+jets$	9.25 ± 0.95	28.77 ± 2.95	567.66 ± 57.94
Total	1077.13 ± 69.93	1851.57 ± 96.73	18530.03 ± 523.88
Data	1096.00	1846.00	18530.00

Table 12.4: Expected and Measured for VBF WW $W+jets$, $t\bar{t}$ control regions and signal regions.

	HP WCR	LP WCR	Resolved WCR
Electron Multi-jet	-	-	870.00 ± 132.75
Muon Multi-jet	-	-	618.45 ± 196.90
Diboson	92.92 ± 41.77	145.90 ± 64.26	228.62 ± 114.62
Single-top	71.13 ± 16.29	118.82 ± 27.98	1209.87 ± 281.64
$t\bar{t}$	427.80 ± 29.72	509.19 ± 46.57	6860.87 ± 254.83
$W+jets$	871.68 ± 64.22	2020.67 ± 93.54	19088.50 ± 442.10
$Z+jets$	19.58 ± 2.01	47.39 ± 4.85	800.19 ± 82.02
Total	1483.11 ± 83.79	2841.97 ± 125.92	29676.50 ± 644.96
Data	1495.00	2898.00	29755.00
	HP TCR	LP TCR	Resolved TCR
Electron Multi-jet	-	-	-
Muon Multi-jet	-	-	-
Diboson	10.12 ± 4.51	12.73 ± 6.55	14.23 ± 7.49
Single-top	51.57 ± 12.31	35.07 ± 8.17	169.21 ± 44.54
$t\bar{t}$	470.06 ± 28.97	298.99 ± 25.28	2414.75 ± 75.42
$W+jets$	49.64 ± 4.17	109.69 ± 6.16	378.22 ± 12.05
$Z+jets$	1.28 ± 0.13	4.81 ± 0.50	17.62 ± 1.83
Total	582.67 ± 32.07	461.30 ± 28.05	2994.03 ± 88.75
Data	584.00	459.00	3001.00
	HP SR	LP SR	Resolved SR
Electron Multi-jet	-	-	444.65 ± 67.99
Muon Multi-jet	-	-	397.29 ± 125.59
Diboson	109.66 ± 44.13	112.28 ± 46.45	265.75 ± 139.43
Single-top	63.16 ± 15.20	48.02 ± 11.56	872.16 ± 205.00
$t\bar{t}$	348.95 ± 24.34	190.68 ± 17.75	5134.25 ± 193.57
$W+jets$	467.21 ± 37.12	973.73 ± 47.91	10226.83 ± 254.67
$Z+jets$	8.15 ± 0.84	23.62 ± 2.43	558.48 ± 57.25
Total	997.13 ± 64.42	1348.33 ± 70.06	17899.41 ± 432.98
Data	1018.00	1313.00	17826.00

Table 12.5: Expected and Measured for VBF WZ $W+jets$, $t\bar{t}$ control regions and signal regions.

Background	Fitted Normalization
XS_Top_LP_lvqq_Merg_binned	$0.905^{+0.0166}_{-0.0166}$
XS_Top_Merg	$0.936^{+0.0199}_{-0.0199}$
XS_Top_Res	$0.957^{+0.0134}_{-0.0134}$
XS_Wjets_LP_lvqq_Merg_binned	$0.884^{+0.00489}_{-0.00489}$
XS_Wjets_Merg	$0.931^{+0.00831}_{-0.00831}$
XS_Wjets_Res	$1.03^{+0.00628}_{-0.00628}$

Table 12.6: Fitted background normalizations for $t\bar{t}$ and $W+jets$ backgrounds for the DY WW analysis region.

Background	Fitted Normalization
XS_Top_LP_Tag_lvqq_Merg_binned	$0.973^{+0.0333}_{-0.0333}$
XS_Top_LP_lvqq_Merg_binned	$0.894^{+0.0135}_{-0.0135}$
XS_Top_Merg	$0.893^{+0.016}_{-0.016}$
XS_Top_Res	$0.965^{+0.0179}_{-0.0179}$
XS_Top_Tag_lvqq_Merg_binned	$0.954^{+0.0276}_{-0.0276}$
XS_Top_Tag_lvqq_Res_binned	$0.999^{+0.0105}_{-0.0105}$
XS_Wjets_LP_Tag_lvqq_Merg_binned	$0.912^{+0.0703}_{-0.0703}$
XS_Wjets_LP_lvqq_Merg_binned	$0.876^{+0.00502}_{-0.00502}$
XS_Wjets_Merg	$0.948^{+0.00779}_{-0.00779}$
XS_Wjets_Res	$1.01^{+0.00673}_{-0.00673}$
XS_Wjets_Tag_lvqq_Merg_binned	$0.906^{+0.117}_{-0.117}$
XS_Wjets_Tag_lvqq_Res_binned	$1.2^{+0.0904}_{-0.0904}$

Table 12.7: Fitted background normalizations for $t\bar{t}$ and $W+jets$ backgrounds for the DY WZ analysis region.

Background	Fitted Normalization
XS_Top_LP_lvqq_Merg_binned	$0.79^{+0.0673}_{-0.0673}$
XS_Top_Merg	$0.888^{+0.061}_{-0.061}$
XS_Top_Res	$1.01^{+0.0311}_{-0.0311}$
XS_Wjets_LP_lvqq_Merg_binned	$0.88^{+0.0423}_{-0.0423}$
XS_Wjets_Merg	$0.881^{+0.0677}_{-0.0677}$
XS_Wjets_Res	$0.932^{+0.0202}_{-0.0202}$

Table 12.8: Fitted background normalizations for $t\bar{t}$ and $W+jets$ backgrounds for the VBF WW analysis region.

Background	Fitted Normalization
XS_Top_LP_lvqq_Merg_binned	$0.708^{+0.064}_{-0.064}$
XS_Top_Merg	$0.958^{+0.0644}_{-0.0644}$
XS_Top_Res	$1.02^{+0.038}_{-0.038}$
XS_Wjets_LP_lvqq_Merg_binned	$0.9^{+0.0438}_{-0.0438}$
XS_Wjets_Merg	$0.883^{+0.0685}_{-0.0685}$
XS_Wjets_Res	$0.945^{+0.0219}_{-0.0219}$

Table 12.9: Fitted background normalizations for $t\bar{t}$ and $W+jets$ backgrounds for the VBF WZ analysis region.

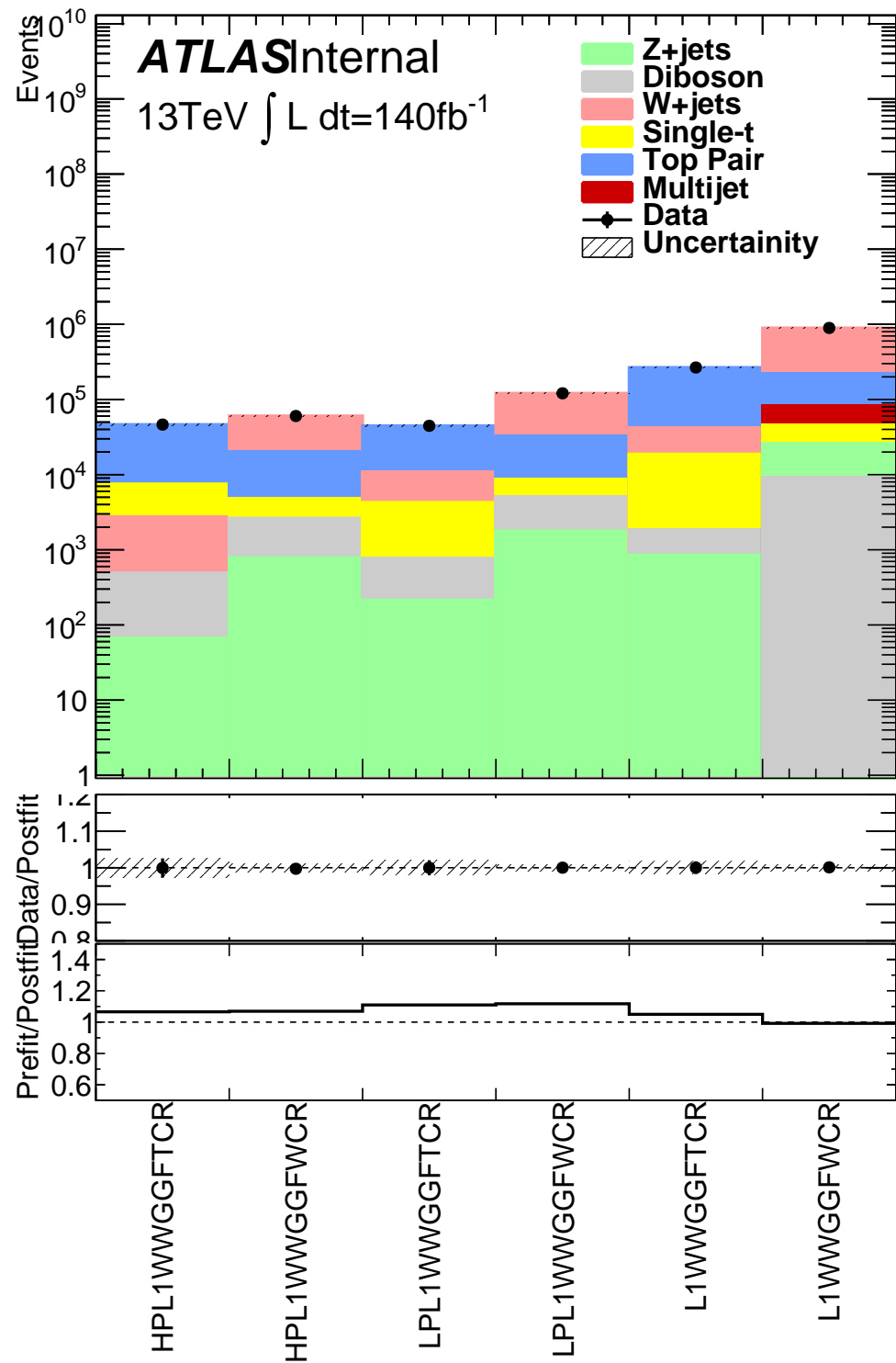


Figure 12.1: This figure shows the distribution of $m_{\ell\nu qq}$ in the DY WW control regions.

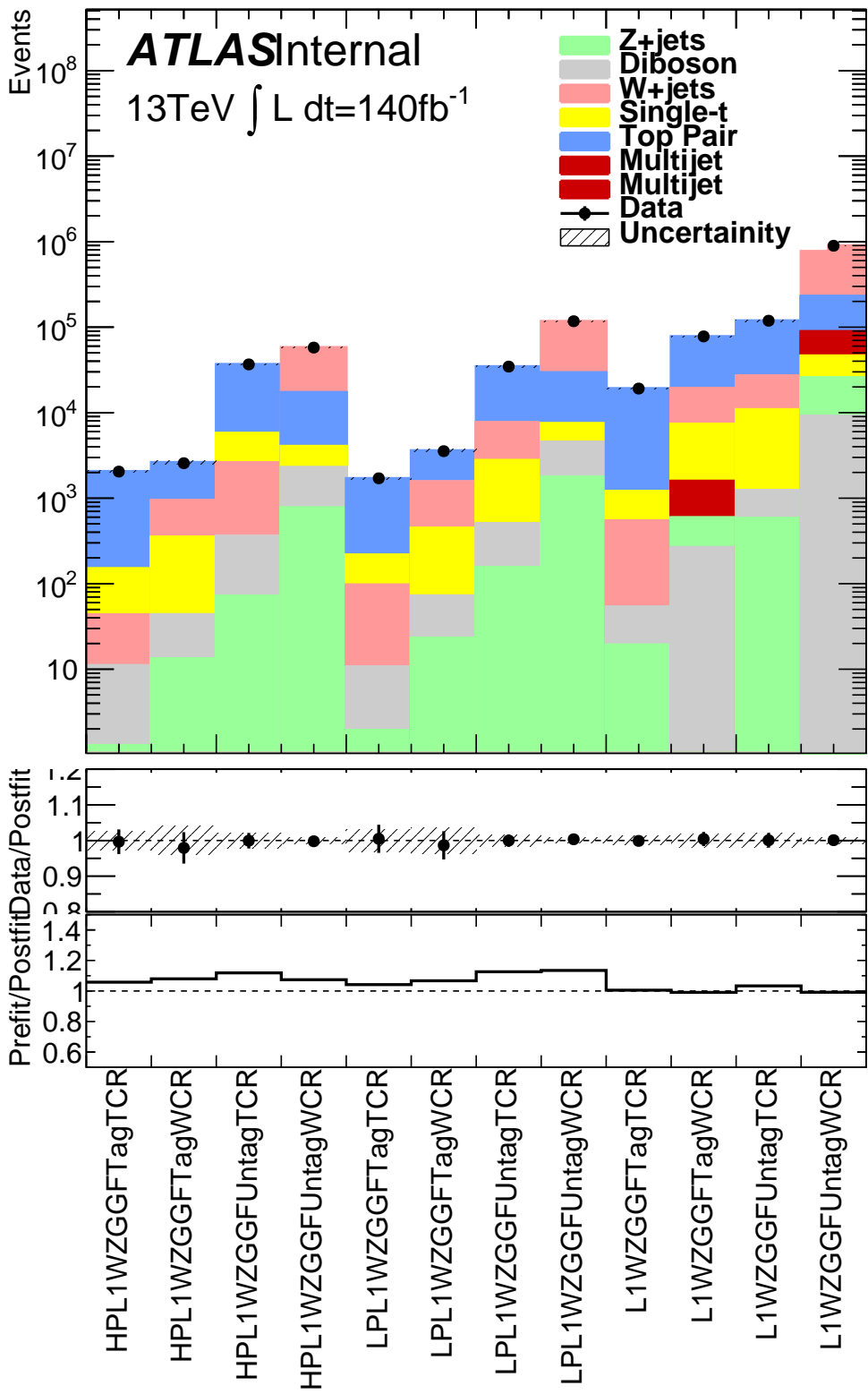


Figure 12.2: This figure shows the distribution of $m_{\ell\nu qq}$ in the DY WZ control regions.

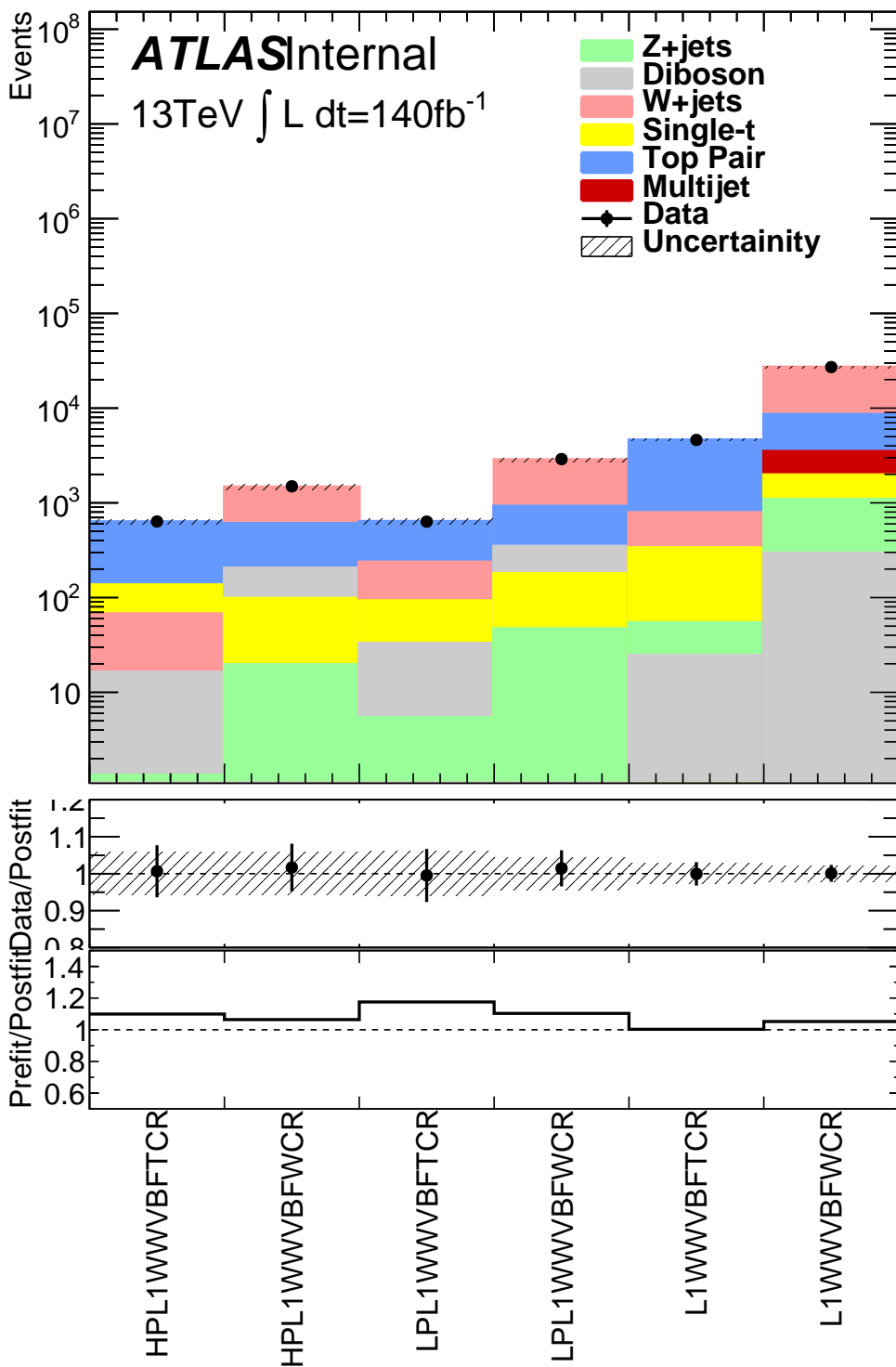


Figure 12.3: This figure shows the distribution of $m_{\ell\nu qq}$ in the VBF WW control regions.

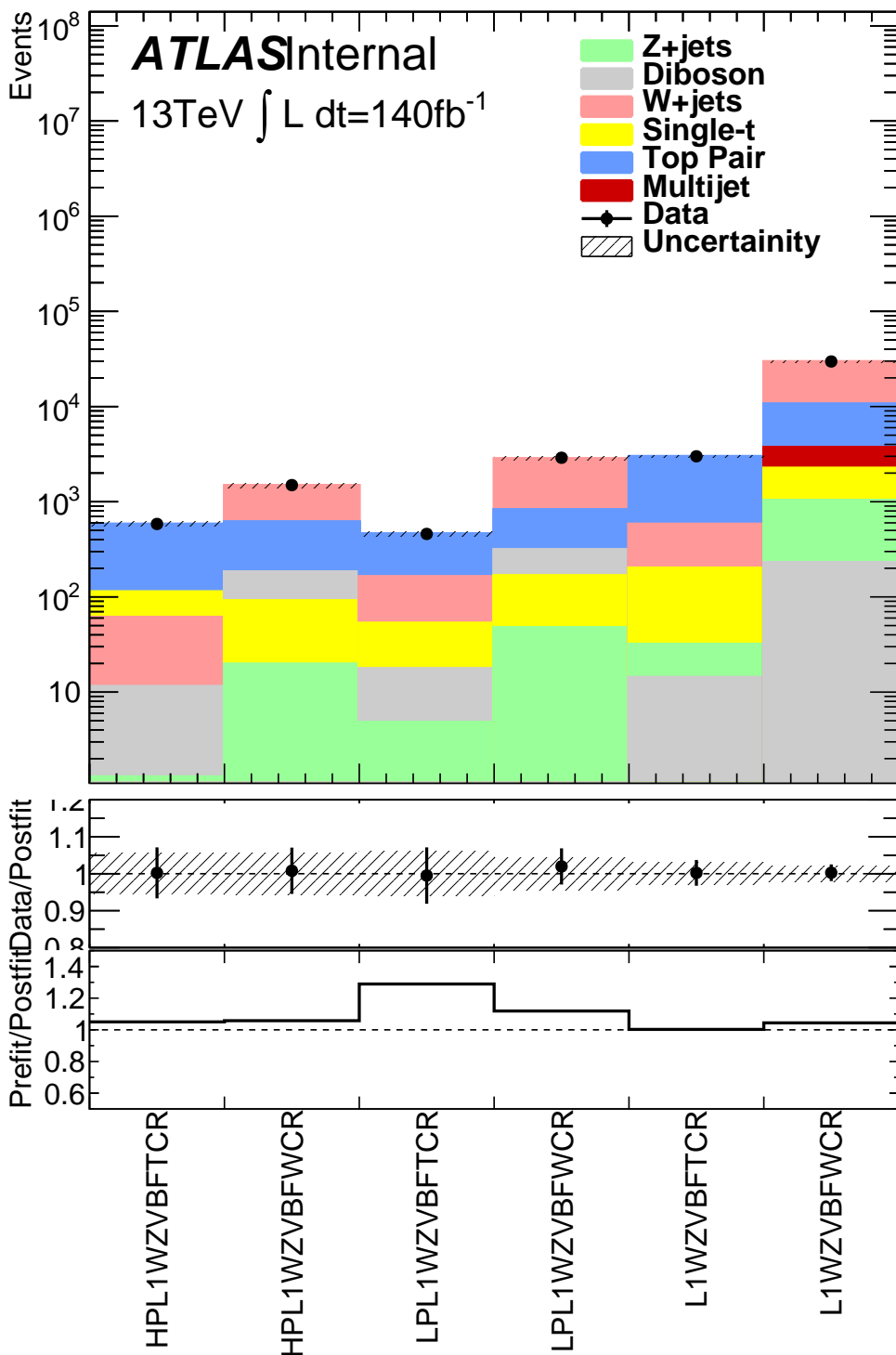


Figure 12.4: This figure shows the distribution of $m_{\ell\nu qq}$ in the VBF WZ control regions.

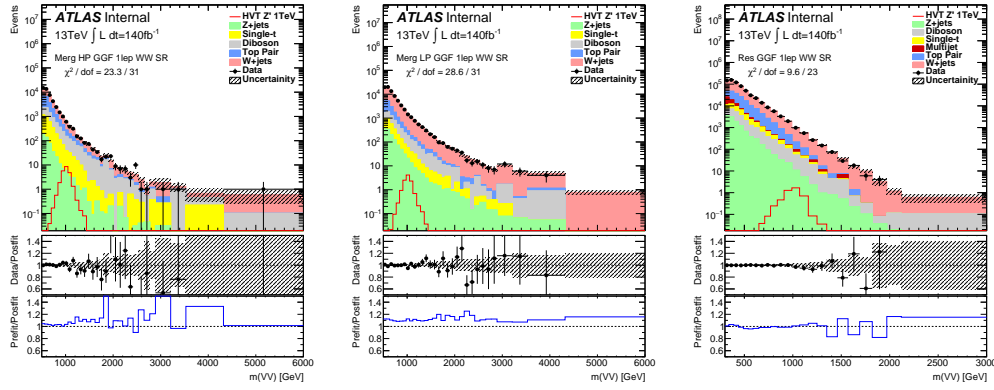


Figure 12.5: This figure shows the distribution of $m_{\ell\nu qq}$ in the GGF WW signal regions.

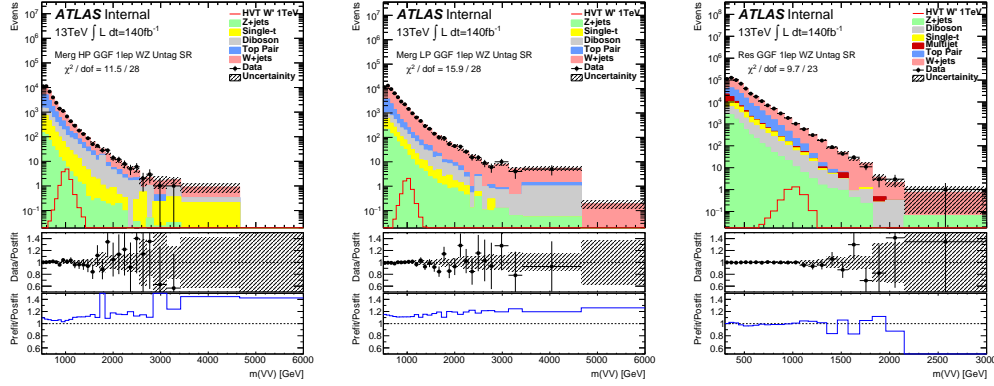


Figure 12.6: This figure shows the distribution of $m_{\ell\nu qq}$ in the GGF WZ Untag signal regions.

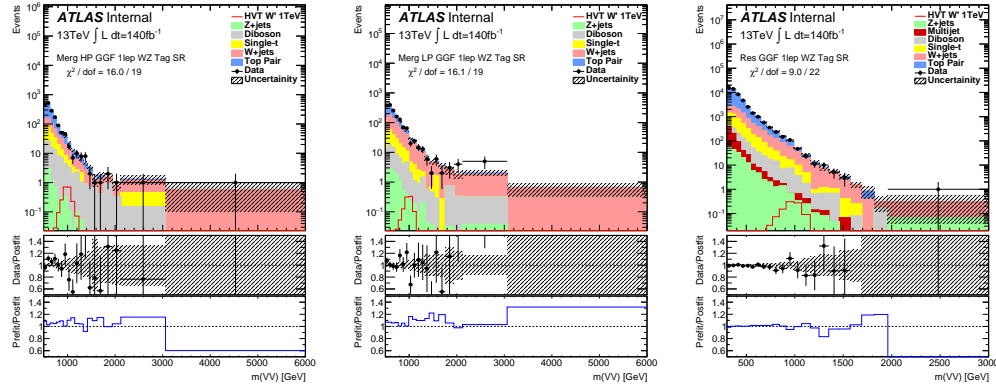


Figure 12.7: This figure shows the distribution of $m_{\ell\nu qq}$ in the GGF WZ Tag signal regions.

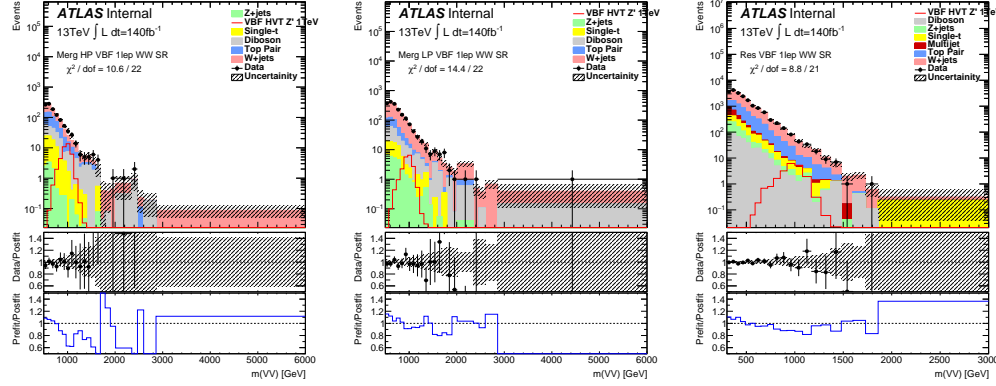


Figure 12.8: This figure shows the distribution of $m_{\ell\nu qq}$ in the VBF WZ Tag signal regions.

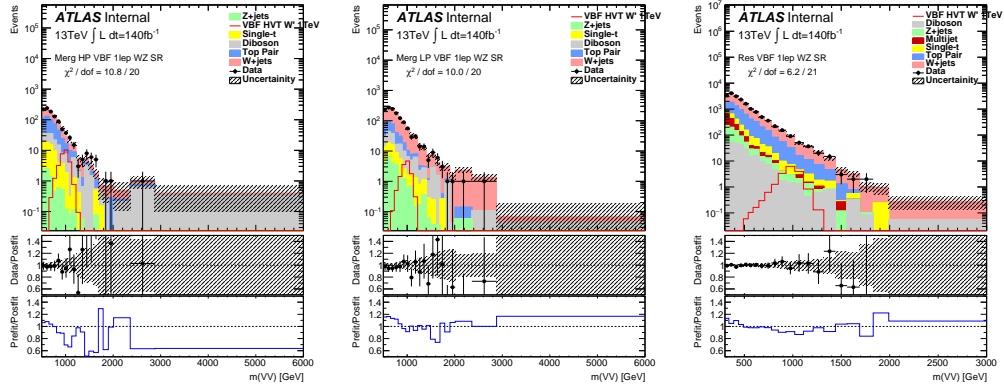


Figure 12.9: This figure shows the distribution of $m_{\ell\nu qq}$ in the VBF WZ Tag signal regions.

12.2 Systematic Profiling and Correlations

The ranked systematics and their fitted values are shown for the different analysis regions in Figure 12.10 - 12.12. Note that background normalizations for $W+jets$ and $t\bar{t}$ are left free to float in the fit. This means the nominal normalization values are at one and the uncertainties are not plotted in the ranked plots. Overall, systematics are not pulled outside their uncertainties, especially for highly ranked nuisance parameters.

The correlation between systematics are shown in Figures ???. Correlations between background normalization are expected. The remaining systematic correlations are not very strong or unexpected.

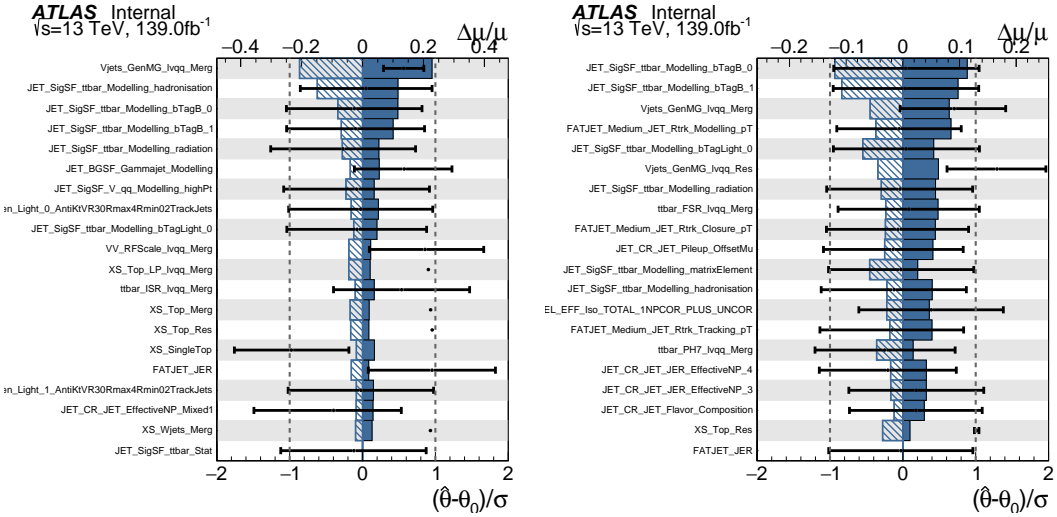


Figure 12.10: Ranked systematics and their fitted values for WW DY (right) and VBF (left) selections.

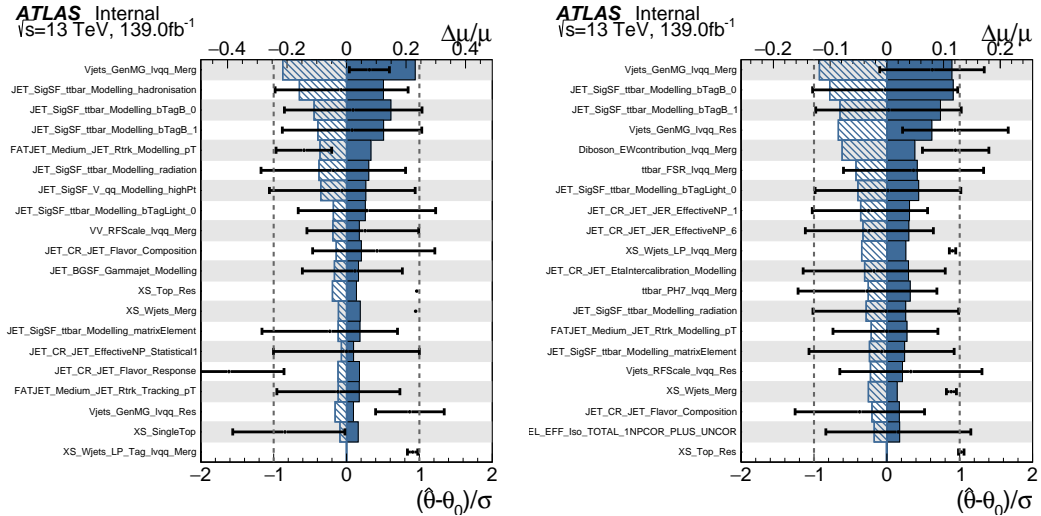


Figure 12.11: Ranked systematics and their fitted values for WZ DY (right) and VBF (left) selections.

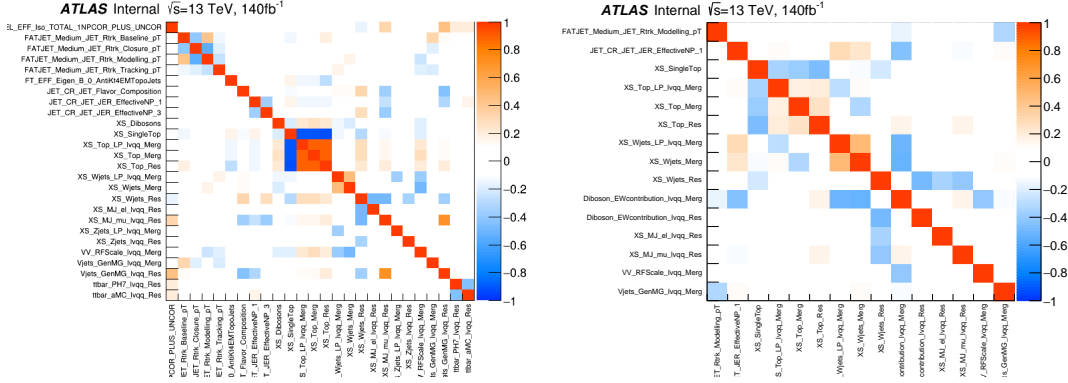


Figure 12.12: Correlations between systematics for WW DY (right) and VBF (left) selections.

12.3 Discovery Tests

To test for the existence of signal in the observed dataset, the discovery tests discussed earlier are used to calculate p-values as a function of resonance mass. The results of these tests are shown in Figures 12.13 - 12.17. Across the different DY signals the largest excesses are $\sim 2.2\sigma$ at 600 GeV and 1.8σ at 2 TeV. The largest excesses for VBF signals are $< 2.5\sigma$ at for 1 TeV resonances. As these deviations do not constitute discoveries, upper limits on μ are calculated.

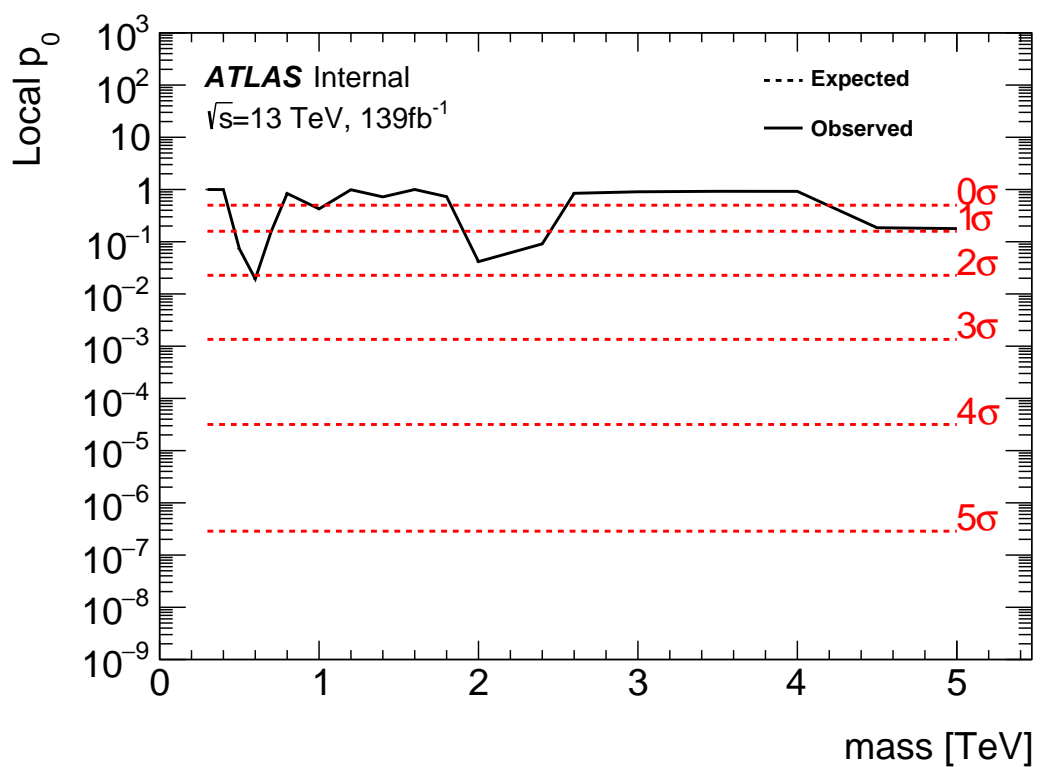


Figure 12.13: These plots show the measured p_0 value as a function of resonance mass for HVT Z' DY production.

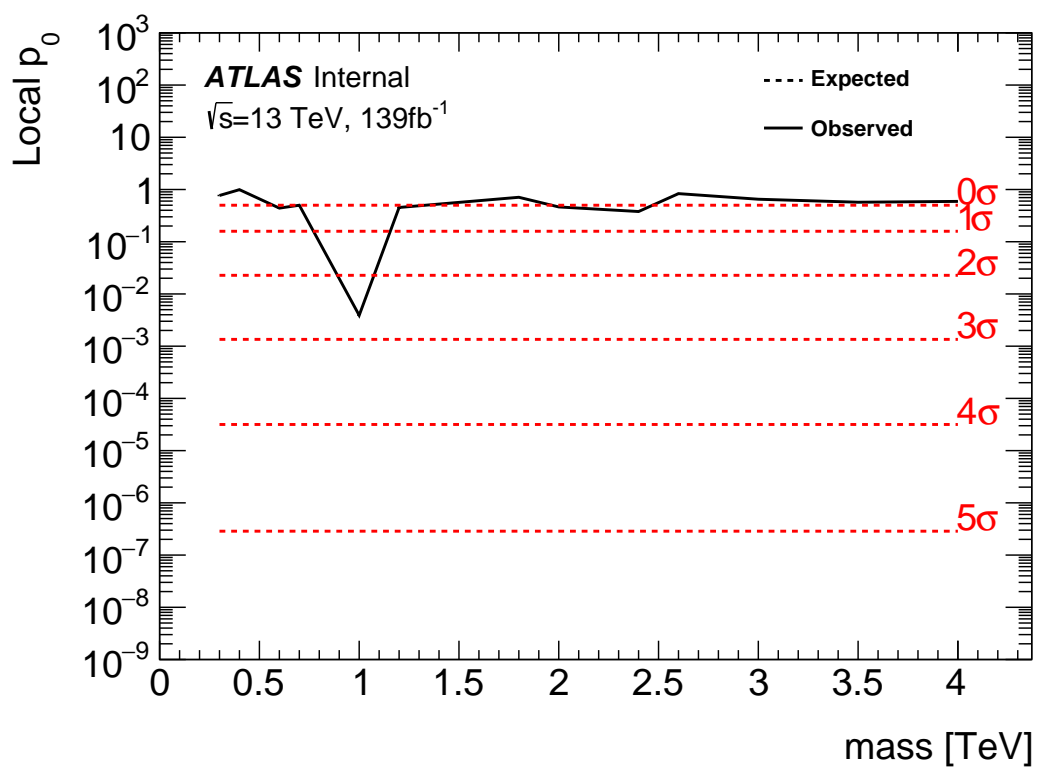


Figure 12.14: These plots show the measured p_0 value as a function of resonance mass for HVT Z' VBF production.

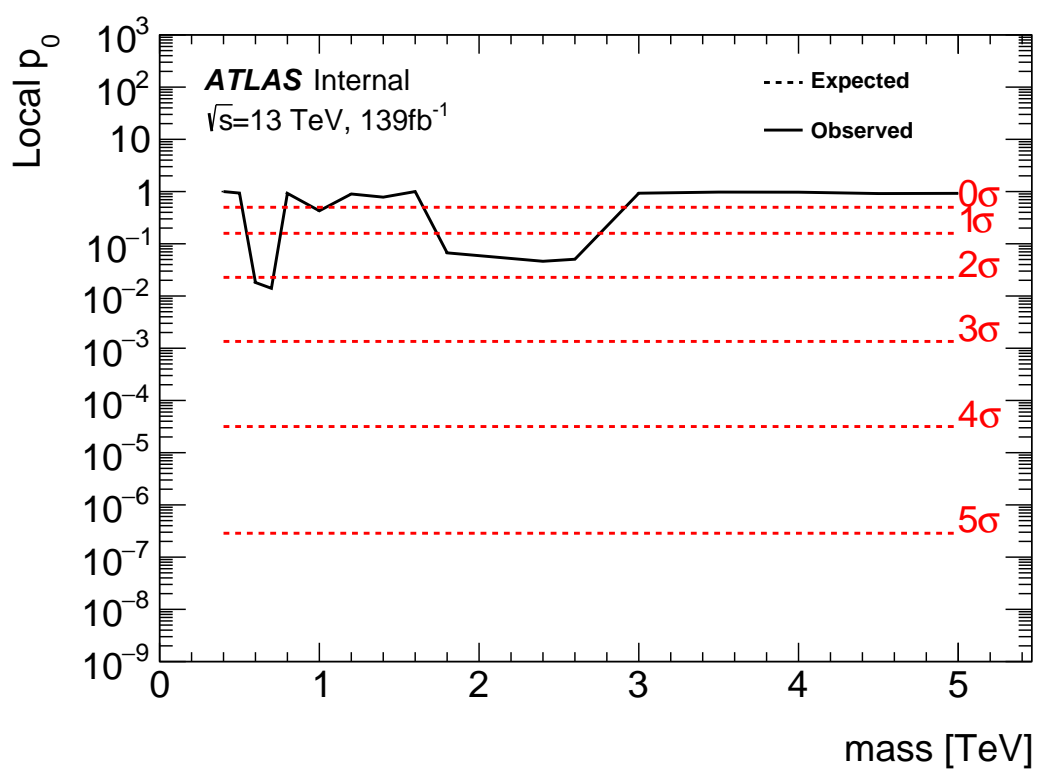


Figure 12.15: These plots show the measured p_0 value as a function of resonance mass for HVT W' DY production.

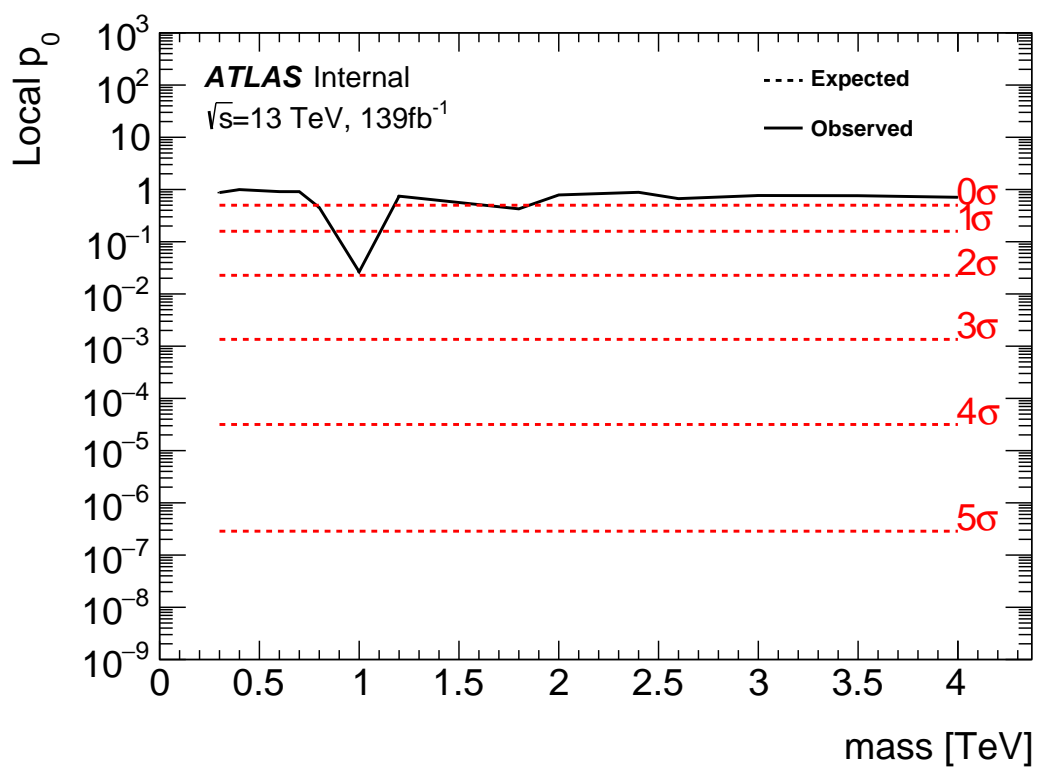


Figure 12.16: These plots show the measured p_0 value as a function of resonance mass for HVT W' VBF production.

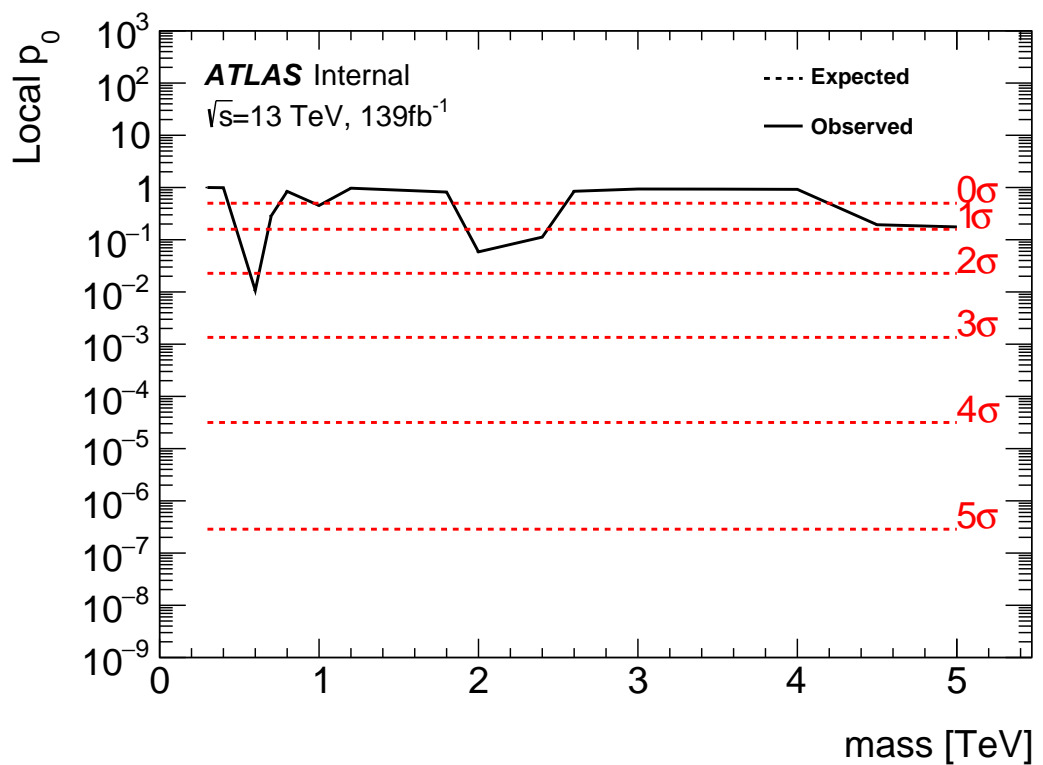


Figure 12.17: These plots show the measured p_0 value as a function of resonance mass for the RS Graviton DY production.

12.4 Limits

Using the exclusion limits tests discussed previously, exclusion limits are set on μ and consequently cross-sections for different signal models. Exclusion limits for the models considered are shown in Figure 12.18 - 12.20. These limits exclude HVT Model A $W' < 3.4\text{TeV}$ and $Z' < 3.3 \text{ TeV}$ and Model B $W' < 3.7 \text{ TeV}$ and $Z' < 3.7 \text{ TeV}$. Randall Sundrum Gravitons are excluded for masses below 1.6TeV .

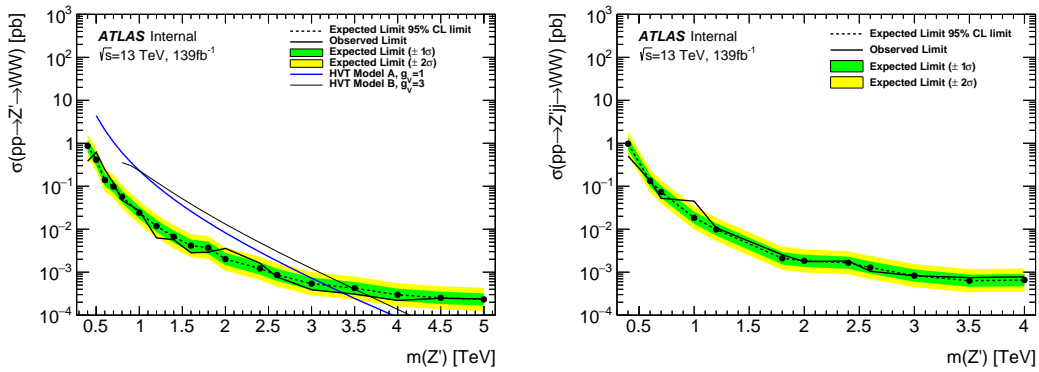


Figure 12.18: This figure shows theory, expected and observed limits for HVT W' DY (left) and VBF (right) production.

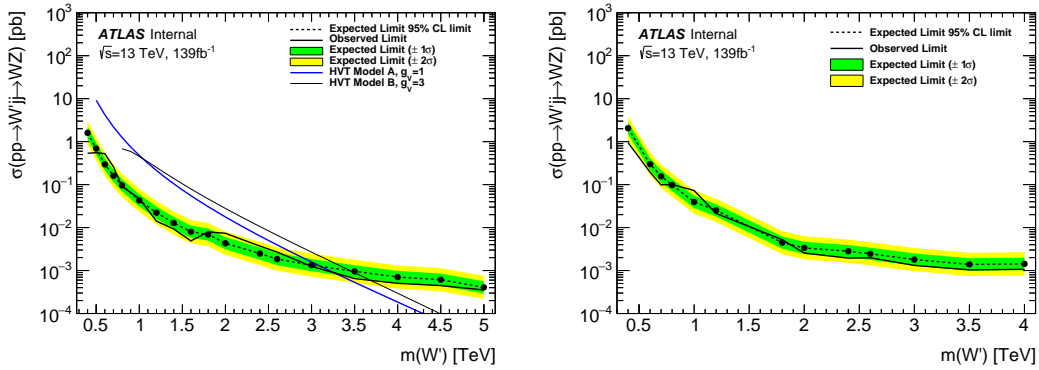


Figure 12.19: This figure shows theory, expected and observed limits for HVT Z' DY (left) and VBF (right) production.

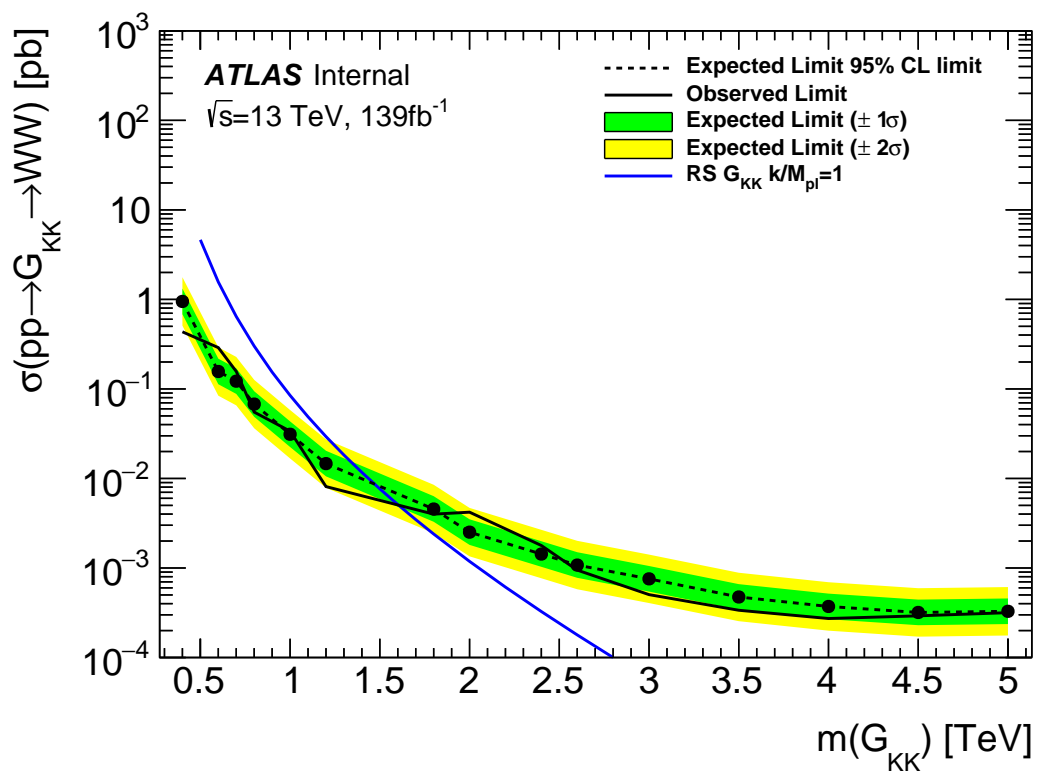


Figure 12.20: This figure shows theory, expected and observed limits for RS Gravitons via DY production.

Part V

1296

Quark and Gluon Tagging

1297

₁₂₉₈ **Chapter 13**

₁₂₉₉ **Prospects**

₁₃₀₀ For the resolved analysis, signal jets are quark enriched and background jets are
₁₃₀₁ gluon dominated. By classifying jets in the event as quark or gluon initiated, less
₁₃₀₂ background would contaminate the signal region. Figure 13.1 shows the PDGID
₁₃₀₃ for the truth parton matched to the jet (meaning the highest energy parton in
₁₃₀₄ the jet catchment area) in events passing the resolved signal region selections.
₁₃₀₅ PDGID = -1 corresponds to pileup jets, $0 < \text{PDGID} < 6$ correspond to quarks
₁₃₀₆ and $\text{PDGID} = 21$ corresponds to gluons. From this Figure, it is evident that a
₁₃₀₇ notable fraction of the background that contaminates the signal region contains
₁₃₀₈ gluon jets, especially for the sub-leading jet.

₁₃₀₉ As gluons jets have more constituents and therefore more tracks (n_{trk}), the
₁₃₁₀ background jets have more tracks than the signal jets. This is shown in Fig-
₁₃₁₁ ure 13.2. Therefore, by cutting on the number of tracks in a jet, quark and gluon
₁₃₁₂ jets may be distinguished (i.e. jets with less than a given number of tracks are
₁₃₁₃ classified as a quark, otherwise the jet is classified as a gluon.) Moreover, as the
₁₃₁₄ momentum of the jet increases the number of tracks also increases logarithmically
₁₃₁₅ [Cite nachman thesis Natasha]. Therefore by applying a cut on the number of
₁₃₁₆ tracks that scales with the $\ln(p_T)$ is more powerful than a threshold cut on the

1317 number of tracks. Figure 13.3-Figure 13.6 show normalized heat maps of $\ln(p_T)$
1318 vs the number of reconstructed tracks for the background and a 300 GeV Z' signal.
1319 In these plots it is evident that the number of tracks in the background jets grows
1320 more quickly with $\ln(p_T)$ than for the signal jets. This is expected given that the
1321 signal is quark dominated and the background is gluon dominated.

1322 In Figure 13.8 is the ROC Curve for quark gluon tagging with cut on the
1323 number of tracks in a jet that depends on $\ln(p_T)$. The sum of the backgrounds in
1324 the signal region were used for this curve. Here the quark tagging efficiency is the
1325 ratio of quarks tagged as quarks to the total number of quarks in the signal region.
1326 The gluon rejection is calculated as the reciprocal of the gluon tagging efficiency.
1327 Choosing a 90% efficient working point with a rejection of 1.4 corresponds to a
1328 slope of 4 and intercept of -5. Tagging both jets in this analysis would yield an
1329 efficiency of $90\%^{n_{jets}}$. Focusing on the background in Figure 13.9, this cut helps
1330 minimize gluon contamination in the signal region. Also, from these heat maps it
1331 is obvious that the number of tracks in gluon jets grows more quickly than those
1332 in quark jets.

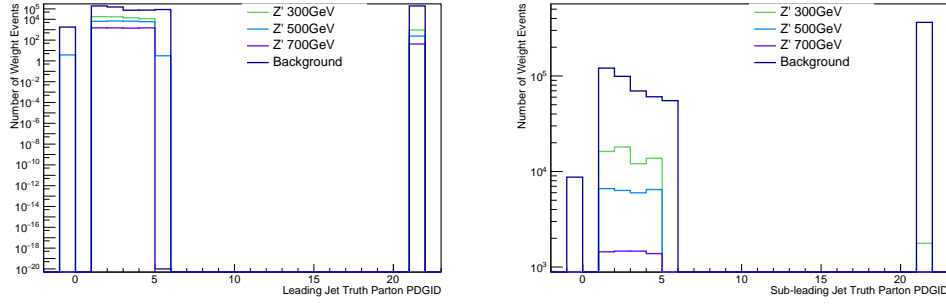


Figure 13.1: PDGID of the truth-level parton matched to the small-R jets passing the Resolved GGF WW Signal Region selections for the (a) Leading (b) Sub-Leading jets . These distributions are shown for 300, 500, and 700GeV Z' signals and the background.

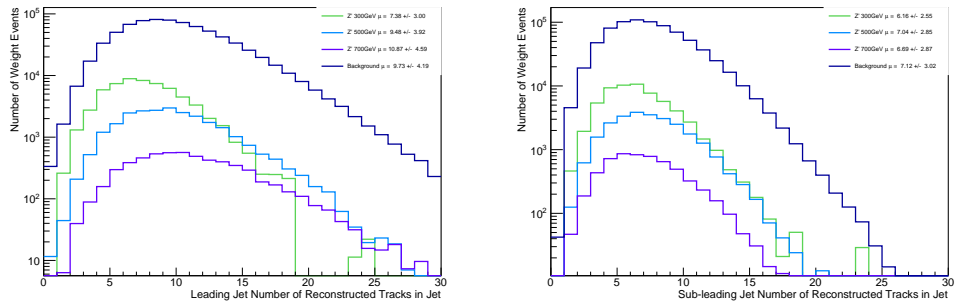


Figure 13.2: The number of tracks in small-R jets in events passing the Resolved GGF WW Signal Region selections for the (a) Leading (b) Sub-Leading jets. These distributions are shown for 300, 500, and 700GeV Z' signals and the background.

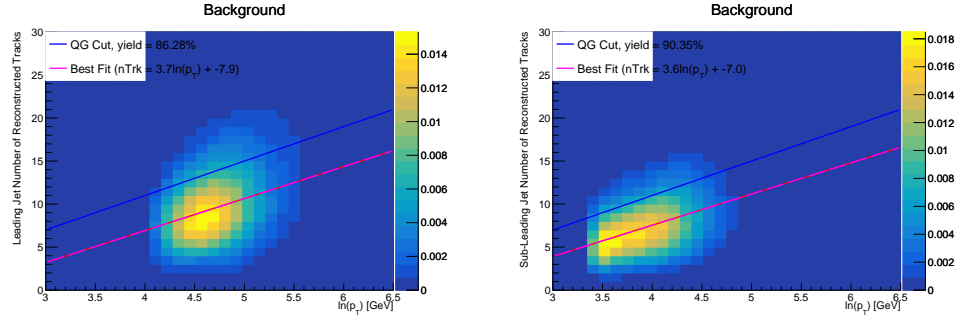


Figure 13.3: The number of tracks in background small-R jets in events passing the Resolved GGF WW Signal region selection vs. $\ln(p_T)$ for (a)Leading (b) Sub-Leading jets. The best fit line for the distribution is also shown, as well as the percentage of jets that pass a cut of number of tracks $< 4 \times \ln(p_T) - 5$. Note the number of total entries in these plots has been normalized to one.

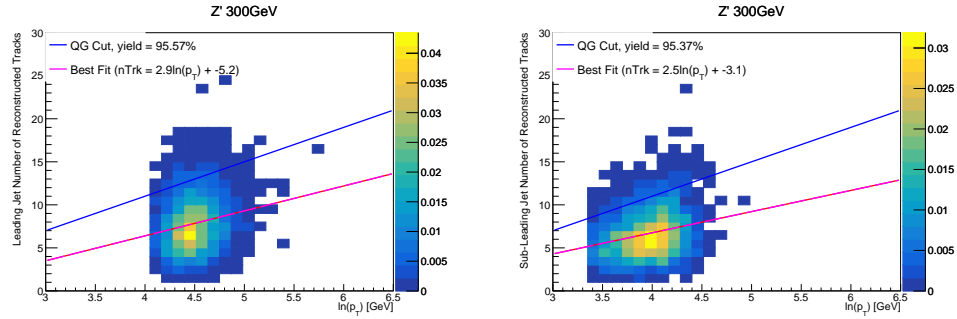


Figure 13.4: The number of tracks in small-R jets in 300GeV Z' events passing the Resolved GGF WW Signal region selection vs. $\ln(p_T)$ for (a)Leading (b) Sub-Leading jets. The best fit line for the distribution is also shown, as well as the percentage of jets that pass a cut of number of tracks $< 4 \times \ln(p_T) - 5$. Note the number of total entries in these plots has been normalized to one.

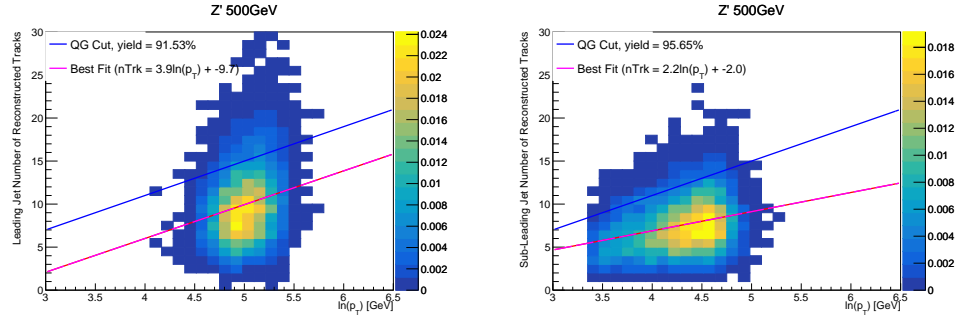


Figure 13.5: The number of tracks in small-R jets in 500GeV Z' events passing the Resolved GGF WW Signal region selection vs. $\ln(p_T)$ for (a)Leading (b) Sub-Leading jets. The best fit line for the distribution is also shown, as well as the percentage of jets that pass a cut of number of tracks $< 4 \times \ln(p_T) - 5$. Note the number of total entries in these plots has been normalized to one.

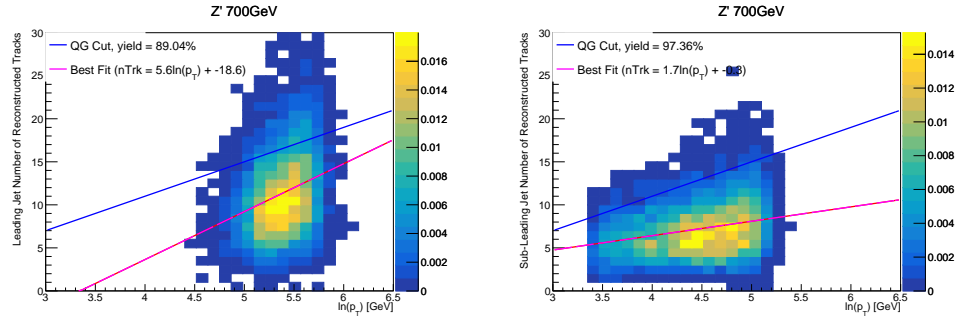


Figure 13.6: The number of tracks in small-R jets in 700GeV Z' events passing the Resolved GGF WW Signal region selection vs. $\ln(p_T)$ for (a)Leading (b) Sub-Leading jets. The best fit line for the distribution is also shown, as well as the percentage of jets that pass a cut of number of tracks $< 4 \times \ln(p_T) - 5$. Note the number of total entries in these plots has been normalized to one.

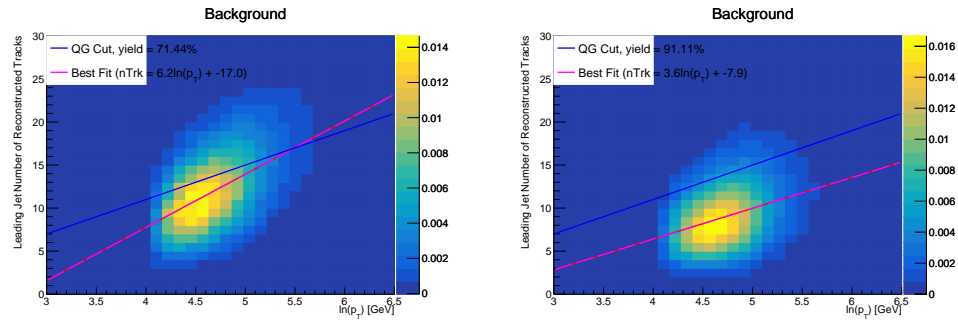


Figure 13.7: The number of tracks in leading small-R jets in background events passing the Resolved GGF WW Signal region selection vs. $\ln(p_T)$ for (a)Gluons (b) Quarks jets. The best fit line for the distribution is also shown, as well as the percentage of jets that pass a cut of number of tracks $< 4 \times \ln(p_T) - 5$.Note the number of total entries in these plots has been normalized to one.

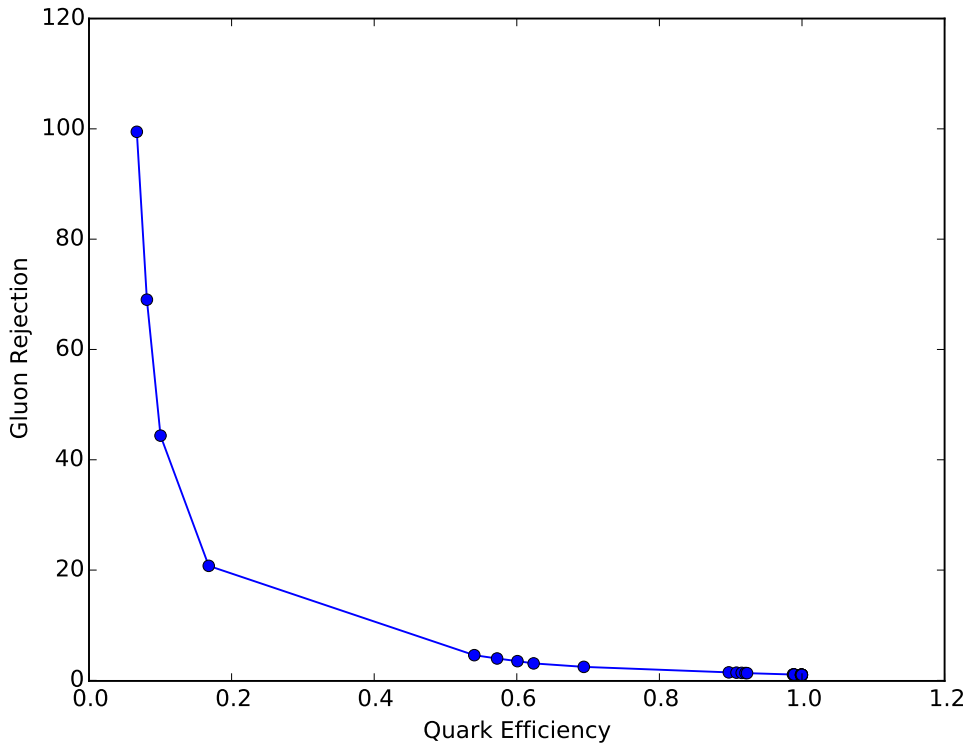


Figure 13.8: ROC Curve for Quark and Gluon Tagging with a cut on the number of tracks that depends on the $\ln(p_T)$.

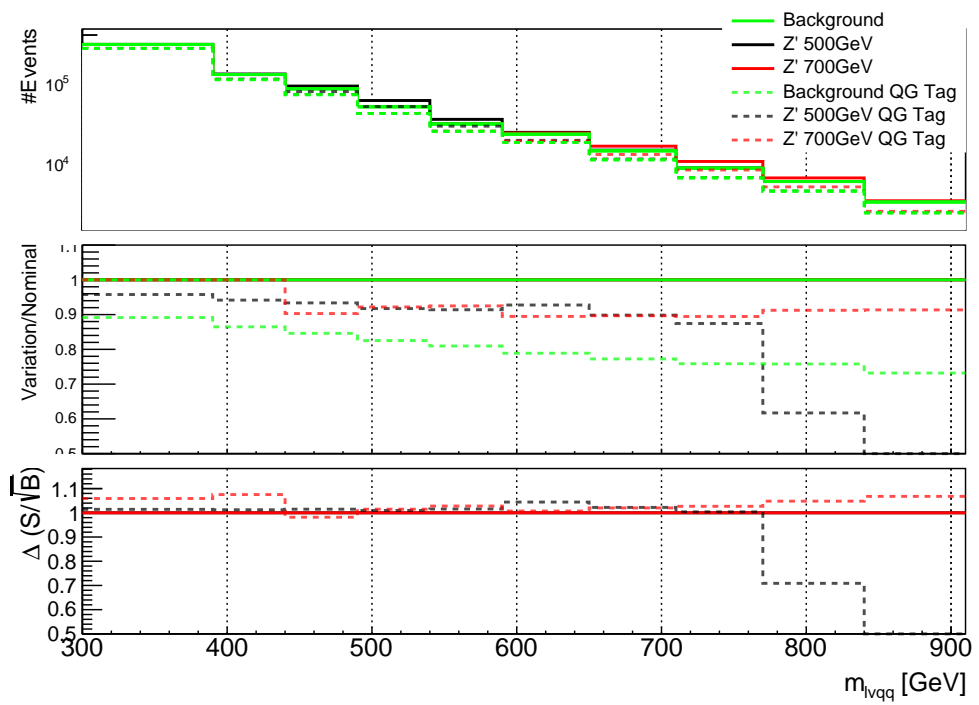


Figure 13.9: The top panel shows the distribution of m_{lvqq} with and without quark gluon tagging. The middle panel shows the ratio of the signals and backgrounds with and without quark gluon tagging. The bottom panel shows the change in S/\sqrt{B} with quark gluon tagging.

1333 Chapter 14

1334 n_{trk} Calibration

1335 As tagger based on nTrk cuts on the number of tracks in jets, a quantity that
1336 is not known with infinite precision, means that relevant systematic uncertainties
1337 must be evaluated. The sources of uncertainty in n_{trk} may be split into modeling
1338 and experimental uncertainties.

1339 Modeling uncertainties are obtained by assessing PDF and ME uncertainties
1340 on the number of charged particles in particle-level jets in dijet events. The
1341 number of charged particles as a function of jet p_T is calculated using an Iterative
1342 Bayesian (IB) technique [cite paper].

1343 This measurement ([9]) uses the ATLAS 2012 pp collision dataset, correspond-
1344 ing to $20.3/\text{fb}$ at center-of-mass energy $\sqrt{s} = 8\text{TeV}$. The number of charged con-
1345 stituents depends on fragmentation modeling and matrix elements, which do not
1346 depend on s . For this reason, it is safe to use these uncertainties for $\text{sqrt}(s)=13\text{TeV}$.
1347 Monte Carlo (MC) samples are used to determine the response matrix. The MC
1348 sample is a dijet sample generated with Pythia 8.175 using CT10 PDF and AU2
1349 tune. The anti- k_T algorithm is used to cluster jets with a radius parameter R
1350 $= 0.4$. Jets are required to have $|\eta| < 2.1$. Tracks in jets are required to have
1351 $p_T > 500\text{MeV}$, $|\eta| < 2.5$, track-fit $\chi^2 < 3.0$ and originate from the primary ver-

tex. Matching tracks to jets is accomplished using ghost-association [cite]. In this technique, jets are re-clustered with the track collection augmented with "ghost" versions of tracks. These "ghosts" tracks have the same direction as their parent track, but infinitesimal track p_T . This insures meta-jet properties (e.g. η , p_T , etc) are unchanged. A track is matched to a jet if it's ghost version remains in the jet after re-clustering. Further details of the data, object, and event selection may be found in [cite 35].

To select dijet topologies events are required to have at least two jets with $p_T > 50GeV$ that are relatively well-balanced ($p_T^{lead}/p_T^{sub-lead} < 1.5$).

In the IB technique, the prior distribution and number of iterations are the inputs [cite Bayesian paper]. The IB response matrix connects number of charged particles to the number of tracks in jets determined using the simulated samples. This response matrix is used to unfold data to extract the n_c . Before applying the response matrix a fake factor is applied. This accounts for jets that pass detector level selections, but not particle level selections. Following this, the IB method iteratively applies the response matrix using the nominal Pythia 8.175 sample as a prior. The number of IB iterations is chosen to minimize unfolding bias and statistical fluctuations. For this measurement four iterations was found to be optimal by minimizing the unfolding bias from pseudodata simulated with Herwig++ with a prior from Pythia 8 AU2. Finally, the inefficiency factor is applied to account for events passing particle level selection but not detector level, yielding the unfolded nCharged distribution.

This process is prone to three main sources of bias: response matrix, correction factor, and unfolding procedure uncertainties. The response matrix is sensitive to experimental uncertainties impacting jet track reconstruction and calorimeter jet p_T . Correction factors are also sensitive to experimental uncertainties (e.g. JES)

1378 as such uncertainties modify detector level acceptance. Sensitivity to particle
 1379 level acceptance is calculated by comparing Pythia and Herwig. Finally, the bias
 1380 from the IB prior choice is determined by reweighting the particle-level spectrum,
 1381 so the simulated detector level spectrum more closely matches the uncorrected
 1382 data. Unfolding this modified detector-level simulation and comparing it to the re-
 1383 weighted particle-level spectrum indicates bias from the prior distribution choice.

1384 A summary of all the systematic uncertainties associated with this unfolding
 1385 may be found in [ref paper]. Total uncertainties are < 7% for the number of
 1386 charged particles in jets. The unfolded distribution of the nCharged in jets from
 1387 data are further analyzed to extract the quark and gluon nCharged distributions.
 1388 In dijet events, the jet with a larger η is more energetic and therefore more likely
 1389 to be a quark. This is due to the quarks in protons generally having a larger
 1390 fraction of the total momentum of the proton constituents. The more central jet
 1391 is more likely to be a gluon-initiated jet. This correlation between jet η and flavor
 1392 may then be used to extract nCharged in p_T bins using:

$$\langle n_c^f \rangle = f_q^f \langle n_c^q \rangle + f_g^f \langle n_c^g \rangle \quad (14.1)$$

1393

$$\langle n_c^c \rangle = f_q^c \langle n_c^q \rangle + f_g^c \langle n_c^g \rangle \quad (14.2)$$

1394 In this equation the f and c subscripts denote the more forward and central
 1395 jets, respectively. The q and g subscripts denote quark and gluon. The fraction
 1396 of more forward jets that are say gluons is denoted by f_g^f . The other relevant jet
 1397 fractions are denoted with the same naming scheme. Finally, $\langle n_c \rangle$ is the average
 1398 number of charged particles in a jet in a given p_T bin. To show that Eq. (??) may
 1399 be used to extract quark and gluon n_c distributions the extracted distributions
 1400 are compared to n_c distributions determined using the jet flavor in simulation.
 1401 Figure [add figure natasha] shows that the extracted and true distributions differ

1402 by < 1% over the p_T range probed for this study. Moreover, this implies that n_c
1403 depends only on the flavor of the initiating parton and jet p_T .

1404 These extracted distributions are prone to PDF and ME biases. The bias from
1405 the choice of the CT10 PDF for the Pythia sample is accounted for by comparing
1406 quark/gluon fractions for the nominal CT10 sample with its eigenvector variations.
1407 Comparing the quark/gluon fractions from Pythia 8 and Herwig++ quantify the
1408 uncertainty from the ME calculation. These uncertainties are added in quadra-
1409 ture with the unfolding uncertainty to give the total modelling uncertainty on
1410 the extracted n_c distribution. This is shown in Figure 15.2.

1411 To apply these uncertainties in n_c distributions in data, per-jet event weights
1412 are associated with each uncertainty according to:

$$w_i(n_c) = \frac{P(n_c | n_c > \pm \sigma_{n_c}^i)}{P(n_c | n_c >)} \quad (14.3)$$

1413 In Eq. (??), i denotes the uncertainty considered, P is the Poisson probability,
1414 and $\sigma_{n_c}^i$ represents the average impact of the uncertainty on n_c .

1415 The previous uncertainties described accounted for modeling uncertainty as-
1416 sociated with the number of charged particles in a jet. However, n_c is not a
1417 measurable quantity. Instead the number of tracks in a jet is measured, which is
1418 a proxy for n_c . Therefore the uncertainties associated with the measurement of
1419 nTracks must also be considered ([11]). These uncertainties were calculated using
1420 a Pythia 8 dijet sample with NNPDF 23 and Run 2 data. Track reconstruction
1421 efficiency and fake rates are the dominant sources of nTrack uncertainties.

1422 The track reconstruction efficiency is affected by the uncertainty of the de-
1423 scription of the ID material in simulation and the modeling of charged-particle
1424 interactions with this material. These uncertainties are accounted for by varying
1425 the ID material by 5-25% (dependent on the region of the detector considered).

1426 The difference in the tracking efficiency between the nominal and varied simula-
1427 tion give the uncertainty on the track reconstruction efficiency. Another important
1428 source of track reconstruction inefficiency arises in the core of jets. The high den-
1429 sity of tracks in the jet cores can cause ID clusters to merge. The fraction of lost
1430 tracks due to merging is given by the fraction of tracks that have a charge of two
1431 minimum ionizing particles. This quantity is compared between data and simu-
1432 lation resulting in an uncertainty of 0.4% on tracks with $\Delta R < 0.1$. Combining
1433 these effects gives a total uncertainty as a function of p_T and η that is generally
1434 $< 2\%$ [references figure 44 from [11]].

1435 Fake tracks are the other dominant source of nTrk uncertainty. Fake tracks
1436 are tracks that cannot be associated to a single particle. Often these tracks are a
1437 result of random combinations of hits from charged particles that overlap in space.
1438 In dense environments, such as the core of jets or high-pileup environments, fake
1439 tracks are more likely. Fake tracks are estimated with a 'control region method'
1440 which is briefly summarized here [[10]]. By applying a series of track selections
1441 to enrich the fraction of fake tracks (e.g. $|d_0| > 0.1$, track $\chi^2 > 1.4$, etc) in
1442 simulation, templates for fake track parameters are calculated. These templates
1443 are then fit to data to determine the fraction of fake tracks. On average the fake
1444 rate is found to be 30% (independent of p_T and η).

1445 To assess the impact of these two detector level uncertainties, tracks are ran-
1446 domly dropped according to the rates described above. Reconstruction and fake
1447 uncertainties both lower the number of tracks, hence these uncertainties are one-
1448 sided. By dropping tracks in this way a varied nTrk distribution is calculated for
1449 both uncertainties. The associated per-jet event weights are then calculated in
1450 the same way as the modeling weights as:

$$w_i(n_c) = \frac{P(n_{trk} | < n_{trk} > \pm \sigma_{n_{trk}}^i)}{P(n_{trk} | < n_{trk} >)} \quad (14.4)$$

1451 Adding the modeling and detector level uncertainties in quadrature gives the
 1452 overall nTrack uncertainty. The effects of the individual uncertainties on the nTrk
 1453 distributions can be seen in Fig 15.4. Fig 15.3 shows the m_{lvqq} and nTrk distri-
 1454 butions for the W and Top control regions before likelihood fitting. In these plots
 1455 the nTrk uncertainties improve agreement between data and MC. The remaining
 1456 differences are likely covered by likelihood fitting and improving the analysis itself.

1457 **Chapter 15**

1458 **Application**

1459 Using the 90% WP of the n_{trk} tagger improves S/\sqrt{B} is $\sim 3\%$ as shown in
1460 Figure 13.9. Although, n_{trk} is the single most powerful discriminating variable
1461 for quark and gluon jets, the addition of other jet variables would improve the
1462 classification efficiency. Figure 15.1 shows the possible improvement of 10%
1463 in jet classification using the truth label of the jets to classify jets. This type of
1464 improvement is possible by using variables such as jet width, and energy correlata-
1465 tors. Figure [add BDT figure/use 1612.01551.pdf] shows for a 90% quark tagging
1466 efficiency for a 100 GeV jet, a BDT improve the gluon rejection by 0.4. Once this
1467 tagger is calibrated it would improve the analysis sensitivity of this channel.

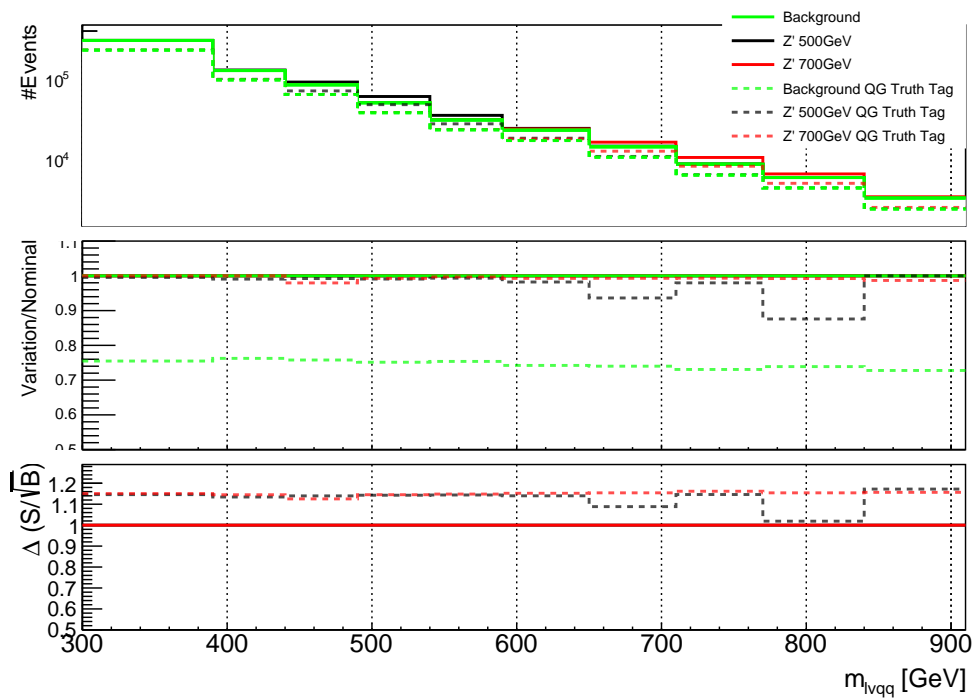


Figure 15.1: The top panel shows the distribution of m_{lvqq} with and without requiring jets to be true quarks. The middle panel shows the ratio of the signals and backgrounds with and without requiring jets to be true quarks. The bottom panel shows the change in S/\sqrt{B} when requiring jets to be true quarks..

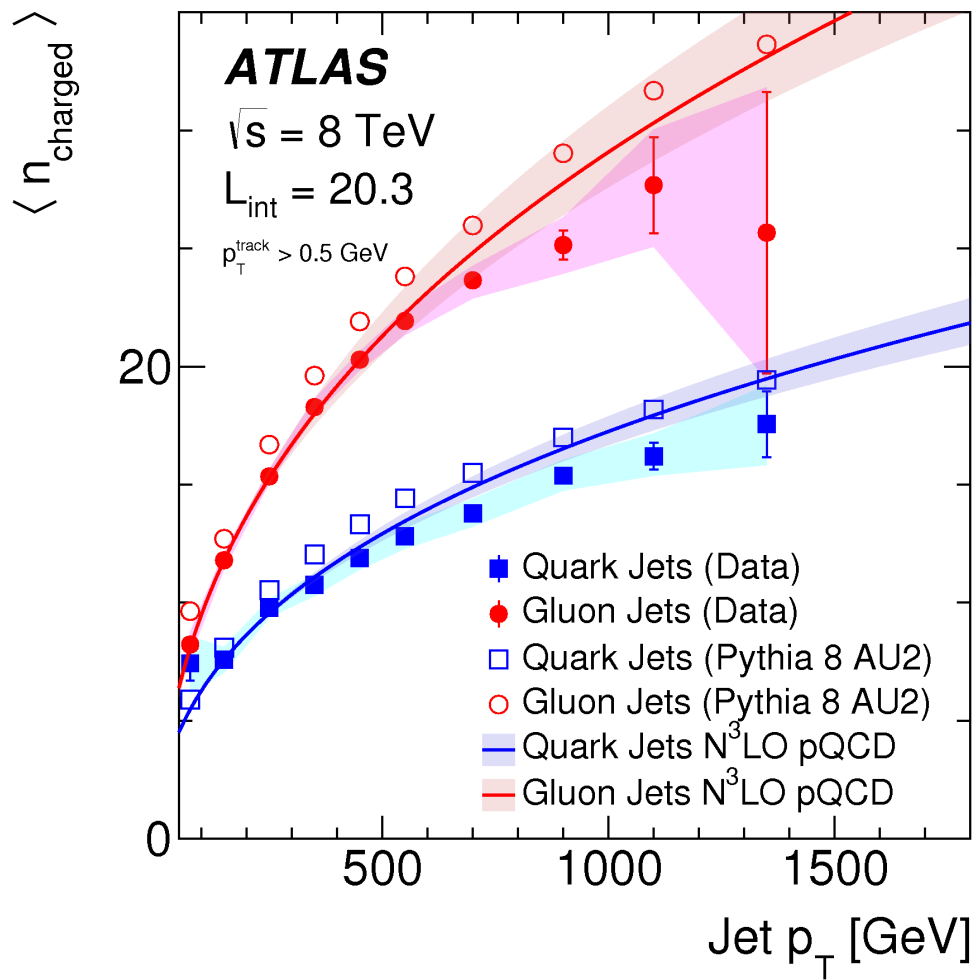


Figure 15.2: Unfolded and extracted n_C qg dstbs..

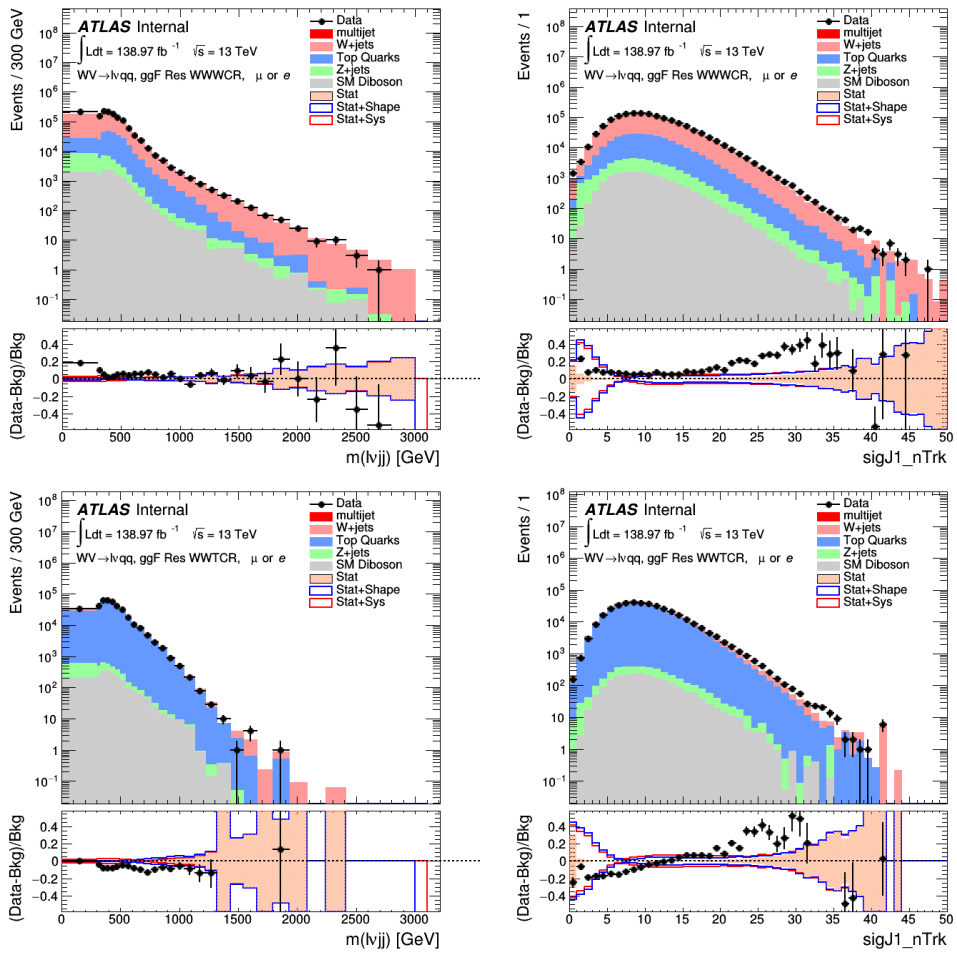


Figure 15.3: PDGID of the truth-level parton matched to the small-R jets passing the Resolved GGF WW Signal Region selections for the (a) Leading (b) Sub-Leading jets . These distributions are shown for 300, 500, and 700GeV Z' signals and the background.

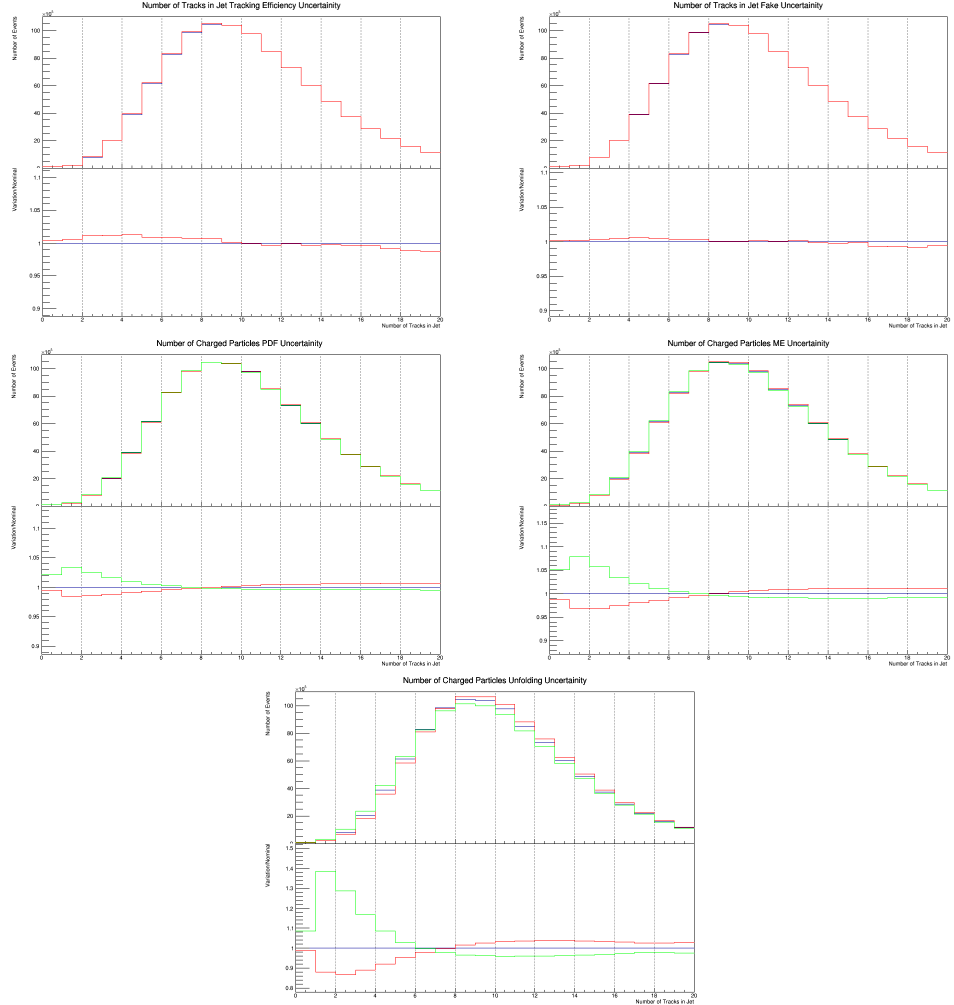


Figure 15.4: These figures show the impact of the uncertainties on the number of tracks in the leading jet in the sum of the background sample in the Resolved GGF WW SR (a) tracking efficiency (b) fake (c) PDF (d) ME (e) unfolding uncertainties.

Part VI

1468

Conclusion

1469

1470 **Chapter 16**

1471 **Conclusions**

1472 A search for WW and WZ diboson resonance production in $\ell\nu qq$ final states
1473 was performed using 139fb^{-1} of pp collision data collected at a center-of-mass
1474 energy of $\sqrt{s} = 13\text{TeV}$ by that ATLAS detector at the LHC between 2015 and
1475 2018. No excess of events above the background-only expectation was observed.
1476 The largest local excess is approximately 2.7σ , which is not significant. Limits
1477 on the production cross section are obtained for the HVT W' and Z' and RS
1478 Gravitons. Signal masses below 3.4 (3.7) TeV are excluded for HVT W' Model
1479 A(B). Signal masses below 3.3 (3.7) TeV are excluded for HVT Z' Model A(B).
1480 Randall Sundrum Gravitons are excluded for masses below 1.6 TeV. Going forward,
1481 improving the classification of jets in events would improve analysis sensitivity.
1482 To distinguish quark from gluon jets a jet tagger based on the number of tracks in
1483 jets is studied in the context of this search. Finally, the calibration of the number
1484 of tracks in jets is discussed.

Bibliography

- [1] Lecture notes particle physics ii.
- [2] Kaustubh Agashe, Hooman Davoudiasl, Gilad Perez, and Amarjit Soni. Warped Gravitons at the LHC and Beyond. *Phys. Rev.*, D76:036006, 2007.
- [3] G. Altarelli and G. Parisi. Asymptotic freedom in parton language. *Nuclear Physics B*, 126(2):298 – 318, 1977.
- [4] M. N. Chernodub. Background magnetic field stabilizes qcd string against breaking, 2010.
- [5] ATLAS Collaboration. Atlas muon reconstruction performance in lhc run 2.
- [6] ATLAS Collaboration. Summary plots from the atlas standard model physics group.
- [7] ATLAS Collaboration. Tagging and suppression of pileup jets with the atlas detector.
- [8] ATLAS Collaboration. Jet energy scale measurements and their systematic uncertainties in proton–proton collisions at $\sqrt{s} = 13$ tev with the atlas detector. arXiv: 1703.09665 [hep-ex].
- [9] ATLAS Collaboration. Measurement of the charged-particle multiplicity inside jets from $s=\sqrt{8}$ tev pp collisions with the atlas detector. arXiv:1602.00988 [hep-ex].
- [10] ATLAS Collaboration. Performance of the atlas track reconstruction algorithms in dense environments in lhc run 2. arXiv:1704.07983 [hep-ex].
- [11] ATLAS Collaboration. Properties of jet fragmentation using charged particles measured with the atlas detector in pp collisions at $\sqrt{s} = 13$ tev. arXiv:1906.09254 [hep-ex].
- [12] Alex Dias and V. Pleitez. Grand unification and proton stability near the peccei-quinn scale. *Physical Review D*, 70, 07 2004.

- 1511 [13] Stefan Höche, Frank Krauss, Marek Schönherr, and Frank Siegert. Qcd ma-
1512 trix elements + parton showers. the nlo case. *Journal of High Energy Physics*,
1513 2013(4), Apr 2013.
- 1514 [14] Diederik P. Kingma and Jimmy Ba. Adam: A method for stochastic opti-
1515 mization, 2014.
- 1516 [15] David Krohn, Jesse Thaler, and Lian-Tao Wang. Jets with variable r. *Journal*
1517 *of High Energy Physics*, 2009(06):059–059, Jun 2009.
- 1518 [16] Gregory Soyez Matteo Cacciari, Gavin P. Salam. The anti- k_T jet clustering
1519 algorithm. arXiv:0802.1189 [hep-ph].
- 1520 [17] Duccio Pappadopulo, Andrea Thamm, Riccardo Torre, and Andrea Wulzer.
1521 Heavy vector triplets: bridging theory and data. *Journal of High Energy*
1522 *Physics*, 2014(9), Sep 2014.
- 1523 [18] Antonio Pich. The Standard Model of Electroweak Interactions. In *Proceed-
1524 ings, High-energy Physics. Proceedings, 18th European School (ESHEP 2010):
1525 Raseborg, Finland, June 20 - July 3, 2010*, pages 1–50, 2012. [,1(2012)].
- 1526 [19] Lisa Randall and Raman Sundrum. A Large mass hierarchy from a small
1527 extra dimension. *Phys. Rev. Lett.*, 83:3370–3373, 1999.
- 1528 [20] Sebastian Raschka. Model evaluation, model selection, and algorithm selec-
1529 tion in machine learning, 2018.
- 1530 [21] Tania Robens and Tim Stefaniak. Lhc benchmark scenarios for the real higgs
1531 singlet extension of the standard model. *The European Physical Journal C*,
1532 76(5), May 2016.
- 1533 [22] Alex Sherstinsky. Fundamentals of recurrent neural network (RNN) and long
1534 short-term memory (LSTM) network. *CoRR*, abs/1808.03314, 2018.
- 1535 [23] Muhammed Ali Sit and Ibrahim Demir. Decentralized flood forecasting using
1536 deep neural networks. Jun 2019.
- 1537 [24] Wojciech Zaremba, Ilya Sutskever, and Oriol Vinyals. Recurrent neural net-
1538 work regularization, 2014.